UNIVERSITY OF CAPE TOWN

DOCTORAL THESIS

Observing flow using fast neutron radiography and positron emission particle tracking

Author:
Graham Clinton DANIELS

Supervisor:
Professor Andy BUFFLER

A thesis submitted in fulfillment of the requirements for the degree of Doctor of Philosophy

in

Department of Physics

February 12, 2021

Declaration of Authorship

I, Graham Clinton DANIELS, declare that this thesis entitled, "Observing flow using fast neutron radiography and positron emission particle tracking"and the work presented in it, are my own. I confirm that:

- This work was done wholly or mainly while in candidature for a research degree at the University of Cape Town.
- Where any part of this thesis has previously been submitted for a degree or any other qualification at this University or any other institution, this has been clearly stated.
- Where I have consulted the published work of others, this is always clearly attributed.
- Where I have quoted from the work of others, the source is always given. With the exception of such quotations, this thesis is entirely my own work.
- I have acknowledged all main sources of help.
- Where the thesis is based on work done by myself jointly with others, I have made clear exactly what was done by others and what I have contributed myself.

Signed: Signed by candidate

Date: 02/12/2020

"Those who have the ability to do have the responsibility to do."

The Amazing Spiderman

UNIVERSITY OF CAPE TOWN

Abstract

Faculty of Science
Department of Physics

Doctor of Philosophy

Observing flow using fast neutron radiography and positron emission particle tracking

by Graham Clinton DANIELS

Dynamic flow of material has been studied using fast neutron radiography (FNR) and positron emission particle tracking (PEPT). A new fast neutron imaging system was commissioned at The South African Nuclear Energy Corporation, Pretoria, as part of this study, although FNR measurements were ultimately performed at Physikalisch-Technische Bundesanstalt (PTB), Braunschweig. The PEPT studies were undertaken at the PEPT Cape Town facility located at iThemba LABS, Cape Town. The steady state motion of media, within a laboratory-scale tumbling mill, was studied for a range of speed and media mixes, using both FNR and PEPT. Several operational parameters were derived from the data, which could be related to potential improvements to the milling efficiency. The blending of FNR and PEPT data for the study of steady state flow, was explored for the first time. In addition, the flow of water through porous media was studied using FNR, which enabled the determination of the hydraulic conductivity, and hence intrinsic permeability, of the media within the column. The potential of using FNR, without or without PEPT, for the study of material in motion is discussed.

Acknowledgements

- My deepest gratitude and thanks to God, for blessing me with the opportunity and tools to pursue this dream in the very curious field of physics.

- My supervisor, Professor Andy Buffler, for providing the platform where I could be free to express my passion for science, for his continual support in the construction of this thesis and pushing me to rise to the next level. Your introduction into this world of flow has changed my scientific path for the exciting better.

- My advisor and friend, Dr. Volker Dangendorf for his valuable help and guidance through the FNR experiments, his quality advice and words of wisdom. To the Dangendorf family, for their immense kindness and hospitality shown to this visiting scientist.

- My mentor, Dr. Chris Franklyn, whose motivation set me along this PhD path. His belief in my ability and constant challenging pushed me to aim higher.

- My sister Aliscia, the first Dr. Daniels, without whom I could not have finished this process. Thank you for your guidance and the laughs that got me through the hard times.

- To my dear Parents, Regina and Brendan, who have always been a source and love and encouragement throughout my life, I thank you.

- My mentor, leader and fellow nerd, Dr. Gawie Nothnagel, whose wealth of knowledge in all things physics is a true inspiration that always kept me rooted to the power of pure fundamentals.

- Dr. Tom Leadbeater for his valuable help with all things PEPT and his very well timed words of advice.

- Mr friend, Hantie Labuschagne, for all her proof reading and suggestions that helped this thesis.

- To Mike van Heerden, for his assistance in performing the PEPT experiments.

- My employer, The South African Nuclear Energy Corporation (Necsa), for allowing me the time to conduct this investigation, construct this thesis and for their financial support toward my studies, equipment and travel. The P-LABS team for their continued and valuable support.

- The International Atomic Energy Agency (IAEA) for their financial assistance.

Contents

Declaration of Authorship ii

Abstract iv

Acknowledgements v

Abbreviations xviii

Physical Constants xix

1 Introduction 1
- 1.1 Context of the present work . . . 2
- 1.2 Thesis aim and content . . . 3

2 Fast Neutron Radiography 6
- 2.1 Theory . . . 6
- 2.2 Detection system development . . . 11
  - 2.2.1 Introduction . . . 11
  - 2.2.2 Scintillator . . . 12
  - 2.2.3 Bending mirror . . . 13
  - 2.2.4 Lens . . . 13
  - 2.2.5 Image intensifier . . . 13
  - 2.2.6 Second lens and image intensifier . . . 14
  - 2.2.7 CCD camera and acquisition system . . . 14
- 2.3 Comparative fast neutron systems . . . 14
  - 2.3.1 FANGAS . . . 14
  - 2.3.2 CSIRO . . . 15
  - 2.3.3 PSI system . . . 16
- 2.4 Fast neutron sources . . . 17
  - 2.4.1 Accelerator based . . . 17
  - 2.4.2 Reactor based . . . 23
  - 2.4.3 Neutron generators . . . 25
  - 2.4.4 Spallation . . . 26
- 2.5 Reactions . . . 27
  - 2.5.1 D(d,n)^{3}He . . . 28
  - 2.5.2 ^{9}Be(d,n)^{10}B . . . 31
  - 2.5.3 ^{7}Li(d,n)2^{4}He . . . 35

2.5.4 ^{7}Li(p,n)^{7}Be . . . 35

3 The Fast Neutron Imaging System at Necsa **37**
3.1 Introduction . . . 37
3.2 The Radio Frequency Quadrupole (RFQ) accelerator . . . 37
3.3 Optimization of High Energy Beam Transport system (HEBT) . . . 39
3.3.1 Introduction . . . 39
3.3.2 TRACE 3D optimization for new HEBT configuration . . . 40
3.3.3 Evaluation of TRACE 3D settings for the new HEBT configuration 41
3.4 Preliminary studies using the Necsa Fast Neutron Radiography (FNR) system . . . 45
3.5 Necsa FNR system evaluation . . . 45
3.5.1 Introduction . . . 45
3.5.2 Detector Linearity . . . 45
3.6 Preliminary tests using the Necsa FNR system . . . 47
3.6.1 Introduction . . . 47
3.6.2 Test measurements . . . 47
3.7 Evaluation of samples using FNR on the Necsa system . . . 50
3.7.1 Introduction . . . 50
3.7.2 Sample configuration 1: Polyethylene cylinder, polyethylene block and a steel bolt . . . 50
3.7.3 Sample configuration 2: Aluminium canisters filled with water . 52
3.7.4 Further developments to the Necsa FNR system . . . 53

4 Flow of Media within Tumbling Mills **55**
4.1 Introduction . . . 55
4.2 Experimental setup . . . 59
4.3 Internal mill dynamics and associated parameters . . . 62
4.3.1 Wooden beads . . . 64
4.3.2 Glass beads . . . 68
4.3.3 Wood and plastic beads . . . 72
4.3.4 Wood, steel and plastic beads . . . 76
4.4 Fill factor of the mill charge within the tumbling mill . . . 80
4.4.1 Wooden beads . . . 82
4.4.2 Glass beads . . . 84
4.4.3 Wood and plastic beads . . . 86
4.4.4 Wood, steel and plastic beads . . . 88

5 Combining FNR with Positron Emission Particle Tracking (PEPT) **91**
5.1 Introduction . . . 91
5.2 Experiment . . . 95
5.3 Results . . . 97
5.3.1 Optimization . . . 97

5.3.2 Wooden beads 99
5.3.3 Glass beads 103

6 Flow of Water through Porous Media **110**
6.1 Introduction 110
6.2 Experimental setup 113
6.3 Results 115

7 Conclusion **127**
7.1 Recommendations and Future Work 129

A Resolving Multiple Attenuating Materials using FNR **130**
A.1 Single Energy 130
A.2 Two Energies 131

Bibliography **133**

List of Figures

1.1 Fast neutron radiograph of a skull sample measured at the Necsa RFQ facility . . . 2
1.2 Identification of the TATP surrogate using FNR. The figure is taken from [2] with permission of one of the authors . . . 2

2.1 Method for performing radiography on samples . . . 7
2.2 Neutron interaction cross-section of hydrogen, oxygen, carbon and nitrogen in the 10^{-6} to 10^{8} eV neutron energy range . . . 8
2.3 Fast neutron interaction cross-section of hydrogen, oxygen, carbon and nitrogen in the 10^{6} to 10^{8} eV neutron energy range . . . 8
2.4 Optical path of a radiography system . . . 9
2.5 Conceptual method for the implementation of the Beer-Lambert Law . . . 10
2.6 The sample, above, with the resulting FANGAS radiographs presented in (a) and (b), below . . . 15
2.7 Image obtained using the CSIRO imaging system at Brisbane . . . 16
2.8 Image obtained from the PSI imaging system . . . 16
2.9 Conceptual design for a linear accelerating system . . . 20
2.10 Representation of the RFQ rods showing the modulation that induces the acceleration field . . . 20
2.11 Concept representation for the operation of a cyclotron accelerator . . . 21
2.12 Concept representation for the operation of a synchrotron accelerator . . . 23
2.13 A typical neutron energy spectrum from a nuclear fission reactor . . . 25
2.14 Time-averaged neutron yield per unit beam power at the PSI neutron generator . . . 27
2.15 Calculated neutron spectra for fission and spallation using a tungsten target . . . 28
2.16 Total neutron yield obtained when using a thick target . . . 29
2.17 Spectral yield of *D-D* neutrons versus deuterium gas cell pressure and Neutron Spectrum from the *D(d,n)* reaction measured at various angles . . . 30
2.18 Relation of neutron energy to deuteron energy for the *D-D* reaction . . . 31
2.19 Multiple foil activation unfolding of neutron spectra from a thick Be target 32
2.20 Neutron spectra produced by 1.45 MeV deuterons on a 8.0 μm thick beryllium target and by 2.30 MeV protons on lithium . . . 33
2.21 The stopping power of the ^{9}Be target to deuterons . . . 34
2.22 Neutron energy spectra of the ^{9}Be neutron source with the thick beryllium target at different incident deuteron energies . . . 34

2.23 Neutron yield from ^{7}Li(d,n) reaction at 0° for a thick metallic ^{7}Li target for E_d = 2.0 MeV . . . 35
2.24 Double differential neutrons yield from ^{7}Li(p,n) reaction for angle 0°, 45° and 90° for thick metallic ^{7}Li target, initial proton energy 2.30 MeV . 36

3.1 Layout of the original 4.0 to 5.0 MeV D^{+} RFQ system at Necsa . . . 38
3.2 TRACE 3D simulation of the initial HEBT configuration using the original focusing gradient values for *Q1*, *Q2* and *Q3* showing how the input beam shape is transformed to the beam at target shape . . . 41
3.3 TRACE 3D simulation of the new HEBT configuration matched to obtain the smallest possible beam spot size showing how the beam is transformed from the input beam shape to the beam at target shape . . . 42
3.4 Aluminium target after 1.50 minute exposure to an accelerating deuteron beam at a peak beam current of 1.0 mA . . . 43
3.5 Aluminium target after 8.0 minute exposure to an accelerating deuteron beam at a peak beam current of 1.0 mA . . . 43
3.6 Illustration of quad analyser used to determine the beam position, incident onto the target . . . 43
3.7 Oscilliscope showing the equal peaks of the quadrant analyser . . . 44
3.8 Fast neutron radiograph of a skull obtained at the RFQ facility using the Necsa FNR system . . . 46
3.9 Layout of the FNR system at Necsa used to perform the preliminary experiments . . . 46
3.10 FNR result for polyethylene cylinder, water vial filled with water and a steel bolt using the Necsa FNR system . . . 48
3.11 FNR for water, propanol and a mixture of water and sugar obtained using the Necsa FNR system . . . 48
3.12 FNR for sugar, propanol and a mixture of water and sugar obtained using the Necsa FNR system . . . 49
3.13 Sample configuration 1 investigated using the Necsa FNR system . . . 51
3.14 FNR of sample configuration 1 . . . 51
3.15 Sample configuration 2 investigated using the Necsa FNR system . . . 52
3.16 FNR of sample configuration 2 . . . 53
3.17 The design of the optical components of the new FNR system for Necsa 54

4.1 The different phases formed by the charge within the tumbling mill . . . 56
4.2 Representation of the mill charge showing the total ball angle and average ball lift . . . 57
4.3 Important regions and angles of mill charge formed during tumbling . . 58
4.4 Experimental setup for the tumbling mill placed on the rollers and the TRION fast neutron radiography system [78] . . . 60

4.5 Important regions and angles of the mill charge made up of 10.0 mm wooden beads rotating at 47.0% V_c occurring during the tumbling phase and acquired using the TRION system 63
4.6 Fast neutron radiographs showing the phases formed by the mill charge comprised of 10.0 mm diameter wooden beads, for different percentages of the critical speed at (a) rest, (b) 19.5% V_c, (c) 31.0% V_c, (d) 39.0% V_c, (e) 47.0% V_c, (f) 54.5% V_c, (g) 78.0% V_c and (h) 117.0% V_c 65
4.7 The total ball angle, average ball lift and power usage of the tumbling mill system with a mill charge comprised of 10.0 mm wooden beads . . 66
4.8 Area of regions formed by the mill charge comprised of 10.0 mm wooden beads as a function of the percentage of the critical speed 66
4.9 Angles formed by the mill charge comprised of 10.0 mm wooden beads as a function of the percentage of the critical speed 67
4.10 The head height formed by the mill charge comprised of 10.0 mm wooden beads as a function of the percentage of the critical speed 67
4.11 Fast neutron radiographs showing the phases formed by the mill charge comprised of 6.0 mm, 8.0 mm and 12.0 mm diameter glass beads, for different percentages of the critical speed with (a) rest, (b) 19.5% V_c, (c) 31.0% V_c, (d) 39.0% V_c, (e) 47.0% V_c, (f) 54.5% V_c, (g) 62.0% V_c, (h) 70.0% V_c and (i) 101.0% V_c 69
4.12 The total ball angle, average ball lift and power usage of the tumbling mill system with a mill charge comprised of 6.0 mm, 8.0 mm and 12.0 mm glass beads 70
4.13 Area of regions formed by the mill charge comprised of a mixture of 6.0 mm, 8.0 mm and 12.0 mm diameter glass beads as a function of the percentage of the critical speed 70
4.14 Angles formed by the mill charge comprised of a mixture of 6.0 mm, 8.0 mm and 12.0 mm diameter glass beads as a function of the percentage of the critical speed 71
4.15 The head height formed by the mill charge comprised of 6.0 mm, 8.0 mm and 12.0 mm glass beads as a function of the percentage of the critical speed 71
4.16 Fast neutron radiographs showing the phases formed by the mill charge comprised of 6.0 mm and 5.50 mm diameter wood and plastic beads, for different percentages of the critical speed with (a) rest, (b) 19.5% V_c, (c) 31.0% V_c, (d) 39.0% V_c, (e) 47.0% V_c, (f) 54.5% V_c, (g) 78.0% V_c and (h) 101.0% V_c 73
4.17 The total ball angle, average ball lift and power usage of the tumbling mill system with a mill charge comprised of 6.0 mm diameter wooden beads and 5.50 mm diameter plastic beads 74

4.18 Area of regions formed by the mill charge comprised of a mixture of 6.0 mm diameter wooden beads and 5.50 mm diameter plastic beads as a function of the percentage of the critical speed 74
4.19 Angles of regions formed by the mill charge comprised of a mixture of 6.0 mm diameter wooden beads and 5.50 mm diameter plastic beads as a function of the percentage of the critical speed 75
4.20 The head height formed by the mill charge comprised of 6.0 mm diameter wooden beads and 5.50 mm diameter plastic beads as a function of the percentage of the critical speed 75
4.21 Fast neutron radiographs showing the phases formed by the mill charge comprised of 6.0 mm diameter wooden, 5.0 mm diameter steel and 5.50 mm diameter plastic beads, for different percentages of the critical speed with (a) rest, (b) 19.5% V_c, (c) 31.0% V_c, (d) 39.0% V_c, (e) 47.0% V_c, (f) 54.5% V_c, (g) 62.0% V_c, (h) 70.0% V_c,(i) 78.0% V_c and (j) 101.0% V_c 77
4.22 The total ball angle, average ball lift and power usage of the tumbling mill system with a mill charge comprised of 6.0 mm diameter wood beads, 5.0 mm diameter steel beads and 5.50 mm diameter plastic beads 78
4.23 Area of regions formed by the mill charge comprised of a mixture of 6.0 mm diameter wooden beads, 5.0 mm diameter steel beads and 5.50 mm diameter plastic beads as a function of the percentage of the critical speed 78
4.24 Angles formed by the mill charge comprised of a mixture of 6.0 mm diameter wooden beads, 5.0 mm diameter steel beads and 5.50 mm diameter plastic beads as a function of the percentage of the critical speed 79
4.25 The head height formed by the mill charge comprised of 6.0 mm diameter wooden beads, 5.0 mm diameter steel beads and 5.50 mm diameter plastic beads as a function of the percentage of the critical speed 79
4.26 The region of interest used to calculate the length of the mill charge at different rotation speeds 81
4.27 I/I_0 for the 10.0 mm diameter wooden beads making up the mill charge, through the defined region of interest, for speeds of 47.0%, 54.5% and 78.0% of the critical speed 83
4.28 I/I_0 for the 10.0 mm diameter wooden beads making up the mill charge, through the defined region of interest, for the rest and full centrifuge condition 83
4.29 Fill factor of the mill charge, x_{wood}, that attenuates the fast neutrons at varying rotation speeds 84
4.30 I/I_0 for the 6.0 mm, 8.0 mm and 12.0 mm diameter glass beads making up the mill charge, through the defined region of interest, for speeds of 54.5%, 70.0% and 78.0% of the critical speed 85
4.31 I/I_0 for the 6.0 mm, 8.0 mm and 12.0 mm diameter glass beads making up the mill charge, through the defined region of interest, for the rest and full centrifuge condition 85

4.32 Fill factor of the mill charge, x_{glass}, that attenuates the fast neutrons at varying rotation speeds . . . 86
4.33 I/I_0 for the 6.0 mm diameter wooden beads and 5.50 mm diameter plastic beads, through the defined region of interest, for speeds of 47.0%, 54.5% and 78.0% of the critical speed . . . 87
4.34 I/I_0 for the 6.0 mm diameter wooden beads and 5.50 mm diameter plastic beads making up the mill charge, through the defined region of interest, for the rest and full centrifuge condition . . . 87
4.35 Fill factor of the mill charge, $x_{wood/plastic}$, that attenuates the fast neutrons at varying rotation speeds . . . 88
4.36 I/I_0 for the 6.0 mm diameter wooden beads, 5.0 mm steel beads and 5.50 mm diameter plastic beads, through the defined region of interest, for speeds of 47.0%, 54.5%, 62.0%, 70.0% and 78.0% of the critical speed . . . 89
4.37 I/I_0 for the 6.0 mm diameter wooden beads, 5.0 mm diameter steel beads and 5.50 mm diameter plastic beads making up the mill charge, through the defined region of interest, for the rest and full centrifuge condition . 89
4.38 Fill factor of the mill charge, $x_{wood/plastic/steel}$, that attenuates the fast neutrons at varying rotation speeds . . . 90

5.1 The ECAT EXACT3D HR++ PET scanner at PEPT Cape Town, which has been adapted for PEPT . . . 92
5.2 An axial projection of one thousand lines of response measured in about one second by the ECAT EXACT3D HR++ PET scanner (a) before and (b) after application of the PEPT algorithm . . . 93
5.3 An example of a PEPT measurement of (a) a few thousand locations (z-axis projection) of a tracer moving within a small rotating drum filled with glass beads of diameter 5.0 mm; and (b) the average velocity field determined for the tumbling tracer . . . 94
5.4 Experimental setup at PEPT Cape Town with the rollers and mill set in the middle of the ECAT EXACT3D HR++ PET Scanner . . . 96
5.5 Uncertainties in the LOR reduction as a function of f and N, measured for a stationary tracer positioned near the centre of the ECAT EXACT3D HR++ scanner for the 10.0 mm wooden tracer . . . 98
5.6 Uncertainties in the LOR reduction as a function of f and N, measured for a stationary tracer positioned near the centre of the ECAT EXACT3D HR++ PET scanner for (a) 8.0 mm glass tracer and (b) 12.0 mm glass tracer 98
5.7 Results for the 10.0 mm wooden beads, showing (a) the PEPT occupancy xy projection and (b) the associated fast neutron radiograph for the same rotation speed . . . 100
5.8 PEPT occupancy zy projection for the 10.0 mm wooden beads in the mill charge, during rotation . . . 101

5.9 Speed of the tracer in the *xy* projection for a mill charge comprised of 10.0 mm wooden beads . . . 102
5.10 The average velocity field in the *xy* projection for a mill charge comprised of 10.0 mm wooden beads . . . 103
5.11 Results showing the PEPT occupancy *xy* projections for (a) 8.0 mm glass tracer, (b) 12.0 mm glass tracer and (c) the FNR image at the same rotation speed . . . 105
5.12 Results showing the occupancy *zy* projection for the mix of glass beads with (a) 8.0 mm glass tracer and (b) 12.0 mm glass tracer . . . 106
5.13 Speed of the tracer in the *xy* projection for (a) 8.0 mm glass tracer and (b) 12.0 mm glass tracer . . . 108
5.14 The average velocity field in the *xy* projection for a mill charge comprised of (a) 8.0 mm glass tracer and (b) 12.0 mm glass tracer . . . 109

6.1 Representation of the application of Darcy's Law for the flow of water through porous sand . . . 111
6.2 Conceptual model for capillary rise of water in sand with a water content curve on the right . . . 113
6.3 Experimental setup of the sample showing the directional flow of water while employing the constant head method to determine the hydraulic conductivity . . . 114
6.4 Schematic showing the flow of water for the setup presented in Figure 6.3 115
6.5 Fast neutron radiographs showing the absorption of water in a cylinder of sand. The increasing presence of water in the sand is represented by the dark region that grows as a function of time . . . 116
6.6 The regions of interest, referred to in Table 6.3, used to examine the flow of water through the sand sample . . . 117
6.7 Comparing the transmission of fast neutrons through the sample during water absorption examined at different regions of interest . . . 118
6.8 Volume contribution for a mixed sample . . . 119
6.9 Increasing volume contribution of water in sand, observed over the acquisition time . . . 120
6.10 Water content of the sample along the suction head obtained at times of 12 s, 240 s, 360 s and 480 s . . . 121
6.11 The hydraulic conductivity along the suction head of the sample obtained from Gardner's Equation at different observation times . . . 122
6.12 Regions used to obtain the required parameters for application in Darcy's Law . . . 123
6.13 Hydraulic conductivity of the sample calculated using Darcy's Law, along the length of the sample . . . 125

6.14 The comparison of the hydraulic conductivity between Darcy's Law and Gardner's Equation over time on the lower x-axis and length on the upper x-axis 126

A.1 Three attenuating materials in a composite system 131

List of Tables

3.1 Specified and achieved values for the RFQ accelerator system 39
3.2 Specifications for focusing magnets forming part of the new HEBT setup 40
3.3 Comparison between the counts from the 30.0 minute and 15.0 minute acquisitions 46
3.4 Samples used to perform the preliminary quantitative FNR investigation 50

4.1 Attenuation coefficient of beads making up the mill charge 81

5.1 Characteristics of glass beads used to perform the PEPT experiments . . 103

6.1 The effective thickness of each region of interest used in the analysis to calculate the hydraulic conductivity k 115
6.2 The inverse air-entry head (τ) values for the sample taken at different times during the absorption of water 120
6.3 Input parameters for Darcy's Law to calculate the hydraulic conductivity, k 124
6.4 Comparison between the Darcy's Law calculation and Gardner's Equation calculation 124

Abbreviations

CCD	**C**harge-**C**oupled **D**evice
CRP	**C**oordinated **R**esearch **P**roject
CSIRO	**C**ommonwealth **S**cientific and **I**ndustrial **R**esearch **O**rganisation
DC	**D**irect **C**urrent
ESS	**E**uropean **S**pallation **S**ource
FANGAS	**FA**st **N**eutron **GA**s filled imaging **S**ystem
FLI	**F**inger **L**ake **I**nstruments
FNR	**F**ast **N**eutron **R**adiography
HEBT	**H**igh **E**nergy **B**eam **T**ransport
HV	**H**igh **V**oltage
IAEA	**I**nternational **A**tomic **E**nergy **A**gency
iThemba-**LABS**	iThemba - **L**aboratory for **A**ccelerator **B**ased **S**cience
LHC	**L**arge **H**adron **C**ollider
LOR	**L**ine **O**f **R**esponse
MCP	**M**ulti **C**hannel **P**late
OTIFANTI	**O**p**TI**cal **F**ast **N**eu**T**ron **I**maging system
PC	**P**ersonal **C**omputer
PEPT	**P**ositron **E**mission **P**article **T**racking
PET	**P**ositron **E**mission **T**omography
P-LABS	**P**elindaba **L**aboratories for **A**ccelerator and **B**eam-line **S**cience
PSI	**P**aul **S**cherrer **I**nstitute
PTB	**P**hysikalisch-**T**echnische **B**undesanstalt
RF	**R**adio **F**requency
RFQ	**R**adio **F**requency **Q**uadrupole
RoI	**R**egion **o**f **I**nterest
TATP	**T**ri**A**cetone **T**ri**P**eroxide
ToF	**T**ime **o**f **F**light
VdG	**V**an **d**er **G**raaff

Physical Constants

Symbol	Name	Value	Unit
π	Pi	3.14159265359	
g	Acceleration due to gravity	9.80665	$\mathrm{m\ s^{-2}}$

For my loved ones.. . .

Chapter 1

Introduction

Fast Neutron Radiograpy (FNR) has matured into being widely used for the interrogation of the structural and elemental composition of materials and objects in a wide range of contexts. This includes the examination of the steady state of dynamic flow, hydraulic conductivity observations, cultural heritage studies and security applications. Fast neutrons offer high penetrability and their interaction cross-section exhibit energy dependent isotope specific resonance features that can be exploited. In recent years advances in neutron production and neutron detection has allowed FNR to find application in contexts which require higher fluxes and faster imaging. The higher penetrability and element specific interaction of fast neutrons allow for examination of larger systems and/or deliver additional information beyond that achieved when using thermal, epithermal or cold neutrons or X-rays as a probe.

For example, applications in the field of cultural heritage were carried out at the Radio Frequency Quadrupole (RFQ) facility at Necsa, South Africa, from which a radiograph of a skull was examined, in-situ, using a 7.0 MeV neutron beam, as shown in Figure 1.1 [1]. This was the very first application of FNR for cultural heritage samples in South Africa. Both the frontal and maxillary sinus cavities can be seen, the shapes of which are of high importance when conducting evolutionary studies of humans [1]. As another example, fast neutrons are used for the detection of contraband. The example presented in Figure 1.2 [2] identifies a nitrogen free improvised explosive, the oxygen rich TriAcetone TriPeroxide (TATP) surrogate (or substitute) of same density and elemental composition. Figure 1.2a shows a setup having six milk bottles and four vials filled with TATP surrogate and water, with a TATP surrogate placed within the upper middle milk bottle. A combined neutron and gamma radiograph is presented in Figure 1.2b however this does not reveal the TATP surrogate placed inside the milk bottle. By making use of the resonance effect of fast neutrons to specific elements and at specific energies one can reconstruct areal densities of the elements to determine their composition. This is done by employing Fast Neutron Resonance Radiography (FNRR) [2] and the result is presented in Figure 1.2c where only the vials having TATP present can be seen. This has a direct benefit to applications in security.

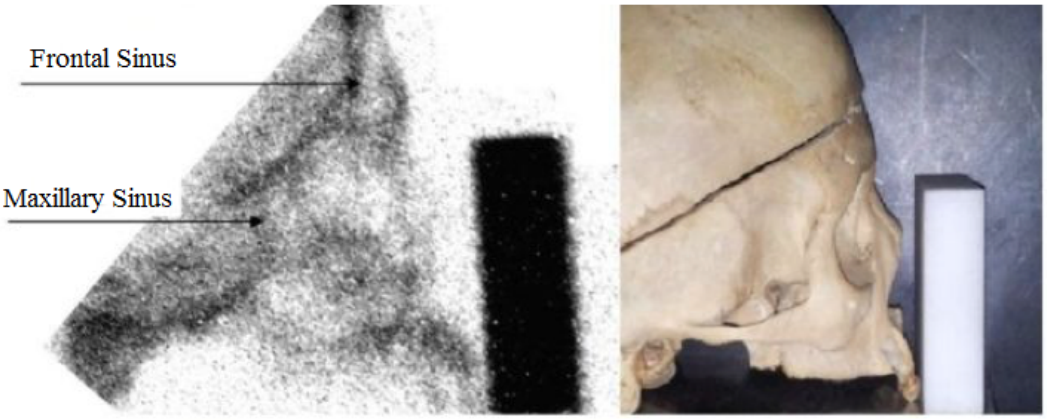

FIGURE 1.1: Fast neutron radiograph of a skull sample measured at the Necsa RFQ facility

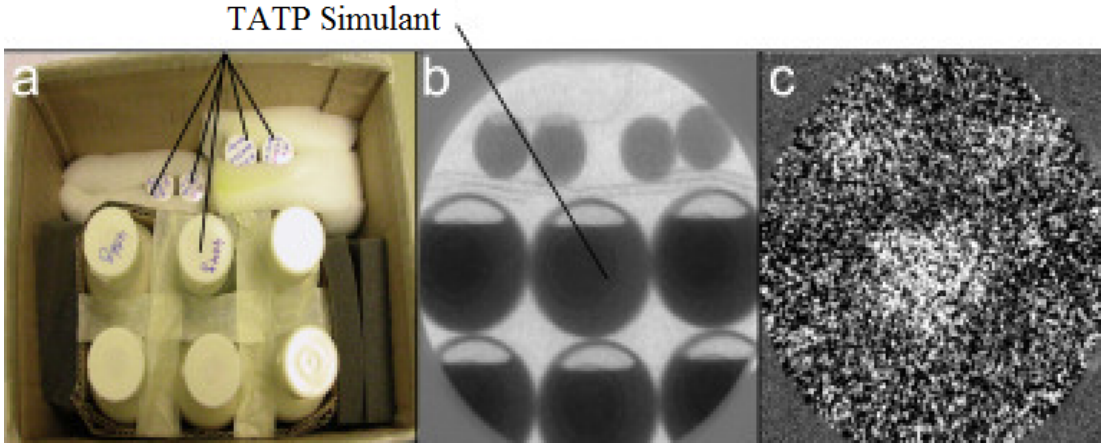

FIGURE 1.2: Identification of the TATP surrogate using FNR. The figure is taken from [2] with permission of one of the authors

1.1 Context of the present work

Understanding the nature of the steady state of dynamic flow within complex moving systems is important in modelling their behaviour. This will allow for a greater optimization of the system's design and construction, which will have a direct impact in increasing efficiency. Two such systems in which the steady state of dynamic flow is examined, are the tumbling mill system, where the mill charge reaches a steady shape for a set rotation speed, and the hydraulic conductivity of sand (k) where the steady state FNR is captured rapidly, to determine the flow of water through the sand which is used to calculate k.

Tumbling mill dynamics are an important part of mineral processing systems, which use the comminution process to facilitate the breakdown of a large object into smaller pieces through crushing and grinding. The shape and flow of the mill charge

is important in ascertaining the best comminution of the mill charge. This investigation makes use of the FNR technique to examine the behaviour of the mill charge which varies between steel, wood, glass and plastic beads. The layering and shape of the mill charge are observed using FNR. From this the motion, a density distribution and effective mixing experienced by the mill charge are inferred and related to comminution. The PEPT technique is also used to determine the shape of the mill charge, which follows the ^{68}Ga positron emitter as it moves within a tracer particle that forms part of the mill charge. This yields a representation of the shape of the mill charge during rotation, which is then compared to the results obtained when using fast neutron radiography.

To study the flow of water through porous media, FNR is employed to determine the intrinsic properties of sand, with the focus being the determination of the hydraulic conductivity, k. This hydraulic conductivity is the ability of the sand to transmit water, the knowledge of which is of importance when planning earth storage leakages and water control structures. The constant head method is applied for this analysis. Examining the attenuation of fast neutrons by water, shows the evolution of the waterfront and from the resulting radiograph, the parameters required to determine the hydraulic conductivity are obtained. These parameters are input into Darcy's Law [3] and Gardner's Equation [4] and are used to calculate the hydraulic conductivity of the sand. Fast neutron radiography is shown to obtain unique information of the water absorption through sand, from which the hydraulic conductivity, k, is calculated.

The research carried out during this thesis applied, for the first time, the technique of fast neutron radiography to tumbling mill systems. Important operational parameters are extracted from the resulting fast neutron radiographs once the steady state condition of the mill charge is reached. Fast neutron radiography is also applied to observe the flow of water through sand, examining a thicker sample then previously tested using other techniques. A first ever comparison is made between fast neutron radiography and positron emission particle tracking, when applied to the tumbling mill system. This highlights the complementarity of transmission and emission radiography.

1.2 Thesis aim and content

This thesis aims to show the requirements of a fast neutron radiography system and the application of the fast neutron radiography technique to the steady state of dynamic flow and the flow of water through porous media.

The study will show the effectiveness of fast neutron radiography as a capable technique which enables the visualization of the internal dynamics of a mill charge

under rotation and also the flow of water through sand. The study of the flow within a tumbling mill is also examined and verified using the Positron Emission Particle Tracking (PEPT) technique.

To achieve this, an available RFQ accelerator-based neutron source at Necsa was upgraded and evaluated. The development and design of a new FNR imaging system is also presented which will make higher resolution FNR possible at this RFQ accelerator-based neutron source of Necsa, South Africa. The FNR technique is applied to investigate the dynamics of mixing processes within a tumbling mill and hydraulic conductivity studies, where the flow of water through porous media was studied. Due to the lack of availability of the Necsa accelerator at the time of this work these studies were performed at the PTB Braunschweig accelerator facility. A final examination of the internal dynamics of a mill charge under rotation is conducted using PEPT and its results are compared with the corresponding results of the FNR investigation.

This examination is verified using acquired experimental data, which is then applied to well-established theories, to determine the important parameters required for hydraulic conductivity, internal mill dynamics and PEPT data. In addition, the optimization of the RFQ facility components at Necsa is experimentally verified by observing the beam shape and beam current on the target. The Necsa FNR system is also tested by conducting initial tests at the RFQ facility.

The contents of each following chapter is summarized here. Chapter 2 gives an overview of the theory of FNR and the description of the detection systems used for this technique. A new generation of fast neutron detectors and an overview of types of fast neutron sources are also described in detail.

Chapter 3 details the development of an operational accelerator-based FNR system, beginning with the RFQ facility and the upgrades that were performed to optimize both the neutron output and the experimental setup. The radiography system and initial test measurements that were conducted at this facility are presented.

In Chapter 4, an application of the technique of fast neutron radiography to the tumbling mill system is presented. The internal dynamics of the tumbling mill during rotation and its mixing are focused on, with the important mill parameters obtained from the resulting radiographs.

Chapter 5 presents the results achieved when the flow of the internal mill charge is investigated using the PEPT technique, which makes use of a ^{68}Ga positron emitter, to image the flow of the mill charge for different rotation speeds and mill charge compositions.

Chapter 6 presents the flow of water through porous media, with the resulting radiographs used to calculate the hydraulic conductivity (k) using both Darcy's Law and Gardner's Equation methods.

In Chapter 7, the conclusion and recommendations for future work are presented.

Appendix A shows the mathematics and the requirements needed to resolve three different attenuating materials within a sample. The results of the calculation show that two different fast neutron energies are required to achieve this distinction.

Chapter 2

Fast Neutron Radiography

2.1 Theory

Radiography is an imaging technique that uses the interaction between a penetration radiation and the atoms of an object to view its internal structure. Initially, the application used x-rays, which senses the local electron densities inside the object. Later other radiation types like neutrons, protons and even muons were also used as interrogating radiation for these types of investigations. Different radiation has a different and unique interaction with the matter of the object and therefore provide complementary information about the composition of the sample. The principal concept of the radiographical technique used in this work is shown in Figure 2.1, where interrogating radiation, neutrons in this case, probes the object. In FNR the neutrons pass through the object and interact with the nuclei by scattering or absorption. The probability of an interaction depends on the nuclear properties of the target atoms and is therefore isotope specific. This accounts for the unique radiographic information available with neutron beams. The neutrons transmitted through the object without interaction may then be detected by a scintillation screen that converts the neutrons into photons, thus presenting an optical image of the spatial distribution of the transmitted neutrons.

This optical image is captured by a digital CCD camera system [5].

Compared to the much more common X-ray imaging techniques, which are prevalent in medicine, industry and research, neutron radiography is still a very small field. This is due to the requirements of a high flux neutron source, for an acceptable signal to noise ratio and the sensitivity of detectors [6][7], which has been a major limiting factor to the advancement of this technique. As neutrons carry no net charge, their interaction cross-section with matter is different from X-rays and occurs mainly through nuclear forces (mechanical or magnetic interaction) [8].

Neutrons interact with matter or, more specifically, the atoms of matter in their own unique way with the interaction only dependent on the specific atom and incumbent neutron energy. The cross section does not depend strongly on the atomic number. Each nucleus comprises a set of protons and neutrons and an electron cloud surrounding it. The electron cloud holds the initial negative charge that an incoming

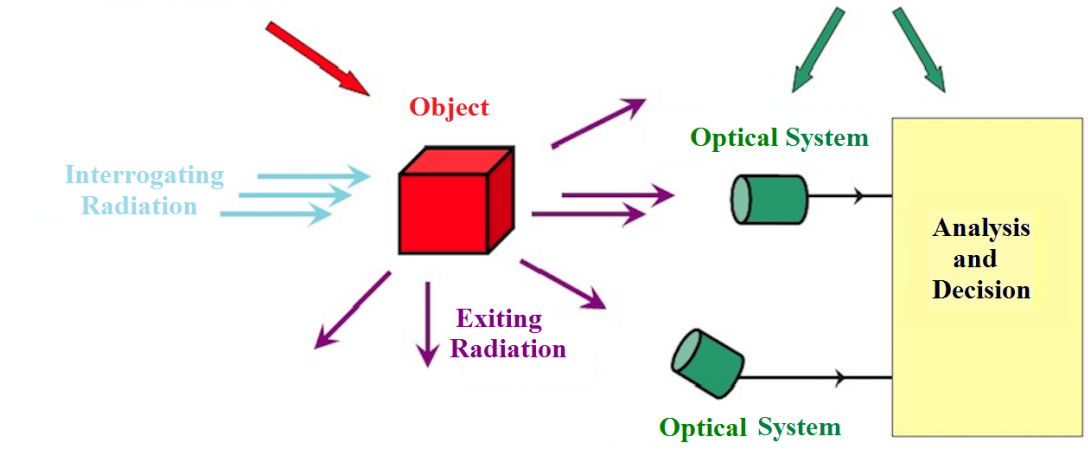

FIGURE 2.1: Method for performing radiography on samples

particle can see, so here the Coulombic interaction can take place. This is the case for x-rays, as they interact with the electron cloud surrounding the nucleus. This makes the x-ray interaction dependent on the atomic number. However, as neutrons are electrically neutral, liberated neutrons pass through the electron cloud and interact with the nucleus directly, this dependency being highlighted in Figure 2.2 and Figure 2.3 [9], showing the fast neutron interaction cross-section and the resonance features of fast neutrons for hydrogen, oxygen, nitrogen and carbon.

The interaction cross-section (the probability of the neutrons interacting with the target material) for fast neutrons, Figure 2.3 [9], shows how each neutron will interact with different elements. Each element has a different neutron interaction cross section at specific neutron energies as shown in Figure 2.2. The behaviour of the neutron interaction cross section is predictable in the cold, epithermal and thermal regime and becomes unpredictable in the fast neutron regime as shown in Figure 2.3.

At very low neutron energies, so called thermal or cold neutrons, the cross-sections are significantly higher than for fast neutrons. Therefore, thermal and cold neutrons have a shorter penetration depth into the investigating object and this limits the thickness of your object under investigation. The fast neutrons penetrate further into the object and thus, give one the ability to investigate also larger objects of up to meters in size.

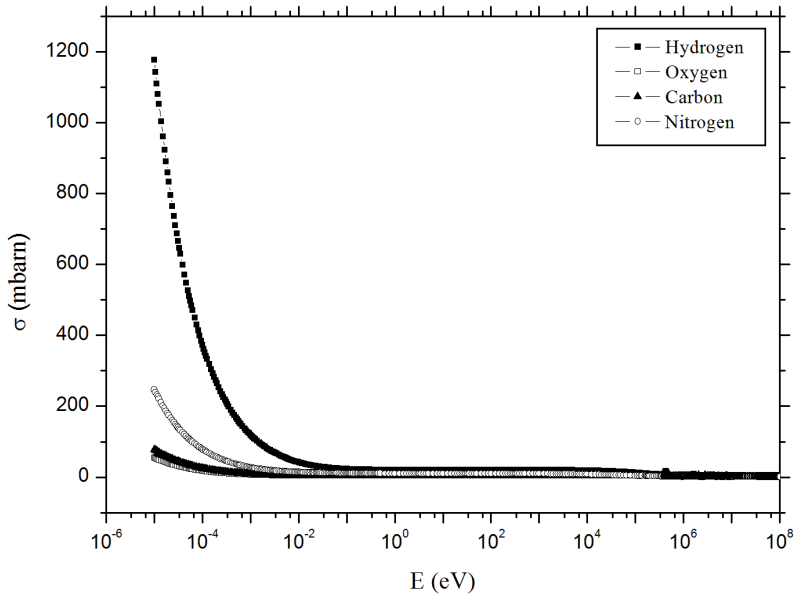

FIGURE 2.2: Neutron interaction cross-section of hydrogen, oxygen, carbon and nitrogen in the 10^{-6} to 10^{8} eV neutron energy range

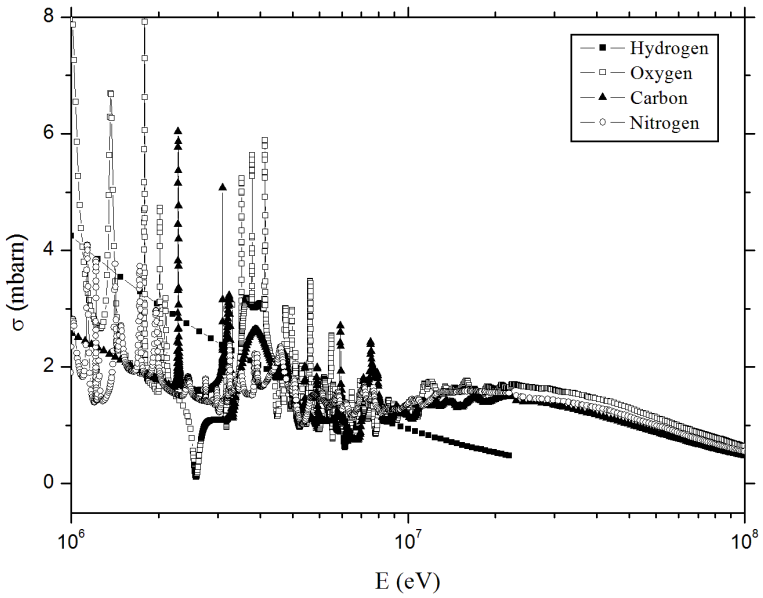

FIGURE 2.3: Fast neutron interaction cross-section of hydrogen, oxygen, carbon and nitrogen in the 10^{6} to 10^{8} eV neutron energy range

Depending on the energy of the incoming neutron, the number of interactions per unit volume is proportional to the neutron cross section of interaction with a given material [8]. This nature of neutrons allows one to extract information from the elements with a lower atomic number, within the sample, making this a complementary technique to x-rays whose cross section are higher for materials having elements with a higher atomic number [6].

Neutron imaging detectors have gone through a vast array of development over recent years. One of the early imaging techniques for slow neutrons employed foils [10] that would convert the neutron signal to an electron or alpha particle which in turn causes a photon output within another foil. Another system used the build-up of radioactivity on a foil and later transferred this to a photographic film in a dark room environment [10]. In this case, a low neutron flux yields positive results, however, for fast neutrons, a lower cross-section of interaction for metals makes the foil activation effect required to retrieve an image, difficult. Another technique uses a scintillator directly converting a fast neutron to a photon and then an image recorder, CCD camera, capturing the photons. The setup for the optical path of this latter setup is presented in Figure 2.4.

The scintillator is made up of material with the highest possible cross-section for the neutron to photon conversion. An image intensifier system then amplifies the photon signal and a lens mechanism is used to de-magnify and focus the image onto the camera's CCD chip.

The scintillators can either be plastic, plastic fibre or a ^{6}Li based scintillator, depending on the neutron energy to be detected. When, for example, fast neutrons interact with the atoms of a plastic scintillator the dominant interaction is elastic scattering with a recoil proton, transferring on average 50% or the kinetic energy of the neutron

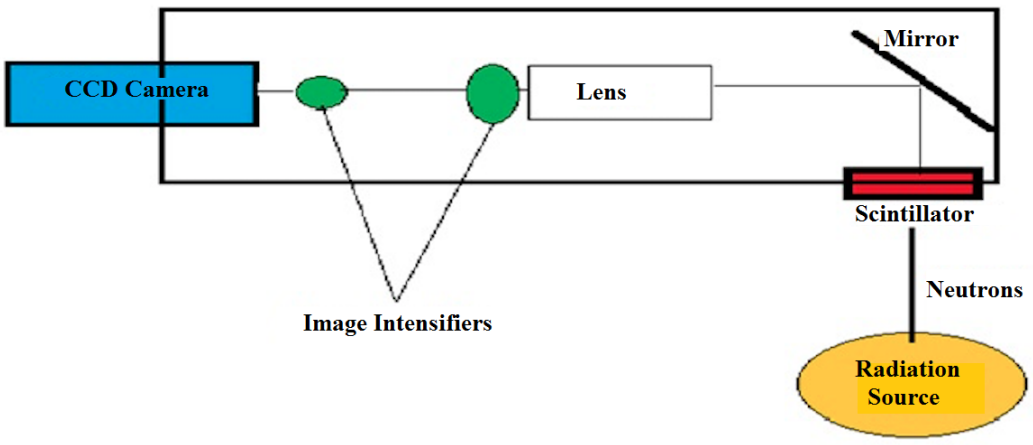

FIGURE 2.4: Optical path of a radiography system

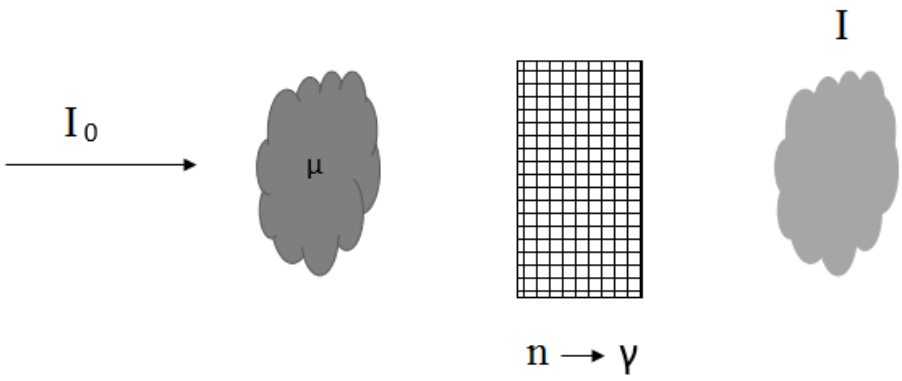

FIGURE 2.5: Conceptual method for the implementation of the Beer-Lambert Law

to the proton. The proton transfers its energy in close vicinity of the neutron interaction point to the molecules and atoms of the scintillator by ionization and excitation. In a scintillator a significant part of this energy is then converted to visible photons. Their local distribution in the scintillator screen represents the local flux density of the neutrons in the screen. Detecting their distribution via an optical system delivers the 2-dimensional spatial distribution of the neutrons which penetrated the object under investigation. The choice of scintillator depends on the energy of the neutrons, the required resolution, neutron flux from the source and makeup of the optical detection system.The mirror in Figure 2.4 is to protect the electronic components (camera) from direct neutron exposure [5].

The optical image of the local neutron flux which emanates from the scintillator screen, is then de-magnified and focused by a lens onto the photo-cathode of an image intensifier. In the last stage, the amplified image which appears on the phosphor of the intensifier is focussed by a further lens or a fibre optical taper to the CCD chip of a camera. This image is then captured on a computer for analysis [11].

The analysis of the captured images follows the principles shown in Figure 2.5, where I_0 is the image taken without an object present, also known as the flat field. I is the image acquired with the object in the beam path and μ is the total attenuation coefficient of the object with thickness, x. To process the image, the Beer-Lambert Law is used [12][13], which for multiple attenuating materials is,

$$I = I_0 \exp\left(-\Sigma_i \mu_i x_i\right) \tag{2.1}$$

where μ_i is the attenuating of material i with thickness x_i.

The Beer-Lambert Law, Equation (2.1), describes the attenuation of the neutrons as they pass through a material and the associated properties of that material. Lambert found that the ability of radiation to travel through an object is related to its thickness whereas, Beer found it was related to the concentration of the attenuation species of the object, i.e. the total attenuation coefficient [13].

The flat field correction corrects the transmission image for inhomogeneous spatial distribution of the neutron field and possible field distortions by the optical system and the CCD camera. Due to the optical system's electronics, further corrections are made to obtain the best image quality [14][15]. If a CCD readout is used as in [11], [14], [15] the following types of noise must be corrected for:

- Readout noise (R/O Noise) – system noise resulting from the charge carriers in the CCD, converting charge carriers into a voltage signal that contributes to the noise signal.

- Background noise – Inherent noise experienced in all detectors that is a result of your design, setup and background effects, this is taken when no beam is present.

- Dark current – This is a thermal effect where electron exposure causes the thermal energy to increase to an intermediate state and produce more electrons, which add to the noise.

These effects are considered by taking an image with the neutron beam-off. It is subtracted, pixel-by-pixel, from the transmission image and the Flat-field image before the flat-field correction is performed.

2.2 Detection system development

2.2.1 Introduction

The components of the fast neutron imaging system, shown in Figure 2.4, are detailed with focus on the PTB (TRION) [11][16] and Necsa systems [1]. These detectors were used for the fast neutron radiographs obtained for this thesis' study.

Plans to upgrade the current Necsa imaging system is under way and will be mentioned at the end of Chapter 3.

The optical arrangement, as in Figure 2.4, aims to convert neutrons to photons in a flat scintillation screen, then focussing and de-magnifying the image by a lens to an image intensifier and finally capturing this image by a CCD camera.

2.2.2 Scintillator

Fast-neutron detection is most efficient using organic, i.e. hydrogen rich scintillators. Within the scintillator, the neutrons are scattered by the hydrogen nuclei which recoils, ionizes and excites the molecules of the scintillator which, after several internal energy transitions by wave length shifting molecules, induces the emission of visible light [17].

Organic scintillators (plastics and liquids) [18] are comprised of hydrocarbon compounds with linked or condensed benzene-ring structures. Valence electrons of the scintillators matrix molecule are excited by a recoil proton or its secondary electrons and transfer their energy to radiant states of so called fluors. These fluors de-excite very fast and produce visible scintillation light. The plastic scintillation has different light yields for different charged particles and has an inherent temperature dependence, but these remain consistent for a specific setting.

The scintillation output of a typical plastic scintillator emits light at a wavelength of 425.0 nm [19] with a high output and decay time in the nanosecond regime (which assists with noise reduction). Plastic scintillators can be cast into shapes that are required to suit the experimental needs.

Plastic scintillation sheets are used to produce light from the incident neutrons with the major criteria being the interaction efficiency that ranges between 50% - 70% [19] neutron absorption cross-section for the scintillator and the scintillation decay time in the nanosecond regime. The thickness of a scintillator in the form of a fully transparent slab affects the quality of the images seen by the CCD camera. Since in the first stage, where the image of the scintillator is focussed on the intensifier photocathode, a very fast optical lens is required, the depth of field (DOF) inside the scintillator, which is focussed sharp, is very small; in the PTB imaging system of the order of 1.0 - 2.0 mm. However, the thickness of an efficient scintillator for fast neutrons is of the order of 30.0 to 50.0 mm [18]. To overcome this DOF problem, a plastic fibre scintillator (FOS) can be used, which produces the optical image in a plane at the rear end of the FOS. The recoil proton produces scintillation inside the fibre and a part of this travels through the fibre itself. The diameter of each fibre relates to the resolution, with a small diameter offering better resolution. However, the minimum thickness of fibres is limited by cross-talk between individual fibres, because the recoil protons have certain ranges and can cross several fibres if they are too thin. Fibre scintillators can have an interaction efficiency of 70% [20]. Thus, the rest of the optical components

can be focused onto the surface of the scintillator. The PTB and Necsa systems use the fibre scintillator with dimensions of 20.0 × 20.0 × 7.0 cm^3 [11] and 19.0 × 19.0 × 7.0 cm^3 [20], respectively. The diameter of the fibres are 0.5×0.5 mm^2 and 0.5×0.5 mm^2 respectively. These are both coupled to a highly reflective surface to make use of any photons moving in the opposite direction, to further amplify the image.

2.2.3 Bending mirror

Neutrons and gamma-rays cause radiation damage to the electronic and electro-optical components in the optical path. The CCD sensor is very vulnerable to fast neutrons. To protect these components, they are moved out of the direct neutron path by a bending mirror placed at 45° to the optical path. This takes the scintillation image through the optical path for capture by the CCD camera. The mirror has a 99% reflectance, temperature stability and mechanical rigidity [14].

2.2.4 Lens

The amount of light emanating from the scintillator is not focused, therefore, a requirement of an optimal focusing of the image is needed to transfer as much usable light as possible onto an image intensifier. This being done by means of a focusing lens (single focus for the Necsa system [20] and a complex custom-made objective for the TRION system [14]). The Necsa system [20] has lens dimensions of 20.0 cm diameter aperture which condenses the image onto a 15.0 cm diameter image intensifier. The TRION system has a lens diameter of 12.60 cm which de-magnifies a 20.0 × 20.0 cm scintillator screen onto an image intensifier of 4.0 cm diameter [14].

2.2.5 Image intensifier

The image intensifier is composed of a phosphor screen, a photocathode (PC) and one of two Multi-Channel Plates (MCP), sealed inside a ceramic vacuum tube. A striking photon on the PC causes a photo electron, which induces an electron avalanche in the MCP of the order of up to 10^7 [21] (the photocathode is negatively biased causing electrons to accelerate toward the MCP which causes emission of secondary electrons and a successive electron avalanche inside an MCP channel). The electrons which are ejected from the MCP are accelerated in an electric field and hit the phosphor, where an electron to photon conversion is induced. For every photon striking the photocathode, the creation of several photons from the phosphor occurs. By that mechanism the weak optical image which is projected on the phosphor is amplified by potentially several orders in magnitude. Image intensifiers used in this study are manufactured by Photek and Photonis.

2.2.6 Second lens and image intensifier

The second Nikon (5.0 cm) lens focusses the light from the intensifier phosphor to the CCD chip of the Camera. In the case of TRION a 50.0 mm Sigma Macro lens of F2.8 is used.

2.2.7 CCD camera and acquisition system

The Necsa system uses a Princeton CCD camera with a 512 $\times$ 512 [22] pixel array system that is cooled to -30°C. The system is controlled by an ST-138 controller [23] and read out through a commercial readout card. The images are captured through the WinView software package [22] and analysed using Image J [24].

The PTB system uses an FLI camera [14] which has a 4k $\times$ 4k resolution, cooled to -25°C with a direct USB-B to USB readout and analysed using commercial FLI software and/or an in-house developed MATLAB code for acquisition and Image J for analysis.

2.3 Comparative fast neutron systems

2.3.1 FANGAS

The Fast Neutron Gas filled imaging System (FANGAS) was also developed at PTB with a 0.10 cm thick polyethylene radiator in which neutron induced recoil protons are produced. Polyethylene is chosen because of its high hydrogen content [25]. Recoil protons escape from the foil and ionize gas along the track. Electrons near the foil surface are amplified by the Parallel Plate Avalanche Chamber (PPAC) with a final amplification taking place in a Multi-Wire Proportional Chamber (MWPC). Position coding is done using a cathode delay line readout (a sensitive area of 314.0 cm^2) [26]. Data for the FANGAS is collected in list mode to achieve a rate of 8.0 $\times$ 10^4 s^{-1} counts with a low detection efficiency. Due to the low efficiency of the radiator the images obtained in Figure 2.6 [26] require long data collection times. Therefore this system was not used in the experiments for this thesis.

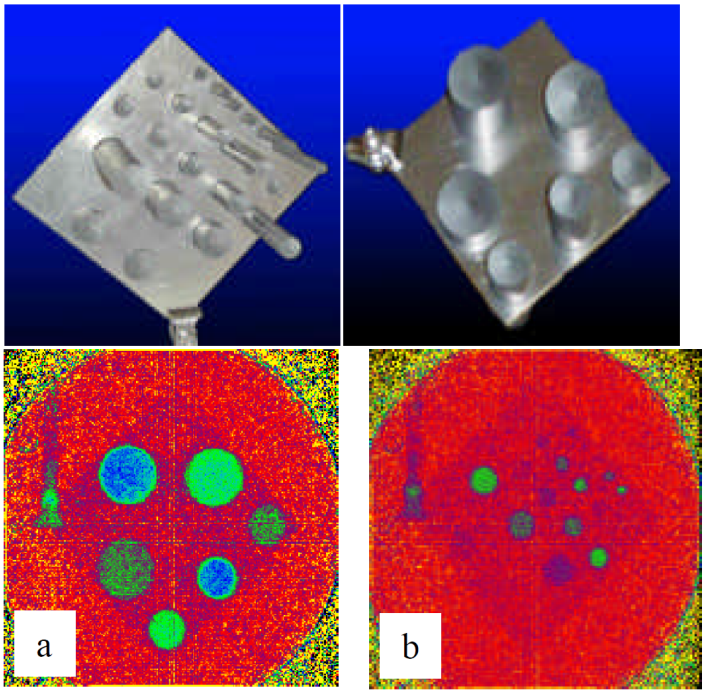

FIGURE 2.6: The sample, above, with the resulting FANGAS radiographs presented in (a) and (b), below

2.3.2 CSIRO

This is a dual fast neutron-gamma scanner commissioned at Brisbane airport for applications in security. It uses a 14.0 MeV D-T neutron generator as its neutron source and a ^{60}Co gamma source [27]. The fast neutrons in combination with the photons allow for a better discrimination of materials of different atomic number.. The attenuation of the two types of radiation in the sample is measured using separate neutron and gamma-ray detectors, optimized for the best efficiency and highest resolution for each kind of radiation. Source to detector distance is varied to accommodate for varying sample sizes. The detectors are placed in a modular configuration to allow for easy replacement and a high-speed custom software package is linked to process the data, producing images as shown in Figure 2.7 [28].

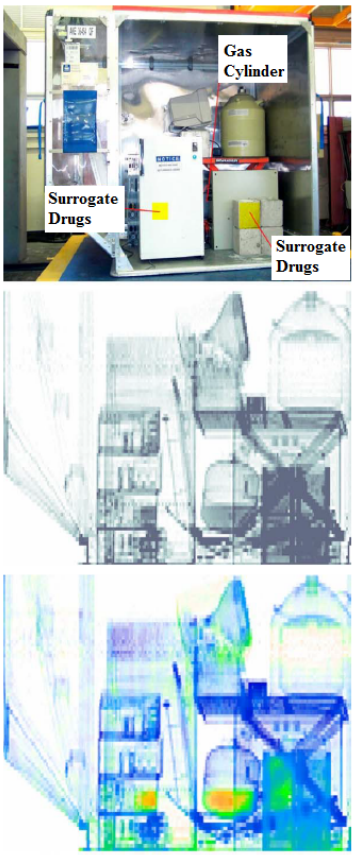

FIGURE 2.7: Image obtained using the CSIRO imaging system at Brisbane

2.3.3 PSI system

The PSI system uses a TS14 CCD camera focused onto a BC 400 plastic scintillator [29], which is transmitted by a bending mirror to the optical path. A focal length of f = 2.50 mm lens is used to focus the image onto the CCD for image capture. Tests were carried out at the 10.0 MW research reactor of the BNC, with a fast neutron flux of 2.70×10^7 n cm^{-2} s^{-1} (neutron energy greater than or equal to 2.50 MeV), used to create the images in Figure 2.8 [30].

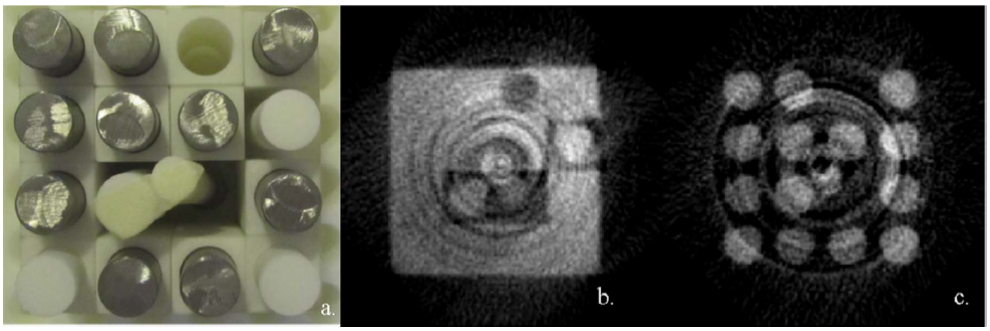

FIGURE 2.8: Image obtained from the PSI imaging system

2.4 Fast neutron sources

2.4.1 Accelerator based

The development of accelerators began as early as the 1930s. These were small machines of a few metres in size and have now evolved to the multi-kilometre sized machines of today.

Some of the earliest applications of accelerators were medically related which grew to the treatment of cancers, production of medical isotopes, food sterilization and aspects to provide energy to processed matter (electron beam welding and x-ray lithography). Other accelerators probe into the microscopic range of matter with a focus on the study of Nuclear and High Energy Physics [31].

One of the first uses of energetic charged particles was the Rutherford experiment [32]. In this, α particles emitted from radium and thorium were used to discover the positively charged nucleus. The next step was to use this natural moving α particles to excite nitrogen through the mechanism [33],

$$\alpha + N \rightarrow O + H \tag{2.2}$$

which was the first investigated nuclear reaction, showing Rutherford the advantage of using moving charged particles from nuclear reactions. This prompted a mindset in which the idea of charged particles moving at a high energy to overcome the Coulomb barrier would be ideal to study further nuclear reactions.

The technological limitations of the time deferred the exponential rise in development, but the advances in quantum mechanics, more especially the quantum tunnelling effect [34], showed that lower energies can be used to penetrate an atom potential well to split the light atoms. This made achieving acceleration of nuclear particles at lower energies possible.

The acceleration of microscopic particles such as electrons and protons, under the influence of an electromagnetic field has two aspects. One related to the longitudinal electromagnetic force (particles moving along the electric field) and the transverse bending due to the electric and magnetic fields. These are respectively represented by the motion of the charge under the Lorentz force by Equation (2.3) [35],

$$\overrightarrow{F} = q\left(\overrightarrow{E} + \overrightarrow{v} \times \overrightarrow{B}\right) \tag{2.3}$$

which governs the longitudinal motion along the electric field and for the transverse bending, the motion is described by the Stern Gerlach Equation (2.4) [35],

$$\overrightarrow{F} = \Delta \left(\overrightarrow{\mu} \overrightarrow{B} \right). \tag{2.4}$$

Particle accelerators can be divided into two categories i.e. linear accelerators that accelerate through a single pass and circular accelerators that re-circulate the beam through the accelerating voltages.

Linear accelerators include the Van der Graaff, the Cockcroft and Walton cascade generator, a Radio Frequency Quadrupole (RFQ) accelerator, etc. For circular accelerators, the cyclotron and synchrotron are most common for applications into nuclear science. A result of the unique nature of accelerators, being able to accelerate specific species for tailored experiments, the parameters of the accelerator and its deliverable output must be considered when deciding what one needs for the experiment, i.e. input power, type of particle and overall cost.

The simplest form of elementary acceleration is the potential drop accelerator [31], in which a source of ions is accelerated across a pair of electrodes through a potential drop of ΔV (voltage differential). This is achieved using devices like a cathode ray tube or electron microscope. It forms the theoretical basis for the electrostatic accelerator built by Van der Graaff and the cascade generator by JD Cockcroft and ETS Walton, the latter being the first to successfully achieve a nuclear reaction from an accelerator which was done at Cavendish Labs [36].

These cascade accelerators are high voltage units enclosed in tanks that make use of a multiplier rectifier-condenser system, in which two rectifying diodes and two capacitors applied to an accelerator system, give twice the voltage yield which is imparted to the particles as they move. It is designed for use up to 5.0 MV and produces a current output of around the 100s of mA [33]. It achieves this by using the pulsing DC current to charge a staged capacitor bank, with each stage adding to the total voltage experienced by the charged particle, this imparts energy to the accelerating beam.

The Van der Graaff (VdG) accelerator [37] is another electrostatic accelerator that uses a belt of insulating material that runs between ground and a high voltage (HV) generator. Charge is then imparted to the belt via a sharp corona discharge, which induces charge on the hot terminal. This charge is collected and allowed to flow to the electrode surface. It then creates a high electric potential on the spherical globe, with the electron stripped off at the lower corona points. The increase in the positive potential causes any internal gas to undergo ionization and due to the increased potential ($\overrightarrow{E}$) these ionized charges experience a large Lorentz electric force and therefore accelerate. An improvement to this design uses accelerated negative ions from the ground to the terminal, this is called a Tandem accelerator [33], which are then stripped of

their electrons via a thin foil. This causes the positive ions in the upper terminal to accelerate to ground, the principal energy gain is twice that of a normal VdG.

The VdG at Necsa is a 4.0 MV VdG accelerator [38][39], with an ion source capable of producing accelerating species of H^+, D^+, Cu^+, N_2^+ and O_2^+ with beam energies of up to 3.60 MeV and a beam current of 200.0 μA. This beam, when passing through a bending magnet, drops to a current of approximately 10% of the nominal value. The fast neutron flux achievable is at most 10^6 n s^{-1} cm^{-2}, using a deuterium target.

As the energy requirement increased it became necessary to look at producing acceleration beyond a few MeV. Another method makes use of the resonance acceleration using a Radio Frequency (RF) field. Here the particle must pass through a small potential gap in resonance with an oscillating electric field, producing a larger energy gain. This can be done in series with many gaps causing linear acceleration, or with a single gap circular device.

In the linear case, several drift tubes are connected to a high frequency oscillator, Figure 2.9 [33]. Charged particles from the ion source are accelerated between the gaps of the tube. Whilst the particle is in the tube, the direction of the field is reversed, this causes the particle exiting the tube to see an accelerating electric field which induces further acceleration. As the particle speed increases, the drift tube length must increase to accommodate the longer distance travelled, for the same time [40]. This also ensures that the particle will reach the next gap with the correct phase. Due to the design, frequency and voltages needed for acceleration, only particles matching these will be accelerated. RF technology has allowed major gains in the development of these accelerators, with Linacs going up to 40.0 GeV (electron accelerators) and 800.0 MeV (protons). Another structure consists of resonator tubes that make use of a standing wave structure created by each tube having a potential distribution, this causes acceleration of each species through the tube. As these particles become more relativistic, one needs a high frequency source to modulate their speeds.

For low energy high current machines, the RFQ accelerator is used. It comprises an inner core of an electrostatic quadrupole which alternates the charge between the perpendicular poles, Figure 2.10 [33], thus giving the beam electric focusing, bunching and acceleration. The field produced by the RFQ is continuous with its bunching effect close to 100% [31] and focusing resulting from the transverse electric gradient.

The electric charge on the vanes oscillates, you get focusing of the beam on one plane and defocusing on the other which is continually switched and results in a net focusing effect on the beam [40]. Each vane has the etchings of a sinusoidal wave, the wavelength increasing as you move away from the ion source. This increasing wavelength is an accommodation for the beam travelling faster along the induced

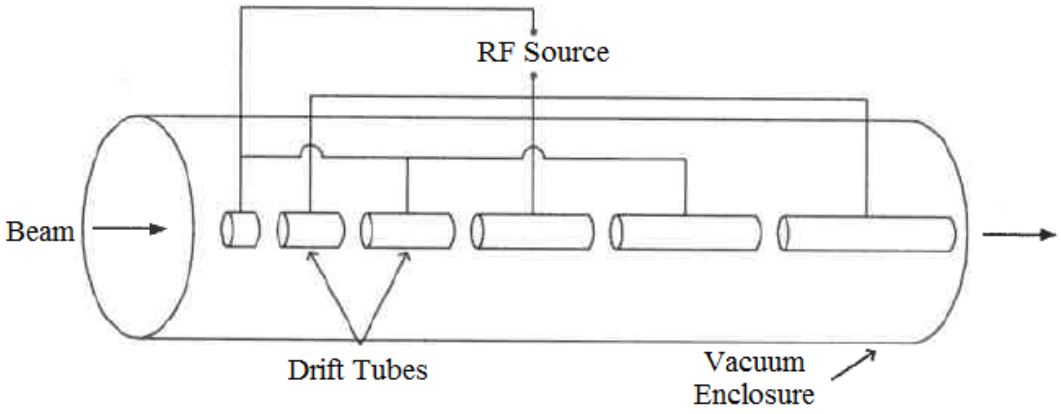

FIGURE 2.9: Conceptual design for a linear accelerating system

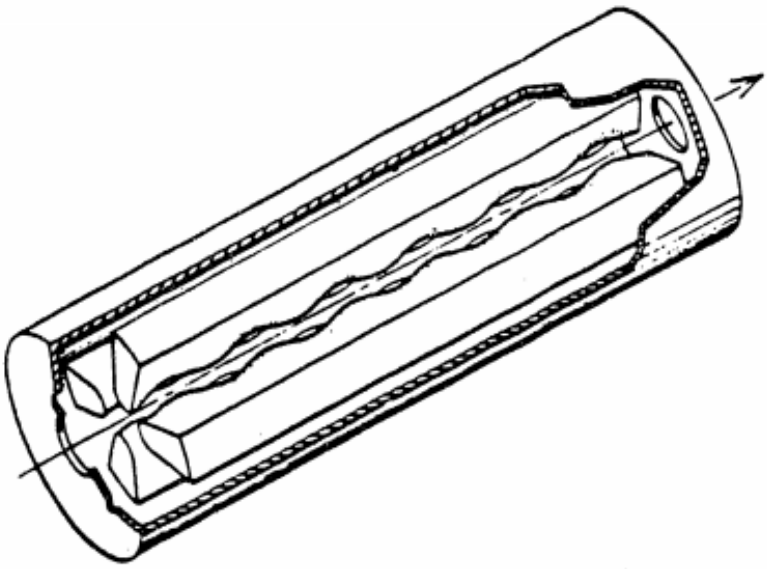

FIGURE 2.10: Representation of the RFQ rods showing the modulation that induces the acceleration field

longitudinal electric field; this is the accelerating field.

The RFQ accelerator at Necsa is a four vane core with a multi-cusp ion source, High Energy Beam Transport (HEBT) system and a target station. The system operates at an ideal vacuum of 10^{-7} mbar. The ion source produces both H^+ and D^+ ions, which due to the RFQ's operating frequency of 200.0 MHz, are accelerated from a potential of 35.0 keV, through the 4.0 m long RFQ cavity, up to a beam energy of 4.0 MeV for D^+ (2.0 MeV for H^+). The RFQ runs at a duty cycle of 1.2% and is able to focus a beam onto a target with a beam current of 1.0 mA (peak) and an associated beam spot of 2.60 mm. This causes a nuclear reaction within the incident target that produces a fast neutron energy spread of 1.0 to 10.0 MeV with a flux at the target of 10^7 n s^{-1} cm^{-2} [1].

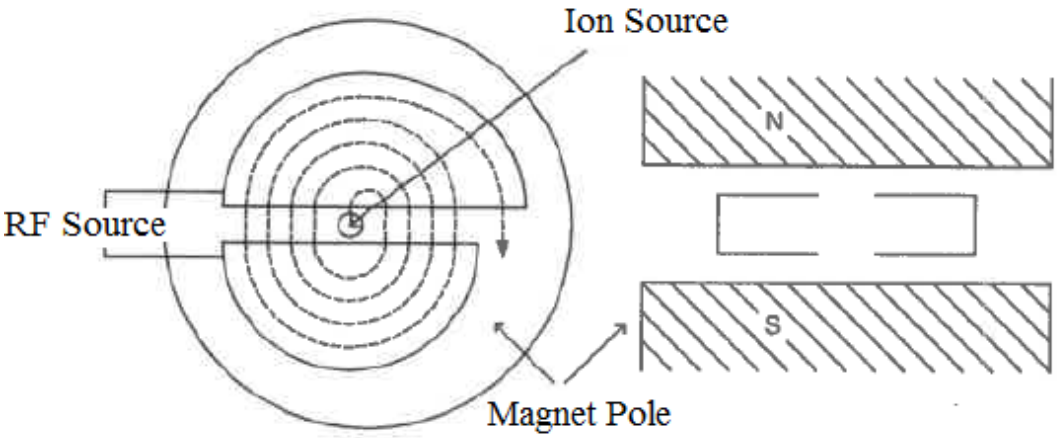

FIGURE 2.11: Concept representation for the operation of a cyclotron accelerator

In 1938 Ernest Lawrence realized that you can accelerate the ions and return them to the same point. This can be repeated and multiple accelerations will occur [41]. From this, his design uses a homogeneous magnetic field so the particle will be bent back twice to the original RF gap in the RF field and at each time it will experience an acceleration, which is the principal of the cyclotron shown in Figure 2.11 [33].

This is the first example of circular acceleration with a homogeneous electric field bending the particles back to the original RF gap between the two *D*-shaped electrodes as shown in Figure 2.11, twice in each period. If the RF is set to the resonant frequency, the particles will continue to pass near the peak RF voltage twice per turn, gaining kinetic energy and growing their orbital radius until reaching some extraction point to move toward a target. To adjust for relativistic speeds, only particles in phase with a varying RF will be accelerated [41]. In this case, only one bunch of particles will reach the energy due to the limitation of the magnetic field and RF modulation (synchrotron principal). Only a few cycles are needed to get to full acceleration.

The two *D*-shapes are connected to a RF source so the alternating voltage appears across the gap, with an ion source placed in the centre. The ion source produces ions at a low initial velocity and with the present magnetic field, the ions move in a circular motion described by Equation (2.5) [33],

$$R = \frac{m\vec{v}}{q\vec{B}} \tag{2.5}$$

where R is the radius of the orbit, m and q the ion mass and charge respectively, $\vec{B}$ the magnetic field experienced and $\vec{v}$ the velocity. The ion, due to its circular motion, has a period and therefore a frequency. The energy of the beam achievable and its current is therefore hard-set into the design of the cyclotron, size of the magnets and the ion source. The ion moves along an increasing orbit as the velocity increases. The field

lines near the edge acts to stop the beam from diverging but this is the region where resonance is lost, so this is where it is beneficial to extract the beam. The cyclotron produces high current beams with the periodicity of the design making for a pulsed beam, with an energy resolution that is not as sharp as that of an electrostatic accelerator [31].

The PTB isochronous cyclotron CV28 [42] is an energy variable cyclotron with a magnetic field flux density of less than 1.40 T and a RF system that operates at 26.0 MHz and 35.0 kV. The system is capable of accelerating protons (2.0 to 24.0 MeV) and deuterons (4.0 to 14.0 MeV) to a beam current of 100 μA. For a ^{9}Be target and a beam energy of 6.60 MeV, the cyclotron can produce neutrons of up to 10^{8} n s^{-1} cm^{-2}.

The synchrotron was invented to adjust for the loss of resonance, this modulates the RF field to keep in step with the frequency [43]. The RF field decreases with an increased ion energy (acceleration for changing mass). The RF is swept from its maximum to minimum and this accelerates the beam around a set loop, here however the current value is lower than the cyclotron but the beam energies are higher. Another method is to have a varying magnetic field with a varying radius, this magnetic field focuses and forces the ion to travel along stable orbits with the poles creating high and low field sectors [44]. This acceleration does not only take one bunch at a time but many pulses; this yields a large beam current (order of 100.0 μA) operating at a fixed frequency.

Synchrotron accelerators use a ring of bending magnets, as indicated in Figure 2.12 [33], to push an ion in a circle around an acceleration ring. This type of acceleration requires the ions to be injected in at a higher energy, then takes the ion species higher up as it moves along the field. For electrons, input is at relativistic speeds (this being achieved by using an electrostatic accelerator as an injector). For protons and heavy ions, this is difficult to achieve pre-synchrotron. Therefore, as close to relativistic as possible, energies are used as an input to the synchrotron with the RF and magnetic fields varied to keep the ion's orbital radius constant. The synchrotron is capable of producing beam energies of up to the hundreds of GeV (even TeV) [33].

The Large Hadron Collider (LHC) is one of the largest global physics endeavours where the synchrotron accelerator can produce a beam of up to 13.0 TeV when the ion travels through a beam circumference of 26.70 km [45]. The LHC was the facility used in the discovery of the Higgs Boson [46].

For materials studies, accelerators are used to move particles to extremely high speeds and cause them to react with target material and to act as a source of fast neutrons via the nuclear reactions. The specific reactions used at accelerator facilities to produce fast neutrons are described in Section 2.5 to follow. The advantage of an accelerator based fast neutron source is the possibility to tailor the properties of the fast

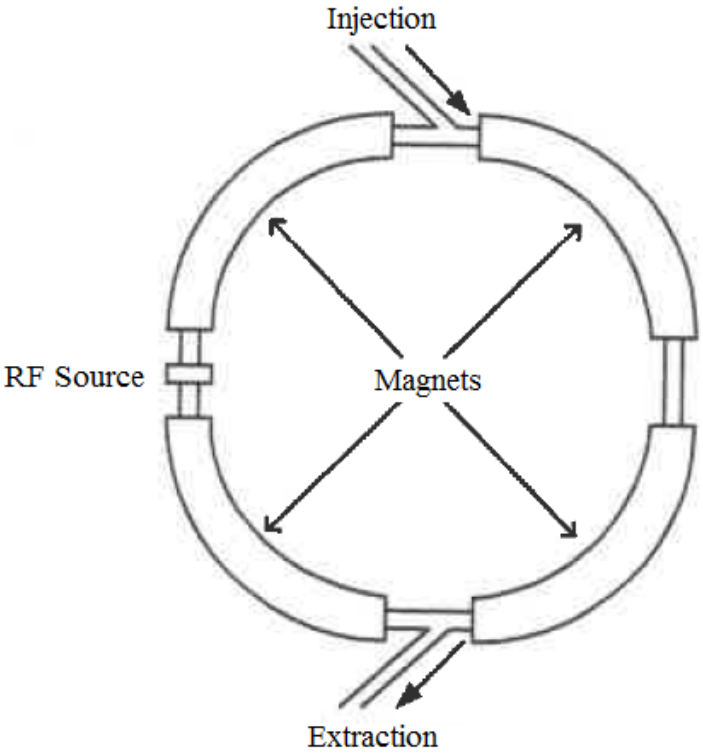

FIGURE 2.12: Concept representation for the operation of a synchrotron accelerator

neutron beam by choosing the most suitable nuclear reaction (ion and target combination), target thickness, ion beam energy, intensity and the time structure of the ion beam, in a way that the resulting neutron beam properties optimally suit the application.

The experiments and investigations carried out during this study where conducted at the PTB cyclotron and Necsa RFQ.

2.4.2 Reactor based

Nuclear reactors are a source of sustained energy supply and serve the purpose of fulfilling nuclear based research. One of the oldest and most powerful sources of fast neutrons are nuclear research reactors. One type of fission reactor makes use of the induced fission of enriched uranium (^{235}U) to chromium (^{92}Kr) and barium (^{141}Ba) after the collision with an appropriately energised neutron [47][48]. The process becomes self-sustaining by appropriate moderation and thermalisation of the neutrons so that they can induce further fission events in a constant and self-sustaining manner, controlled by control rods of neutron absorbers and the core temperature. The same mechanism can be obtained with mixed ^{239}Pu based fuel elements (instead of

^{235}U). The neutrons produced form part of a cascading process where each interaction produces several further neutrons and cause a nuclear chain reaction that can become unstable and dangerous. For this reason, the reaction has to be controlled, which requires the use of moderators to absorb the extra neutrons produced in the core. The ideal case is a one to one conversion of neutron to neutron with the moderator absorbing the extra produced neutrons.

The average neutron energy produced in a fission reactor is about 2.0 MeV. This chain reaction, for neutrons, has a low probability of interaction but this is overcome by the rate and abundance of fast neutrons present during the process. Reactors are named in accordance with the average energy of the neutrons that are responsible for the nuclear chain reaction in the core. Most of the reactors worldwide use thermal neutrons to sustain the chain reaction. Due to this, the dominant applications at reactors are linked to thermal and slow neutron applications, whereas fast neutron applications aren't as common.

All neutrons born in nuclear reactors are fast [49] and as a result of their cross-section of interaction with hydrocarbons and water, these materials are used as moderators to thermalize the neutrons. This increases the thermal neutron to uranium interaction and by implication the yield. The spectrum in Figure 2.13 [50] shows a comparison between the thermal and fast neutron spectra for reactors. One has to also consider safety and design as these are of the utmost importance when creating a neutron beam line at a reactor. Due to these limitations, accelerator based fast neutron sources offer the best option, taking into account the flux, space, safety, signal to noise ratio and ease of sample handling.

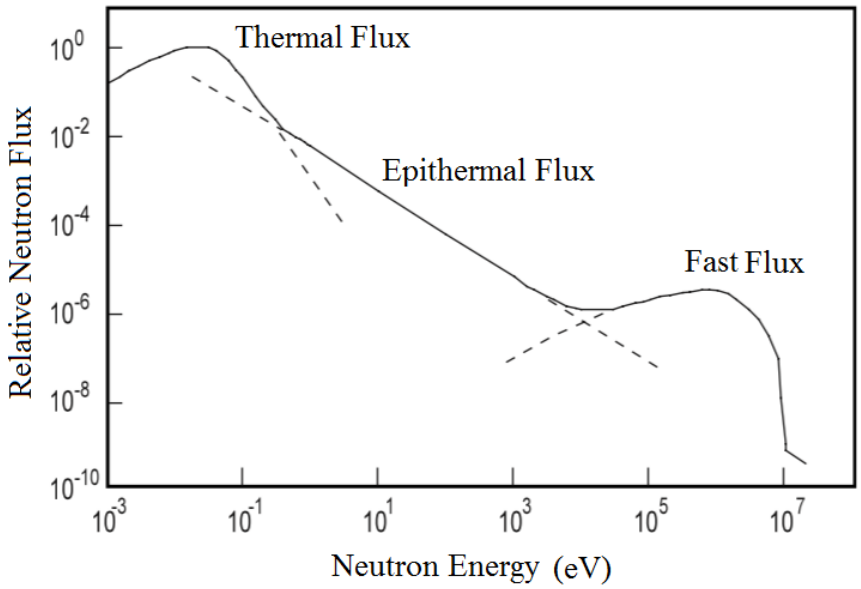

FIGURE 2.13: A typical neutron energy spectrum from a nuclear fission reactor

2.4.3 Neutron generators

Neutron generators are compact devices that use the deuterium on deuterium (*D-D*) or deuterium on tritium (*D-T*) reactions to produce fast neutrons, which can be used in a number of applications. Neutron generators make a small demand on input power, and due to their small size, make this type of neutron source ideal as a mobile source [51]. The drawback is that the yield from these is in 4π, with a slight bias in the forward direction. When looking at the solid angle, the average flux is lower than that achieved when using a linac and this increases the time required to conduct an experiment.

Neutron generators work on the principal of nuclear fusion of the isotopes of hydrogen. Deuterium or tritium (or a combination thereof) are excited and accelerated onto a hydride target of deuterium or tritium, to produce these fast neutrons. The reactions are shown below, [52] [53],

$$\begin{aligned} D + D &= {}^{3}He + n(2.50\ \text{MeV}) \\ D + T &= {}^{4}He + n(14.10\ \text{MeV}) \end{aligned}$$

with the *D-T* reaction having the greater yield which makes it a more common source. Generators produce a higher flux when compared to point sources but are lower than Linacs.

These neutron generators can be bought as a sealed tube [51], that houses an ion source, ion optical elements for beam focusing and a beam target. The entire system

operates completely as one sealed unit, with power supplies being the only external element. Being a complete system, the ion source has to function as efficiently as possible with the maximum ions produced using the least gas and power input, whilst accommodating for the pressure difference between the ion source and the accelerator tube. When the atomic ions exit the ion source extraction, they are accelerated in an electric field to 50 keV up to few 100 keV before they hit the target.

The accelerated ions pass through a negatively biased accelerator electrode and strikes the target. Targets are made up of metal hydrides, be it titanium or zirconium, on a metal backing, which is then dosed with hydrogen atoms. The temperature experienced by the target and the overall neutron yield requirement, play an important role in the target's design [52].

Compact neutron generators are becoming popular in fields of medicine, neutron science and security, this is a result of their mobility and yield 10^8 to 10^{10} n s^{-1} at 14.10 MeV, in 4π. The most beneficial ion source due to its high atomic yield is the RF-Induction discharge ion source. Ions are accelerated toward a titanium target with the deuterons depositing onto the target, causing it to become a deuterated target.

The PSI neutron generator has a target current of 0.15 to 0.50 mA and a neutron yield to beam power, with a spot size of 2.0 mm, shown in Figure 2.14 [54], which gives a neutron output range for the desired experiment.

Figure 2.14 shows the relatively low flux obtained in 4π. This source is limited in producing a larger signal to noise ratio for good quality radiography.

2.4.4 Spallation

During the spallation process, parts of the target are ejected due to impact or stress. This is best described when looking at a heavy nucleus emitting a large number of nucleons after being impacted by a high energy particle [55].

In spallation sources for neutrons, protons are initially accelerated to high energies (using either linacs or synchrotrons) making them incident onto a solid metal target [55]. The incident proton beam excites the heavy nucleus to very high energies and causes it to fragment in many lighter isotopes and a large number of high energy neutrons. The advantage of these sources is that they can be pulsed. Suitable targets for spallation sources are made of high Z elements. Since they have to cooled, liquid targets from Hg and Bi-Eutecticum are used, but also Tungsten is suitable due to its high melting point.

In the spallation process you obtain a lower heat release per neutron and the pulsing of the source gives a time structure, which is a benefit over reactors [48]. The

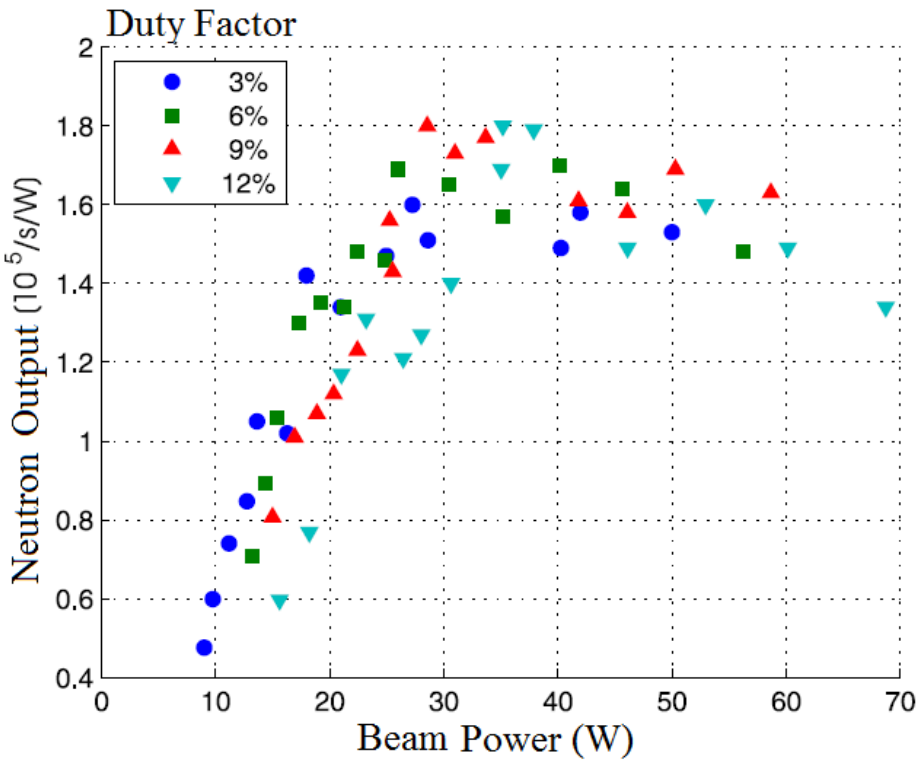

FIGURE 2.14: Time-averaged neutron yield per unit beam power at the PSI neutron generator

process is not exothermic and the yield is also proportional to the target mass. When compared to the neutron flux from those of fission we see in Figure 2.15 [55], a much higher and usable yield in the fast neutron energy regime. For a proton energy of E_p = 800.0 MeV on a non fissile target one obtains a flux of 2.0 $\times$ 10^{16} n s^{-1} [47] .

The international trend is to move away from building reactors and focus on the construction of spallation sources. This is evident by the operational sources, the Spallation Neutron Source in Oak Ridge [56], the Japan Spallation Neutron Source [57] and the Chinese Spallation Neutron Source [58]. The European Spallation Source (ESS) [59] is currently under construction with a targeted completion date in 2025.

2.5 Reactions

The primary reactions used in accelerators to produce fast, free neutrons are mentioned here. Details are given on reactions that are used to produce the fast neutrons in this thesis study, with a few others presented to show the range of possibilities. It is

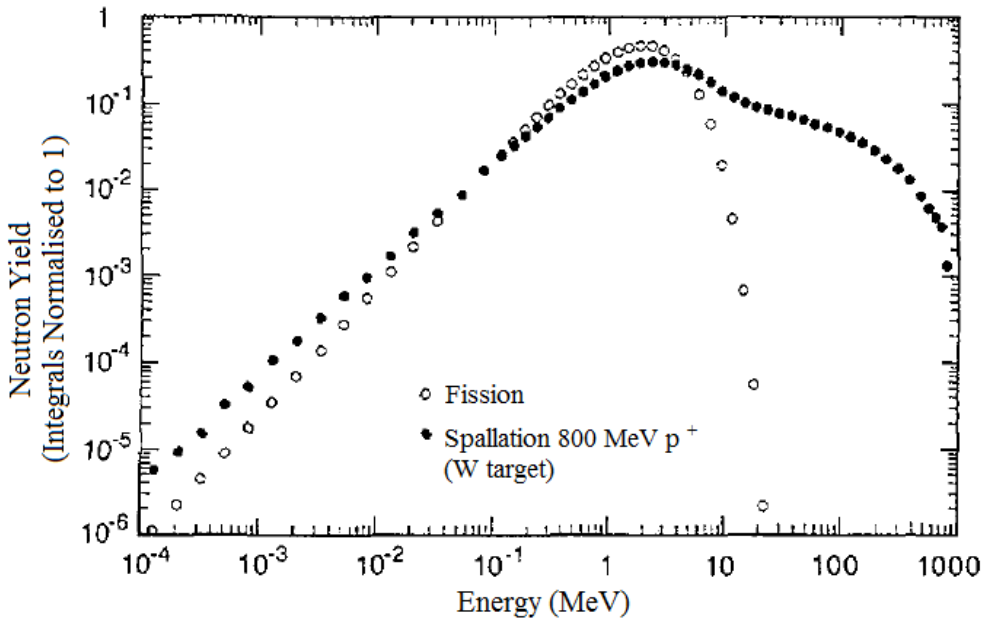

FIGURE 2.15: Calculated neutron spectra for fission and spallation using a tungsten target

the total neutron yield using different targets that makes use of tailored targets, to suit the needs of specific experiments. Figure 2.16 [60] shows the total yield for different reactions.

2.5.1 D(d,n)^{3}He

The D(d,n)^{3}He reaction decays as [61],

$$D + d \rightarrow {}^3He + n \tag{2.6}$$

where a deuterium atom is excited by a deuteron beam and produces neutrons from the fusion reaction. This reaction is known for its large cross-section of interaction and the fast neutrons that move in the forward direction and its positive Q-value of 3.27 MeV [62].

This reaction also allows one to choose an optimal neutron energy as the deuterium on deuterium reaction (*D-D*) yields a discrete energy neutron signal. The target thickness is also important and relates directly to yield [60], with the requirement that the target be as thin as possible, for a maximum yield. If the target is too thick the beam will be absorbed into it.

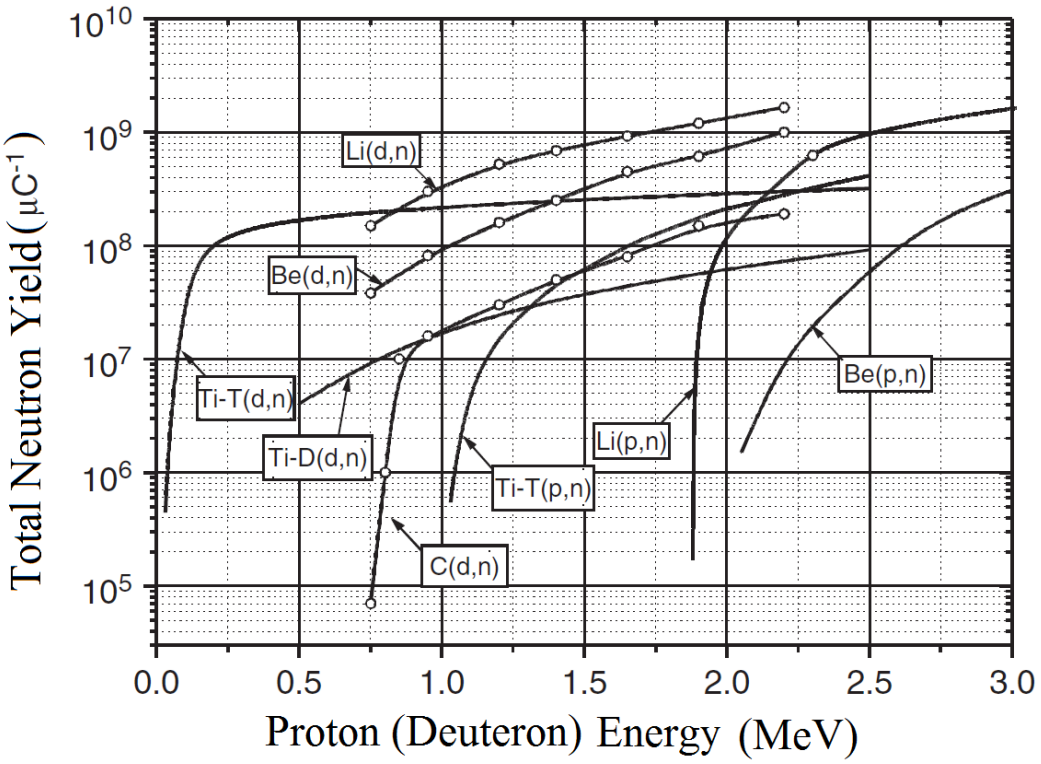

FIGURE 2.16: Total neutron yield obtained when using a thick target

A gas cell of deuterium is also used as a quasi mono-energetic neutron source in the 2.0 to 8.0 MeV intervals. Deuterium is preferred over tritium, as tritium gas is poisonous. The neutron yield in the forward direction, is dependent on the gas pressure and the incumbent deuteron energy. For a 6.67 MeV deuteron beam, the relative flux density is shown, for varying gas pressure and neutron energies as in Figure 2.17 [60].

Figure 2.17 shows the almost mono-energetic neutron peak with a maximum yield proportional to the deuteron energy in the forward direction. As the deuteron energy varies, so does the yield, demonstrating the energy selective nature of this reaction.

The Necsa RFQ accelerator had a windowless gas target that operates at 3.0 Bar pressure, this 4.0 to 5.0 MeV deuteron accelerator then produces 7.0 to 8.0 MeV fast neutrons in the forward direction [1].

Due to the exothermic nature of the *D-D* reaction, the neutron energy, E_n, and deuteron energy, E_d, relation is given by Equation (2.7) [62],

$$E_n = \frac{E_d}{8}\left[\sqrt{\cos^2\theta + 2 + \frac{6Q}{E_d}} + \cos\theta\right]^2 \tag{2.7}$$

to which we apply a Taylor approximation for the $\sqrt{x}$. Also, noting that in the forward direction $\theta = 0$ and the Q-value is Q = 3.30 MeV [62], Equation (2.7) simplifies to,

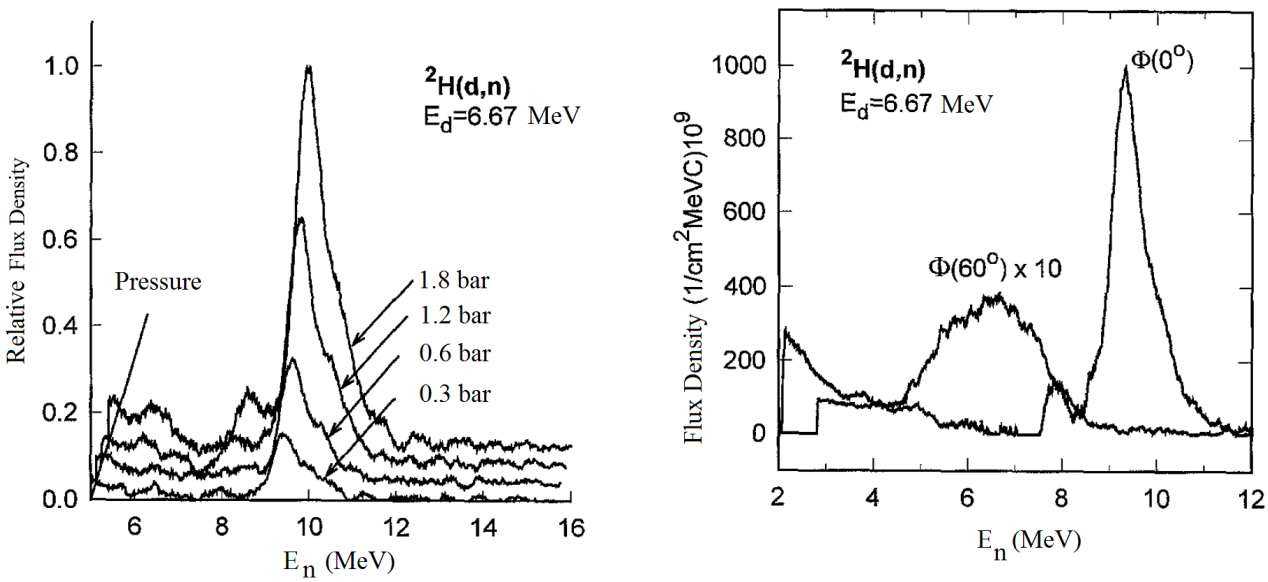

FIGURE 2.17: Spectral yield of *D-D* neutrons versus deuterium gas cell pressure and Neutron Spectrum from the *D(d,n)* reaction measured at various angles

$$
\begin{aligned}
E_n &= \frac{E_d}{8}\left[\sqrt{3+\frac{6Q}{E_d}}+1\right]^2 \\
\frac{E_d^2}{16}\left(3+\frac{6Q}{E_d}+1\right) &= \frac{E_d}{8}\left[3+\frac{6Q}{E_d}+2\sqrt{3+\frac{6Q}{E_d}}+1\right] \\
&= \frac{1}{2}E_d+\frac{3}{4}Q+\frac{\sqrt{3}}{4}E_d\left(1+\frac{Q}{E_d}\right) \\
E_n &= \left(\frac{1}{2}+\frac{\sqrt{3}}{4}\right)E_d+\frac{3\sqrt{3}}{4}Q \\
&= 0.93E_d+1.18Q \\
E_n &\approx E_d+3\text{MeV}. \qquad (2.8)
\end{aligned}
$$

From this a plot of the relation between E_n and E_d, is shown in Figure 2.18, for the gas cell target.

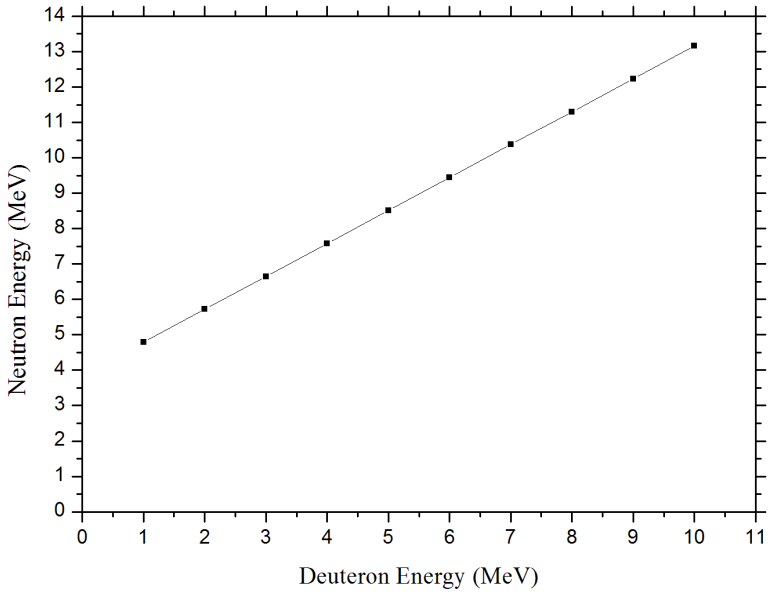

FIGURE 2.18: Relation of neutron energy to deuteron energy for the *D-D* reaction

2.5.2 ^{9}Be(d,n)^{10}B

Using such a target with a thick target layer, they produce a high neutron flux over a wide range of neutron energies.

Knowledge of the spectrum from the thick target at different D^{+} energies is important. The ^{9}Be target must be kept under a good vacuum to preserve the target for the experiment, with the holders made of a cooled conductive metal, like copper.

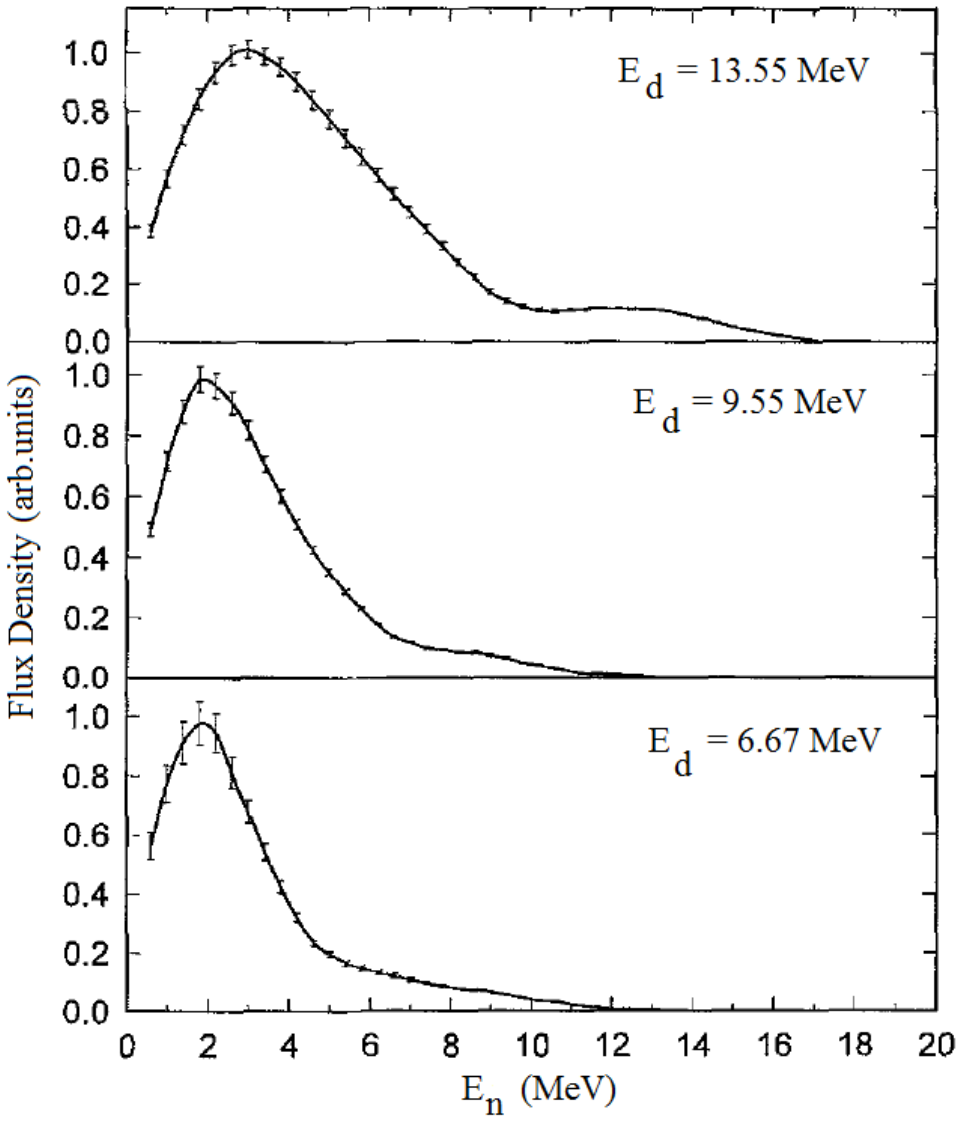

FIGURE 2.19: Multiple foil activation unfolding of neutron spectra from a thick Be target

The neutrons produced using a ^{9}Be target have a wider energy spread when compared to *D(d,n)*, with the average neutron energy produced by deuterons of energies of E_d = 6.67, 9.55 and 13.55 MeV incident onto a ^{9}Be target as shown in Figure 2.19 [63] with a peak intensity measured in the forward direction.

The ^{9}Be target has suitable thermal and metallic properties and little residual radioactivity in the fast neutron range. These ^{9}Be targets (5.0 to 7.0 μm) produce an output neutron energy range that is evident in Figure 2.20 [64].

Metal targets, like these that are chemically stable, can be machined into required shapes, have better thermal conductivity and therefore manage a higher beam current and last longer during an experiment.

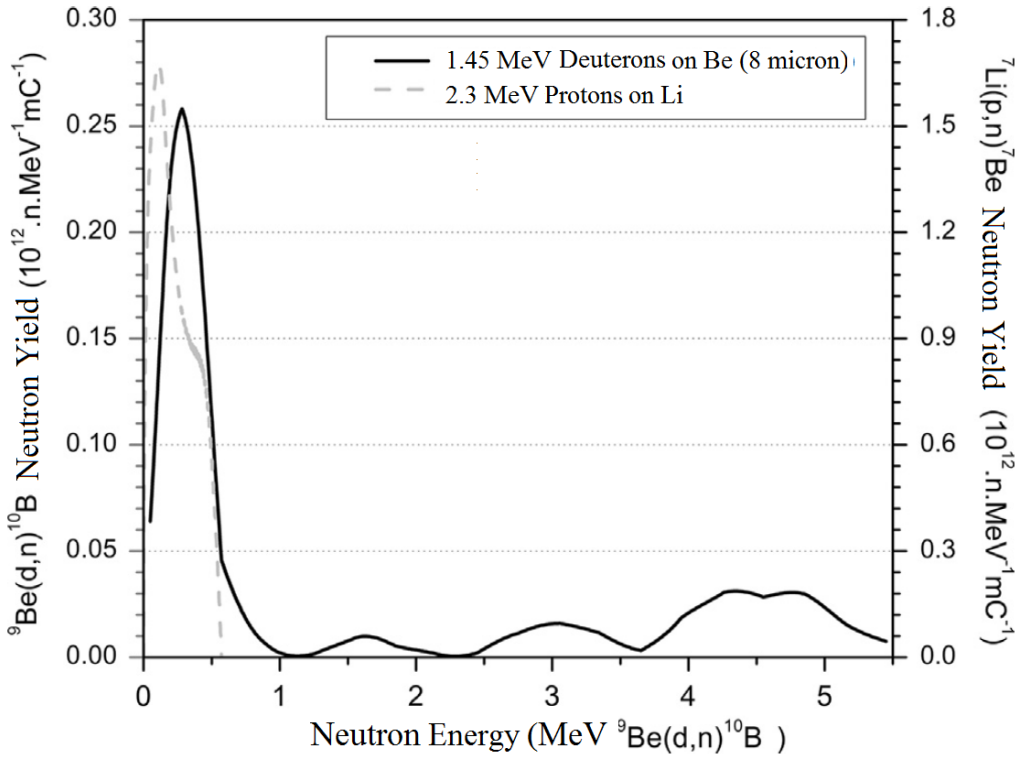

FIGURE 2.20: Neutron spectra produced by 1.45 MeV deuterons on a 8.0 μm thick beryllium target and by 2.30 MeV protons on lithium

When E_d is lower, a Q-value of 4.36 MeV [64] is required for the ^{9}Be(d,n)^{10}B reaction with the E_n spectrum being continuous for the four excited states of ^{10}B. When E_d is higher, many body reactions will occur. This will increase the neutron yield and add to the spectrum.

The stopping power of ^{9}Be for given deuteron energies, E_d, is shown in Figure 2.21 [61], with a higher E_d passing through thicker targets. For thick ^{9}Be at E_d of 7.0 to 13.50 MeV the E_n yield along the direction of propagation versus the E_n and θ, is shown in Figure 2.22 [61].

This highlights the ^{9}Be target as a preferred choice for producing a wide neutron energy range with the peak at 5.0 MeV (E_d=7.0 MeV) but widening for higher deuteron energies. The neutron yield from the ^{9}Be target is approximately 1.50 times greater [60] than that achieved using the ^{7}Li(p,n)^{7}Be reaction.

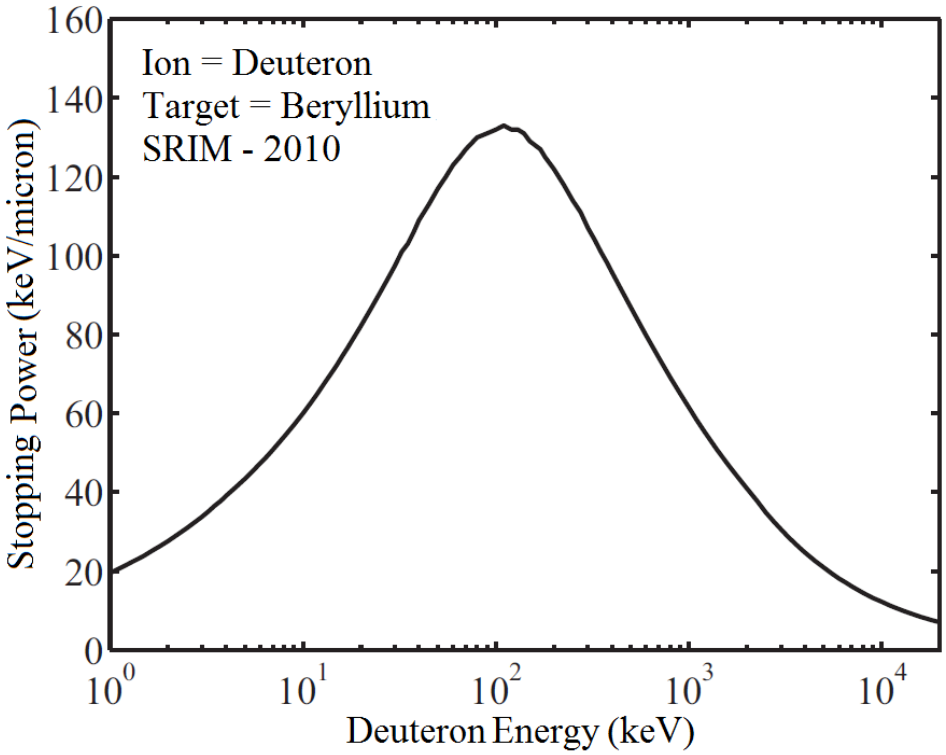

FIGURE 2.21: The stopping power of the ^{9}Be target to deuterons

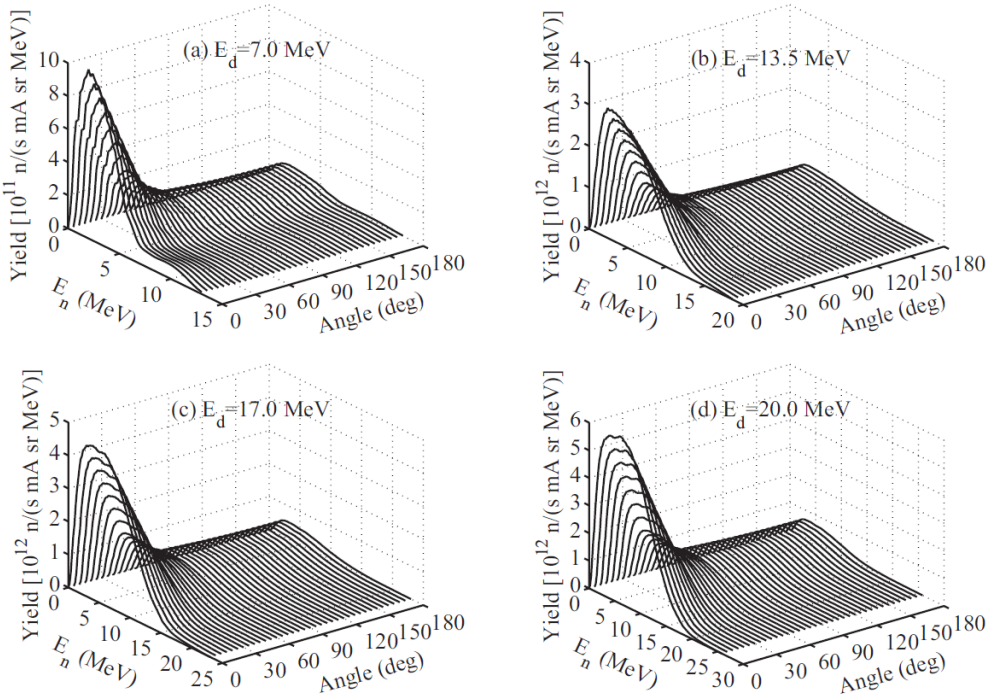

FIGURE 2.22: Neutron energy spectra of the ^{9}Be neutron source with the thick beryllium target at different incident deuteron energies

2.5.3 ^{7}Li(d,n)2^{4}He

This reaction makes it possible to create fast neutrons of up to 18.0 MeV with the E_d = 1.0 to 2.0 MeV, Figure 2.23 [60].

For thick ^{7}Li targets, this reaction also produces a ^{7}Li(d,p) ^{8}Li reaction that yields high energy electrons, making neutron-electron irradiation possible, the electron, however, will be better filtered out.

Lithium targets require care in handling as lithium melts at low temperatures and therefore must be transported in oil and placed immediately in the target station, with cooling. Chemical properties also present a difficulty as lithium oxidises rapidly, with an oxygen layer developing on the surface quickly. Carbon can also easily deposit on the target from diffusion pumps, which are used to create the target vacuum, which compromises the target integrity and therefore the neutron signal [65]. Furthermore, it reacts with water vapour, which is abundant even in vacuum systems.

E_n is measured using the time of flight technique, which requires a pulsed beam of neutrons for the neutron energy resolution. Since the distance to the detector is known and the time for the signal to reach the detector is known, the energy of the neutrons can be calculated. If the repetition rate is too fast, the low energy parts of the signal will mix with the higher energy of the incumbent signal and resolution will be lost, but this can be adjusted for from the pulse height spectrum [65].

2.5.4 ^{7}Li(p,n)^{7}Be

For a maximum yield from this reaction, the forward direction is favoured to overcome the angular anisotropy and beam softening as shown in Figure 2.24 [60]. The gamma-rays produced through this reaction should be moderated using natural lithium. This

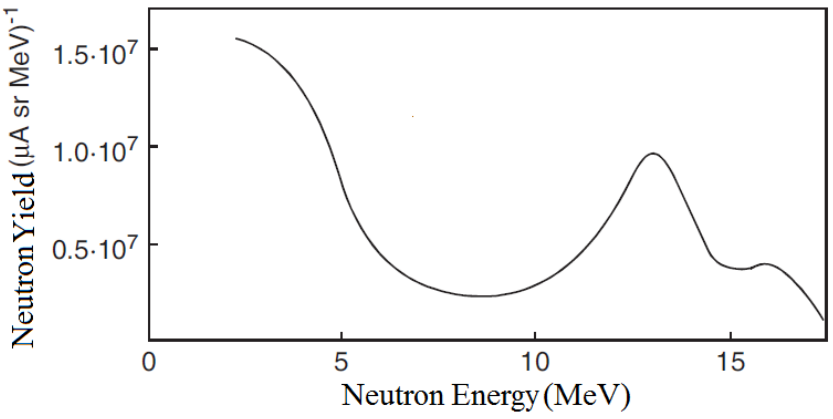

FIGURE 2.23: Neutron yield from ^{7}Li(d,n) reaction at 0° for a thick metallic ^{7}Li target for E_d = 2.0 MeV

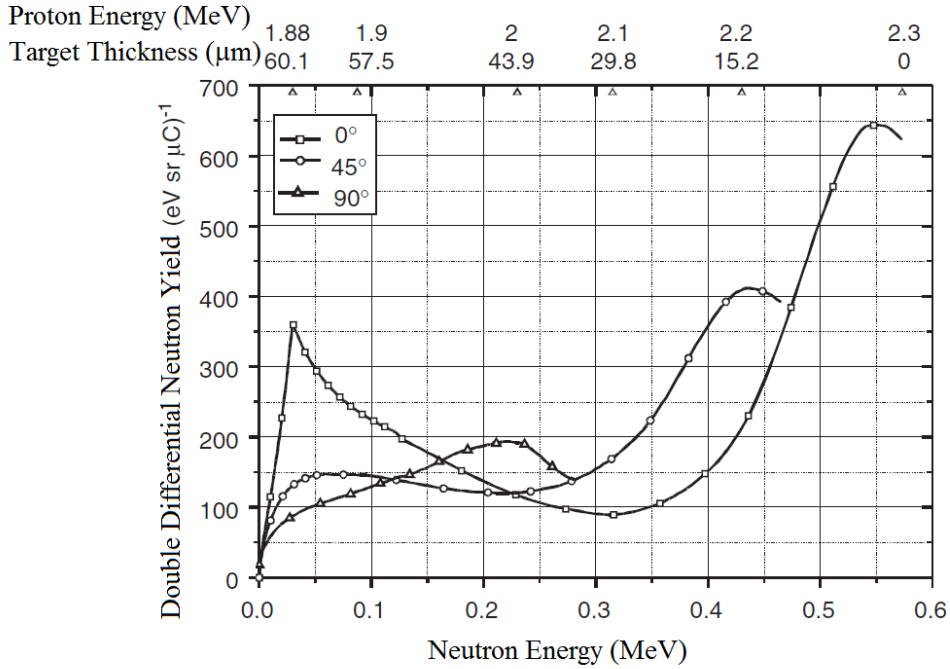

FIGURE 2.24: Double differential neutrons yield from ^{7}Li(p,n) reaction for angle 0°, 45° and 90° for thick metallic ^{7}Li target, initial proton energy 2.30 MeV

reaction is an endothermic one with a Q-value of less than zero. The production of ^{7}Be is used to determine the neutron yield through its prompt gamma-ray emission, as the ^{7}Be has a half-life of 53 days [65].

From these nuclear reactions, tailored targets can be used for a fast neutron spectrum for specific experiments. There are many such reactions to consider, but for a maximum yield to minimal E_d the ^{9}Be target has the most optimal results and is the easiest to operate, due to its good thermal conductivity, robustness, and low residual radioactivity. The deuterium gas target is difficult to maintain and costly to operate as this is a turbulent gas flow system. It does, however, offer the best neutron energy resolution. These are considered and used for the investigations conducted during this thesis.

Chapter 3

The Fast Neutron Imaging System at Necsa

3.1 Introduction

The Pelindaba Laboratory for Accelerator-Based Science (P-LABS), worked on developing a facility capable of producing a flux of neutrons for fast neutron radiography applications. Necsa has a Radio Frequency Quadrupole (RFQ) accelerator, the D-100. The team embarked on upgrades and development of the accelerator system in order to optimize neutron spectrum and neutron flux for its applications.

The RFQ was initially developed for the purpose of performing a non destructive examination of raw mineral elements. The RFQ was specified to provide a neutron yield of 10^{12} n s^{-1} at a beam current of 50.0 mA. The main usage of the fast neutrons was that as a probing tool for use in the technique of Fast Neutron Radiography (FNR). FNR uses the resonance features of the carbon cross-section in the neutron energy region, around 8.0 MeV, for the detection of carbon in minerals. An in-depth look into the features of the RFQ accelerator are examined here.

3.2 The Radio Frequency Quadrupole (RFQ) accelerator

The RFQ facility at Necsa contains a multi-cusp radio frequency ion source, that injects 35.0 keV deuterons directly into a four-rod 4.0 MeV RFQ accelerator cavity, specified to work at a 20% duty cycle. A proposed additional 1.0 MeV is possible via a spiral loaded three gap booster cavity. By tuning the RF phase between cavities, the beam travelling through the booster can be accelerated or decelerated, thus achieving a deuteron beam energy between 3.0 and 5.0 MeV [20]. This beam is incident onto a windowless spinning-disk, deuterium gas target that operated at 3 bar pressure. The original configuration of the system is shown in Figure 3.1.

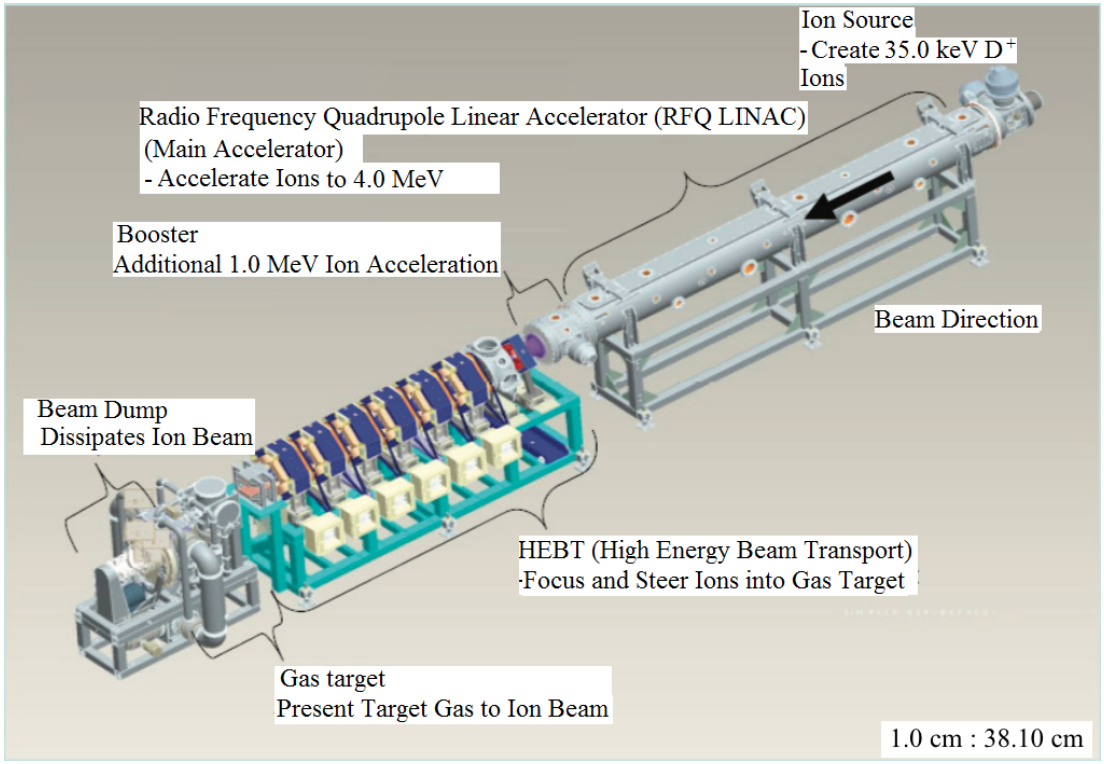

FIGURE 3.1: Layout of the original 4.0 to 5.0 MeV D^+ RFQ system at Necsa

The operating conditions specified and achieved are shown in Table 3.1 [1]. The lower deuteron beam current and energy is a result of a limitation within the RF ion source power supply and the design limitation of the booster which yields a maximum measured boost of 0.60 MeV instead of the specified 1.0 MeV.

The RFQ accelerator system components are described in Table 3.1.

- Ion source - 36.0 keV plasma source at high RF which extracts only D^+ ions for acceleration.

- RFQ - 4 pole/vane system that is water cooled and works on alternating +/- across the poles for simultaneous acceleration and focusing.

- HEBT - Quadrupole magnets that focus the D^+ beam onto the target.

- Booster - Spiral antenna chamber that adds a possible 1.0 MeV energy to the beam. Investigation shows that only 0.60 MeV boost to the beam energy can be obtained and when the booster is off, it acts as a drift space.

TABLE 3.1: Specified and achieved values for the RFQ accelerator system

Condition	Specified Value	Achieved Value
Operating Frequency (MHz)	200.0	200.0
Injection Energy (keV)	36.0	36.0
Maximum Beam Pulse Width (ms)	2.0	2.0
Repetition Rate (MHz)	20.0 - 100.0	20.0 - 100.0
Deuteron Beam Energy (MeV)	5.0	4.60
Average Deuteron Beam Current (mA)	50.0	1.0
Duty Cycle (%)	20.0	0.8 to 1.20
Neutron Flux 4.0 m away from target (n s^{-1} cm^{-2})	1.0×10^7 (Deuterium) 3.0×10^7 (B_4C)	1.0×10^4 (Deuterium) 1.50×10^4 (B_4C)

- Target - The team have access to a gas target that goes from 1.0×10^{-7} mbar to 3.0 bar over 3.0 cm, with D^+ gas and makes use of a high yield, fast neutron spectrum.

- Solid targets used are B_4C, ^9Be, ^6Li and the reaction X(d,n)Y (as described in Section 2.5) to yield neutrons of energy spread unique to each target, which can be tailored for specific applications [1].

Fast Neutron Radiography (FNR) is a primary application at the facility, where imaging is conducted by using a large area scintillating fibre screen, image intensifiers and a cooled CCD camera. Due to a demand for specific applications in which FNR will be applied, development and upgrades have been made to the accelerator system.

3.3 Optimization of High Energy Beam Transport system (HEBT)

3.3.1 Introduction

The High Energy Beam Transport (HEBT) system is used to focus the accelerating deuterium beam onto the RFQ target (gas or solid). The system contained seven Danfysik quadrupole magnets. These magnets form a magnetic field that varies along the radial distance from the longitudinal axis, to focus the beam onto the target. The steel in

TABLE 3.2: Specifications for focusing magnets forming part of the new HEBT setup

Magnets	Focusing Gradient (T m^{-1})	Effective Length (cm)
Q1	4.10	11.0
Q2	4.10	20.0
Q3	4.10	20.0

these quadrupole electromagnets is magnetized by passing an electric current through the coils wrapped around the poles [1].

The magnets making up the original configuration are made up of a smaller magnet, namely *Q1*, having an effective length of 11.0 cm and six larger magnets, namely *Q2* to *Q7*, each having an effective length of 20.0 cm. The maximum focusing gradient for each magnet is 4.10 T m^{-1} with *Q1* requiring up to 20.0 A and *Q2* to *Q7* requiring up to 280.0 A of current. The obstacle created by the seven magnet HEBT system was the short source to detector length, with a maximum of 2.0 m being available for experiments. A decision was made to shorten the HEBT by removing four of the focusing magnets, *Q4* to *Q7*, therefore increasing the source to detector distance to 7.0 m for the experiment. This was the desired length in order to conduct spectral analysis and also enable Time Of Flight (TOF) experiments at a later stage of the project [66].

Removing the focusing magnets had a direct effect on the position of the accelerating beam, therefore simulations of the beam spot size and location were done using the Trace 3D package [67]. This determined the best quadrupole magnet settings that will yield the best beam spot size and location. The magnets used in the new HEBT configuration are shown in Table 3.2.

3.3.2 TRACE 3D optimization for new HEBT configuration

Using the original focusing gradient settings for the magnets, i.e. *Q1* = -3.40 T m^{-1}, *Q2* = -2.23 T m^{-1} and *Q3* = 4.10 T m^{-1}, the TRACE 3D simulates the beam profile and is presented in Figure 3.2, which shows a beam spot size of 7.44 mm diameter.

TRACE 3D [67] is an interactive simulation software that calculates the envelopes of bunched beams incorporating linear space charge forces, through a user defined transport system. The program is FORTRAN based and looks at the two dimensional elliptical projection of the beam in both the transverse and longitudinal projection. The input beam projection is matched to a desired projection using a series of matrix transformations. The transformations performed to optimize the new HEBT design varies the current applied to the quadrupole magnets and calculates the optimal magnet settings to achieve the desired beam spot size at the target. For an improved resolution when performing fast neutron radiography, the beam spot size is desired to be

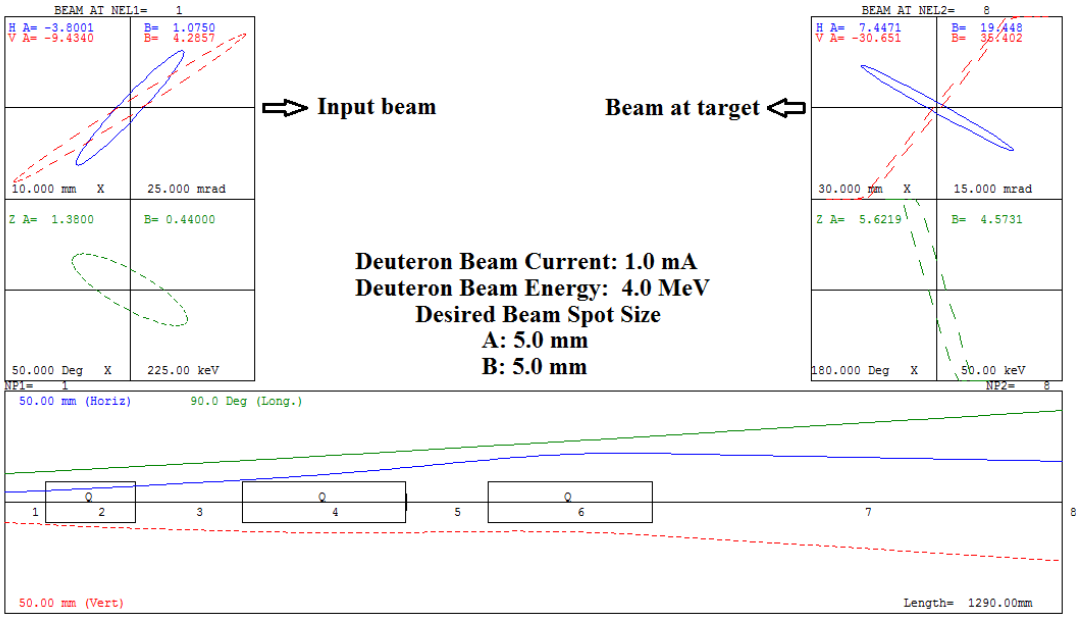

FIGURE 3.2: TRACE 3D simulation of the initial HEBT configuration using the original focusing gradient values for *Q1*, *Q2* and *Q3* showing how the input beam shape is transformed to the beam at target shape

as small as possible. Imposing this on the TRACE 3D varying and matching process, the optimal magnet settings are obtained and presented in Figure 3.3, where *Q1* = -4.0 T m^{-1}, *Q2* = -4.0 T m^{-1} and *Q3* = 4.10 T m^{-1}. This produces a beam spot of 2.57 mm diameter, which is the best achievable beam spot size with the new HEBT setup.

3.3.3 Evaluation of TRACE 3D settings for the new HEBT configuration

To determine the effectiveness of the TRACE 3D simulation presented in Figure 3.3, an examination of the beam location on the target was done, using an aluminium foil target and a beam quadrant analyser.

The aluminium foil target was placed in the path of the accelerating D^+ beam using the magnet settings, *Q1* = -4.0 T m^{-1}, *Q2* = -4.0 T m^{-1} and *Q3* = 4.10 T m^{-1}.

Two experiments were performed, one at 1.50 minutes and the other at 8.0 minutes, with a noticeable beam achieved on the target which is presented in Figure 3.4 and Figure 3.5, respectively. This shows the areas where the deuteron beam interacted with the aluminium foil target at an estimated peak beam current of 1.0 mA.

To confirm this, a quadrant analyser, shown in Figure 3.6, was used to determine the position of the beam as it travels toward the target. The analyser was placed on the beamline directly before the target. It consists of four tantalum plates, each being isolated and arranged in such a way that an orifice is at the centre of the beam pipe.

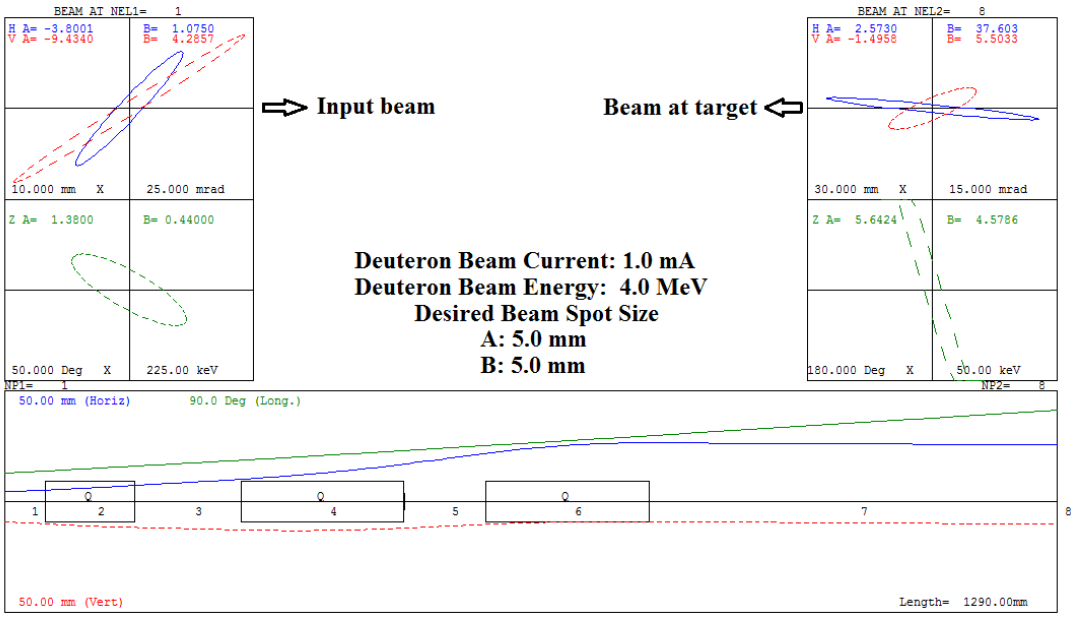

FIGURE 3.3: TRACE 3D simulation of the new HEBT configuration matched to obtain the smallest possible beam spot size showing how the beam is transformed from the input beam shape to the beam at target shape

If correctly aligned, the beam will be picked up by all four plates with equal beam current (measured as a corresponding voltage drop at a 1 MOhm resistor by an oscilloscope). If not at the centre, the beam will strike either or any combination of the plates with a non-uniform distribution.

The signal from the plates is captured and shown in Figure 3.7. Each plate displays the same voltage per division on the oscilloscope. From this we infer that the beam travels through the centre of the quadrant analyser and by extension the beam pipe.

The magnet settings for the new HEBT setup, simulated by using TRACE 3D, show an optimal beam on target for this configuration and will be used to conduct the first and preliminary fast neutron radiography investigations at the RFQ facility.

FIGURE 3.4: Aluminium target after 1.50 minute exposure to an accelerating deuteron beam at a peak beam current of 1.0 mA

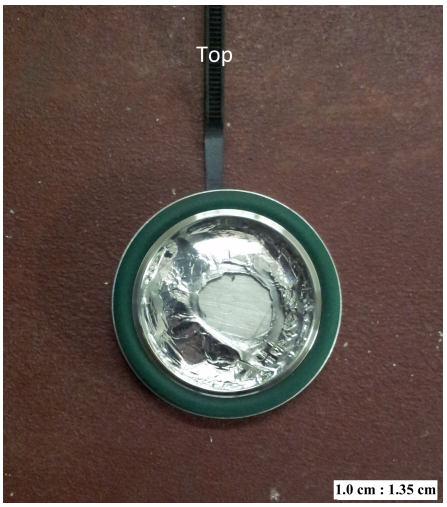

FIGURE 3.5: Aluminium target after 8.0 minute exposure to an accelerating deuteron beam at a peak beam current of 1.0 mA

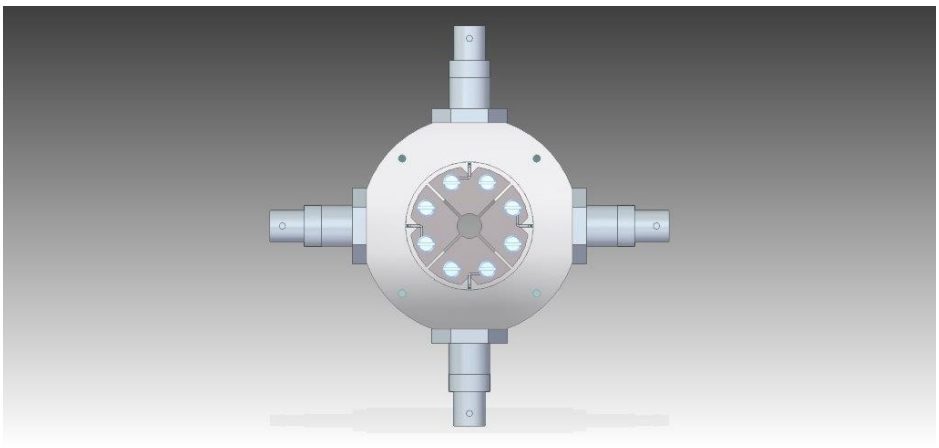

FIGURE 3.6: Illustration of quad analyser used to determine the beam position, incident onto the target

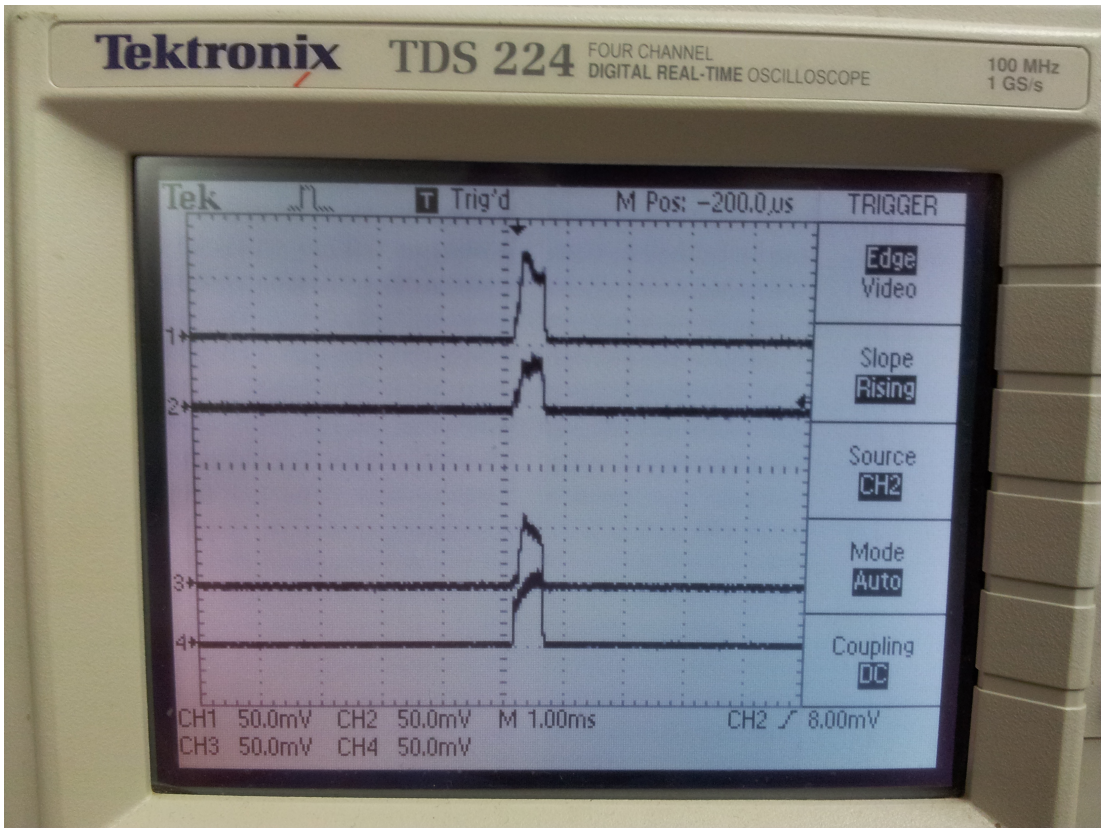

FIGURE 3.7: Oscilliscope showing the equal peaks of the quadrant analyser

3.4 Preliminary studies using the Necsa Fast Neutron Radiography (FNR) system

The Necsa FNR system was described in greater detail in Chapter 2 and was used to perform these preliminary studies using the RFQ as a neutron source.

The current imaging system has been applied in the field of anthropology in order to obtain an image of a human skull, this research being honoured by the IAEA as a success story entitled "The very first application of Fast Neutron Radiography in cultural heritage samples in South Africa under CRP F12024". The result of the study is shown below with the acquired fast neutron radiograph presented in Figure 3.8. The image resolution was effected by a diminished capacity in the CCD chip after years of radiation exposure and the lack of light isolation in the box.

3.5 Necsa FNR system evaluation

3.5.1 Introduction

The FNR system is evaluated using fast neutrons produced by the RFQ accelerator with the achieved flux mentioned in Table 3.1. The fast neutrons range from 1.0 to 10.0 MeV and were generated when a 4.0 MeV deuteron beam interacted with a solid boron carbide target, that induced the B_4C(d,n) reaction, at a peak beam current of 1.0 mA. The FNR system is setup as presented in Figure 3.9 [1] with a Princeton CCD camera (512 $\times$ 512) being used to capture the image. The system uses a fibre scintillator, shown to the right of Figure 3.9 and two image intensifiers (150.0 mm and 50.0 mm diameter) and is cooled to -28°C. The acquired radiograph is captured using WinView software and analysed with Image J.

3.5.2 Detector Linearity

The detector linearity of the Necsa FNR system is tested by calculating the ratio of the maximum, minimum and average counts for both a 15.0 minute and 30.0 minute acquisition. For a linear response the expected ratio of the counts between the two acquisitions should be 2.0. Table 3.3 presents the ratio for the maximum, minimum and average counts.

The ratios presented in Table 3.3 are close to the required value of 2.0 with a maximum of a 1.5% deviation which indicates a linear response of the detector.

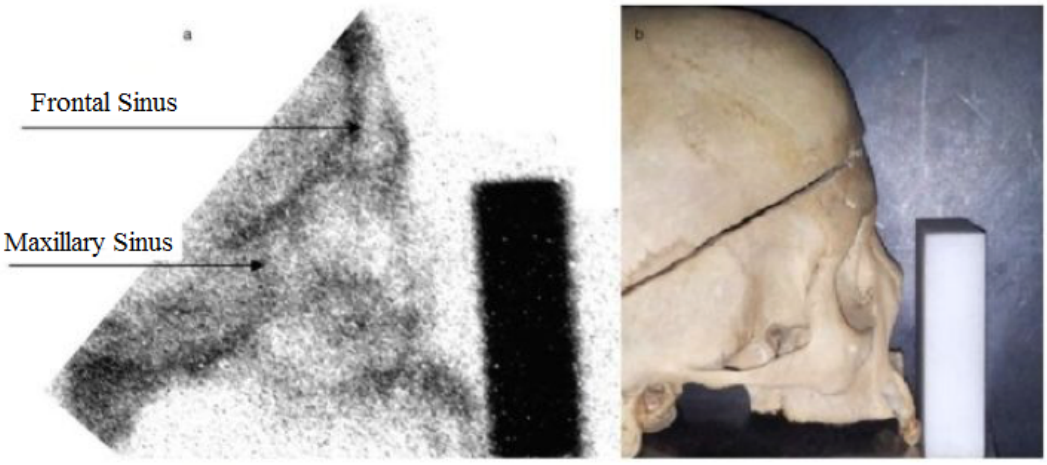

FIGURE 3.8: Fast neutron radiograph of a skull obtained at the RFQ facility using the Necsa FNR system

TABLE 3.3: Comparison between the counts from the 30.0 minute and 15.0 minute acquisitions

Description	Ratio between 30.0 minute and 15.0 minute acquisition
Maximum Counts	2.03
Minimum Counts	2.01
Average Counts	1.98

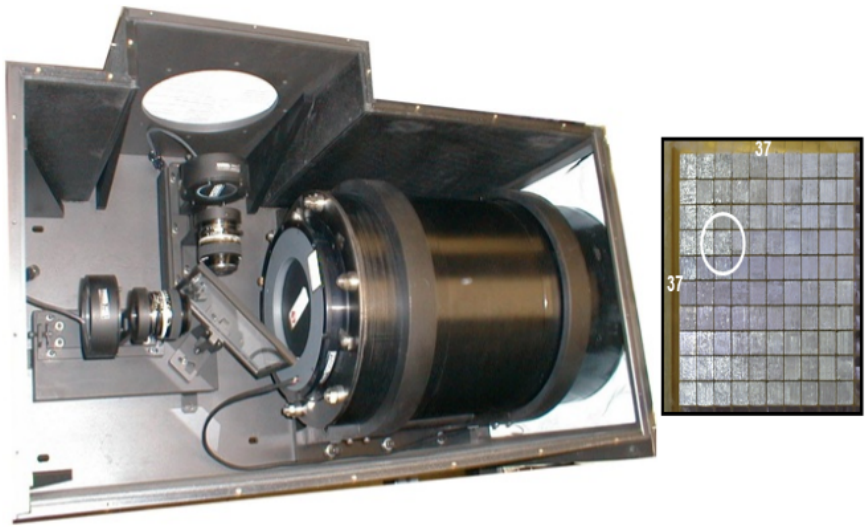

FIGURE 3.9: Layout of the FNR system at Necsa used to perform the preliminary experiments

3.6 Preliminary tests using the Necsa FNR system

3.6.1 Introduction

Preliminary tests were conducted using the RFQ accelerator as a fast neutron source and the FNR system presented in Figure 3.9. The samples used water, a water and sugar mixture, sugar, propanol, polyethylene, and a stainless steel bolt were the samples used.

These initial experiments were carried out to first test the ability of the Necsa FNR system to capture a fast neutron radiograph and to distinguish between different hydrogen rich samples, like water and polyethylene. The ability to observe water is a key element in the experiments carried out and presented in the following chapters. The samples are placed directly in front of the scintillator and the images were acquired using the Princeton CCD Camera, with the radiograph captured using WinView and analysed using Image J software, by applying Equation (2.1).

3.6.2 Test measurements

The initial tests conducted used a hollow polyethylene cylinder, a glass vial filled with water and a stainless steel bolt. A second and third test were performed using beakers filled with water, sugar, a mixture of water and sugar as well as propanol. The noise contributions were removed from the acquired radiographs. Following this, the radiograph with the sample present was divided by the flat field, yielding the resulting radiographs that follow.

The polyethylene cylinder, glass vile filled with water and the stainless steel bolt were initially radiographed and the result is presented in Figure 3.10.

Figure 3.10 shows a distinction between the different attenuating materials in the setup. The next setup consisted of samples of water, water and sugar, sugar and propanol. The results are presented in Figure 3.11 and 3.12.

Figure 3.11 and Figure 3.12 show the presence of all the components of the setup. The observation and distinction of samples that have water present and is applied in greater detail in Chapter 6.

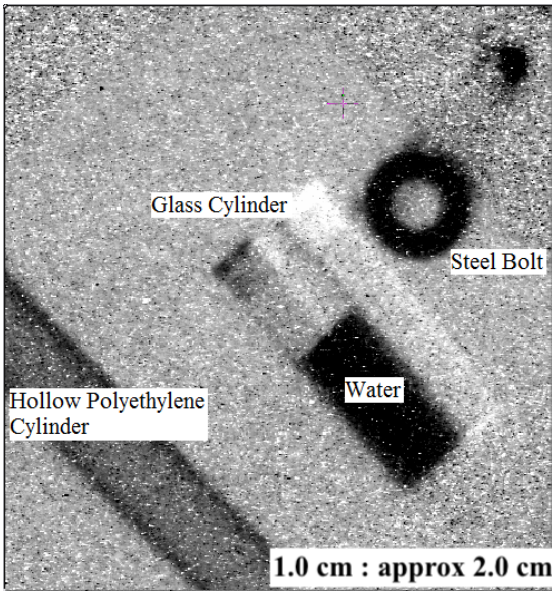

FIGURE 3.10: FNR result for polyethylene cylinder, water vial filled with water and a steel bolt using the Necsa FNR system

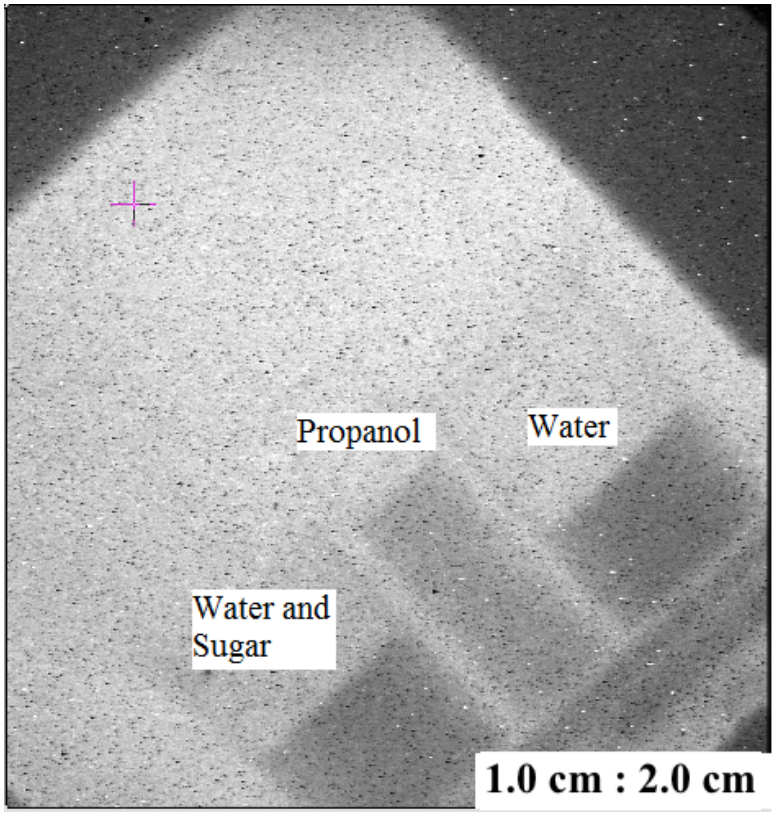

FIGURE 3.11: FNR for water, propanol and a mixture of water and sugar obtained using the Necsa FNR system

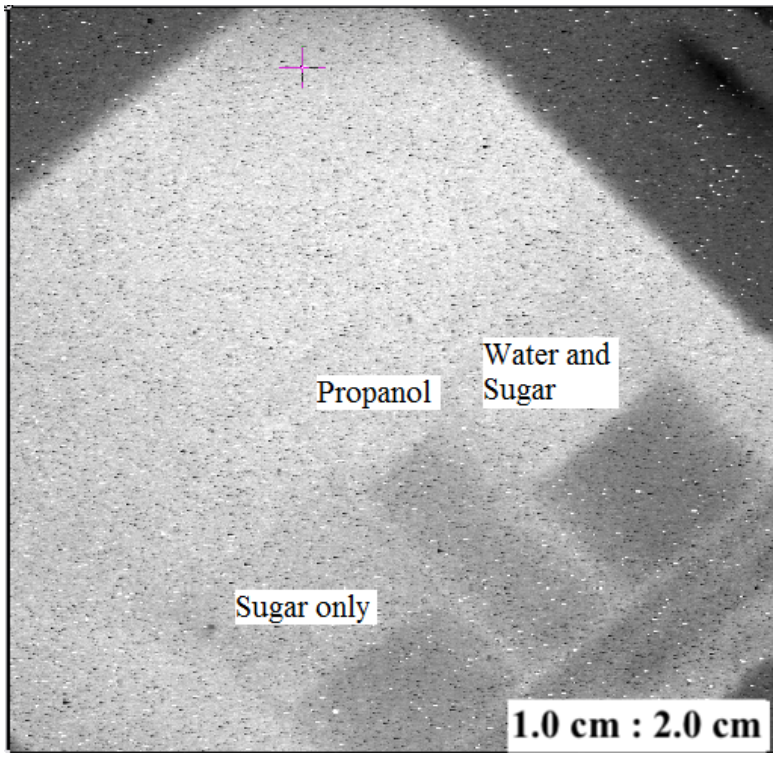

FIGURE 3.12: FNR for sugar, propanol and a mixture of water and sugar obtained using the Necsa FNR system

3.7 Evaluation of samples using FNR on the Necsa system

3.7.1 Introduction

Five samples were used to conduct the preliminary investigation using the Necsa FNR system. The sample characteristics are shown in Table 3.4 [68][69][70].

Each sample causes a different attenuation of the fast neutron beam, which is dependent on the make-up of the material it interacts with.

3.7.2 Sample configuration 1: Polyethylene cylinder, polyethylene block and a steel bolt

The samples mentioned in Table 3.4 were setup in a configuration presented in Figure 3.13, with the yellow areas highlighting the chosen region of interest, for each object.

This configuration interacts with fast neutrons resulting from the aforementioned RFQ system with the resulting FNR shown in Figure 3.14. The resulting FNR are presented in Figure 3.14 which shows the three samples as setup in Figure 3.13. Figure 3.14 shows the presence of the polyethylene block and steel bolt with the polyethylene block, a hydrocarbon, the darkest.

The results obtained here demonstrate an ability to capture a fast neutron radiograph and, for the system, distinguish between hydrogen rich samples (polyethylene) and a high atomic number material (steel bolt) who both have comparative thickness, presented in Table 3.4. Further development and optimization of the technique applied to the Necsa system will be required to perform a more substantive quantitative analysis. One such development will be the use of a mono-energetic beam by employing the D(d,n)He reaction described in Chapter 2 and the development of a new high resolution FNR system described in the following section.

TABLE 3.4: Samples used to perform the preliminary quantitative FNR investigation

Sample	Effective Cross-Sectional Thickness (cm)
Polyethylene Block	1.995
Steel Bolt	1.76
Polyethylene Cylinder	0.555
Case 3a (Water Filled)	1.01
Case 2a (Water Filled)	0.63

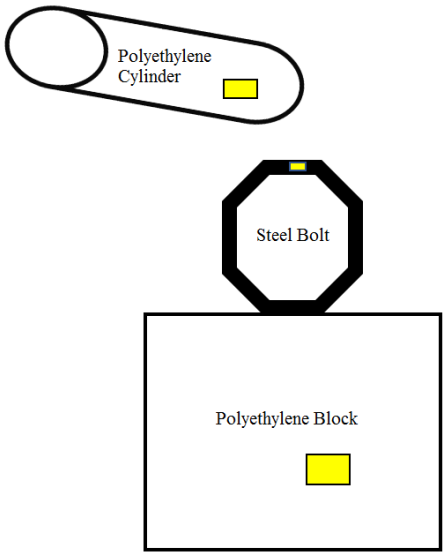

FIGURE 3.13: Sample configuration 1 investigated using the Necsa FNR system

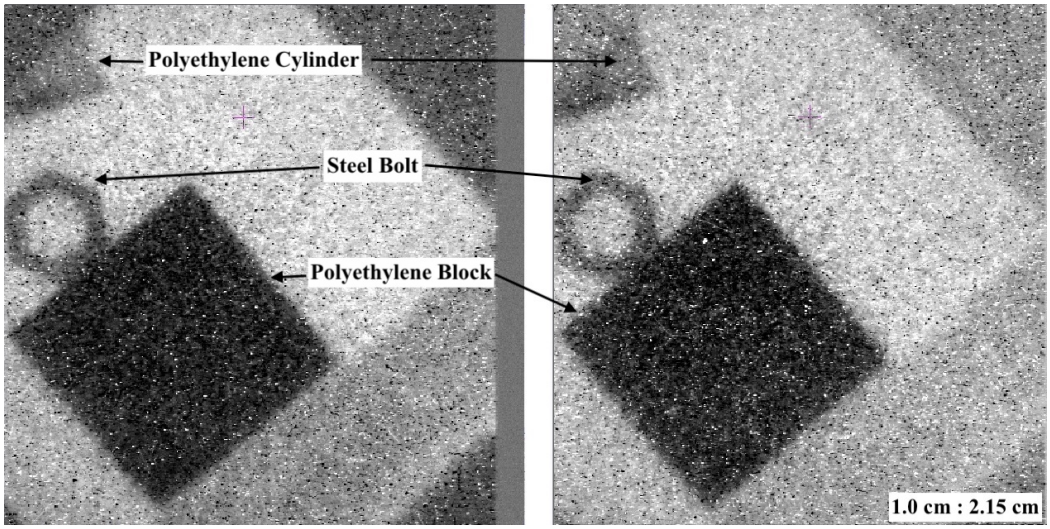

FIGURE 3.14: FNR of sample configuration 1

3.7.3 Sample configuration 2: Aluminium canisters filled with water

Two aluminium canisters mentioned in Table 3.4 were filled with water and setup as shown in Figure 3.15, with the region of interest highlighted in yellow.

The purpose of this experiment was to determine the ability of the Necsa FNR system to image and distinguish water samples of two thicknesses. Two aluminium cannisters with dimensions of 3.90 cm $\times$ 3.90 cm $\times$ 1.01 cm (Case 3a with thickness 1.01 cm) and 3.90 cm $\times$ 3.90 cm $\times$ 0.63 cm (Case 2a with thickness 0.63 cm) were filled with water and placed in the path of the fast neutron generated by the Necsa RFQ. The resulting radiograph is shown in Figure 3.16. For the Necsa system, little observable influence to the resulting FNR, by Case 2a, can be seen in Figure 3.16 which could be a result of scattered neutrons effecting the desired transmission. Case 3a has a larger effective thickness and is visible on the left of Figure 3.16 which shows an ability to image samples above a certain thickness for this system.

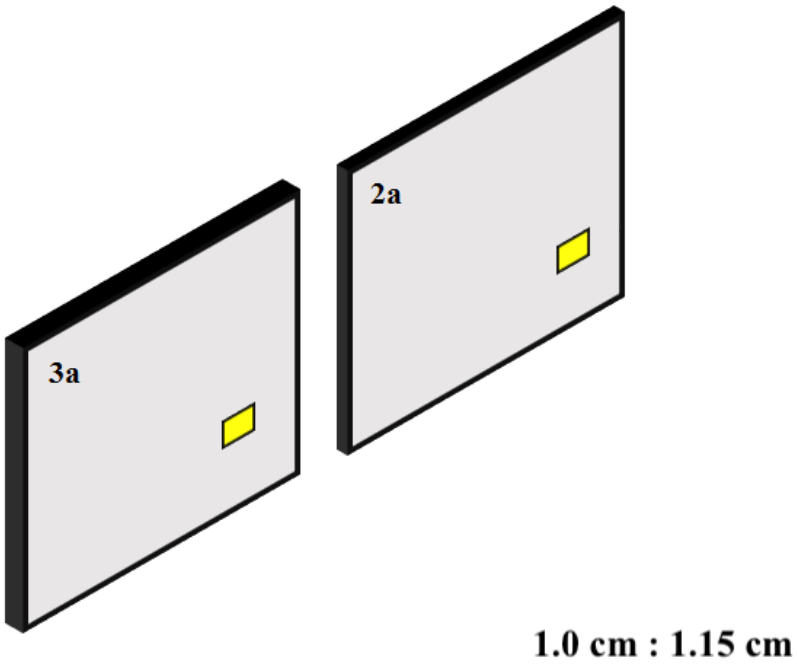

FIGURE 3.15: Sample configuration 2 investigated using the Necsa FNR system

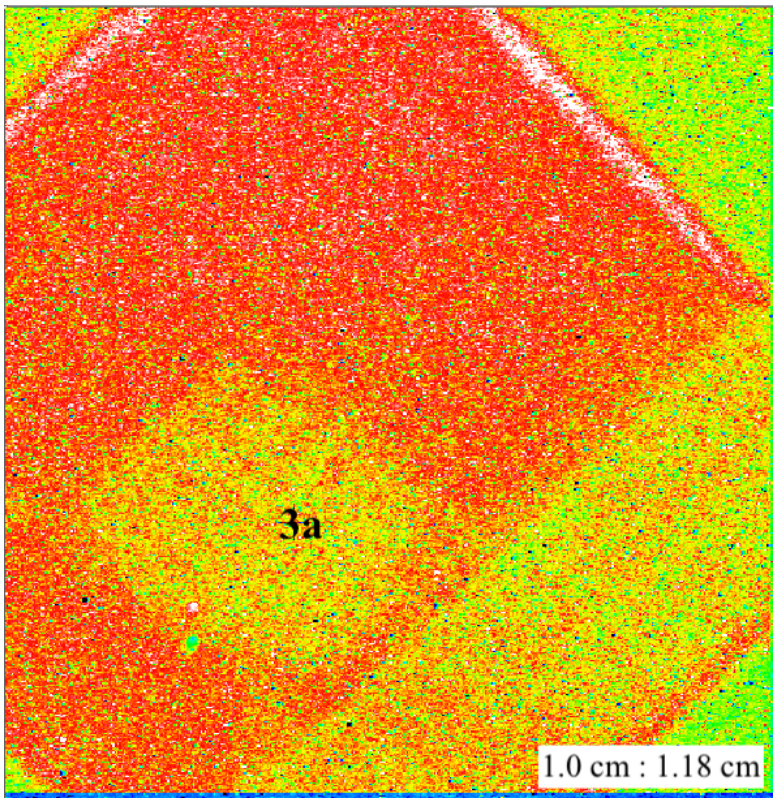

FIGURE 3.16: FNR of sample configuration 2

3.7.4 Further developments to the Necsa FNR system

Due to the outcome obtained using the current Necsa FNR system, an upgrade to the system is under way with the basic design presented in Figure 3.17. This upgrade will improve the image resolution and quality. To save costs, the components that are functionally suited, from the existing system, will be re-used in the new FNR setup while upgrades to the camera, focusing mechanism and camera box will be done.

The new system configuration and design is represented in Figure 3.17, with the new system re-using the main focusing lenses, scintillator, bending mirror and image intensifiers (as described in Chapter 2). The optical system will now be placed on an optical bench with a movable track, which can be moved linearly along the optical path using a stepper motor. This will give the user a remote option to perform both crude and fine focusing. The control of this movable track will be done using an EPIX based control system.

The current Princeton 512 $\times$ 512 CCD camera will be replaced by a FLI Microline 16803 (ML 0402015) CCD camera [71], with a mechanical shutter of 63.50 mm. The camera has a Kodak sensor, KAF 16803, that has a diagonal length of 52.10 mm. The pixel array is 4096 $\times$ 4096, with a pixel size of 9.0 μm. The operating temperature of

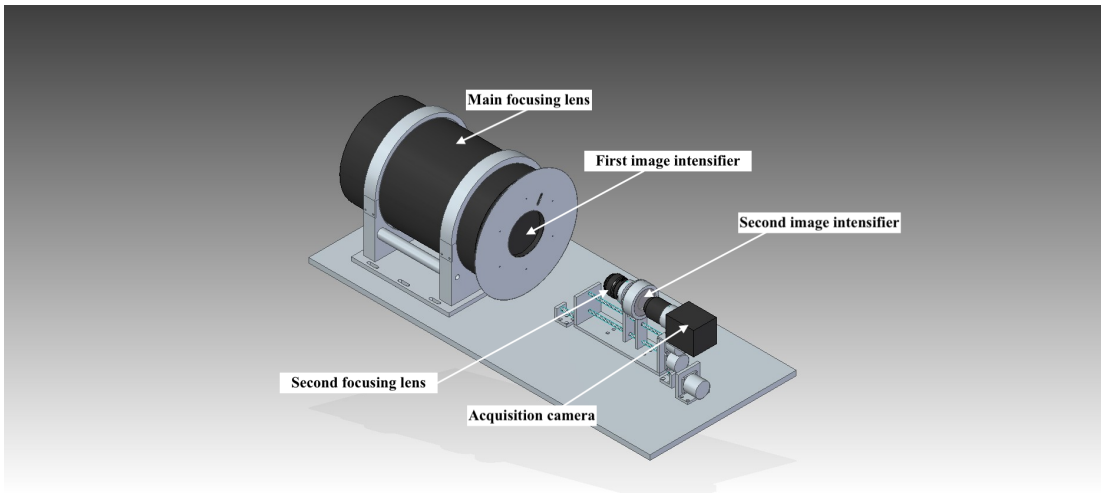

FIGURE 3.17: The design of the optical components of the new FNR system for Necsa

the camera can be as low as -30 °C, using a built-in Peltier cooler. The 4k × 4k resolution will lead to an increase in the overall image quality of this system. The new system will then be able to produce images comparable to an image quality achieved from the TRION detector [11].

The new FNR system is set to be enclosed in an aluminium box that will be coated internally, preferably black anodized, with seals to ensure the camera box is light-tight when closed and in operation. This will be done to minimize the adverse effects caused by stray and scattered light to the resulting radiographs.

Chapter 4

Flow of Media within Tumbling Mills

The technique of fast neutron radiography was used to observe the flow of granular material within a tumbling mill and to examine the steady state of the dynamic flow. Originally the experiments were to be conducted at the RFQ accelerator at Necsa, however unforeseen delays and equipment failure resulted in the experiments being completed at the CV28 Isochronous Cyclotron of the neutron facility at PTB, Braunschweig.

4.1 Introduction

Comminution is a process that reduces the average particle size of granular material to a smaller average particle size through the process of grinding or crushing. A tumbling mill is used to perform comminution and enables the liberation of granular material from larger composites, when applied in the mining industry. The tumbling mill is filled with a mix of granular material, which makes up the mill charge, that undergoes comminution as the tumbling mill rotates. The mill charge takes on six distinct phases [72] during rotation which are shown in Figure 4.1. Each phase is dependent on two parameters, namely the rotation speed of the tumbling mill and the load fraction of granular material placed within the tumbling mill.

The volume of the granular material making up the mill charge is expressed as a fraction of the load volume, f, of the tumbling mill. The load volume is the total critical volume occupied by the mill charge. The fraction is obtained by using the volume of the granular material, the spacing between the granular material components, the volume available within the tumbling mill and is presented in Equation (4.1) [73],

$$f = \frac{V_m}{\eta V_d} \tag{4.1}$$

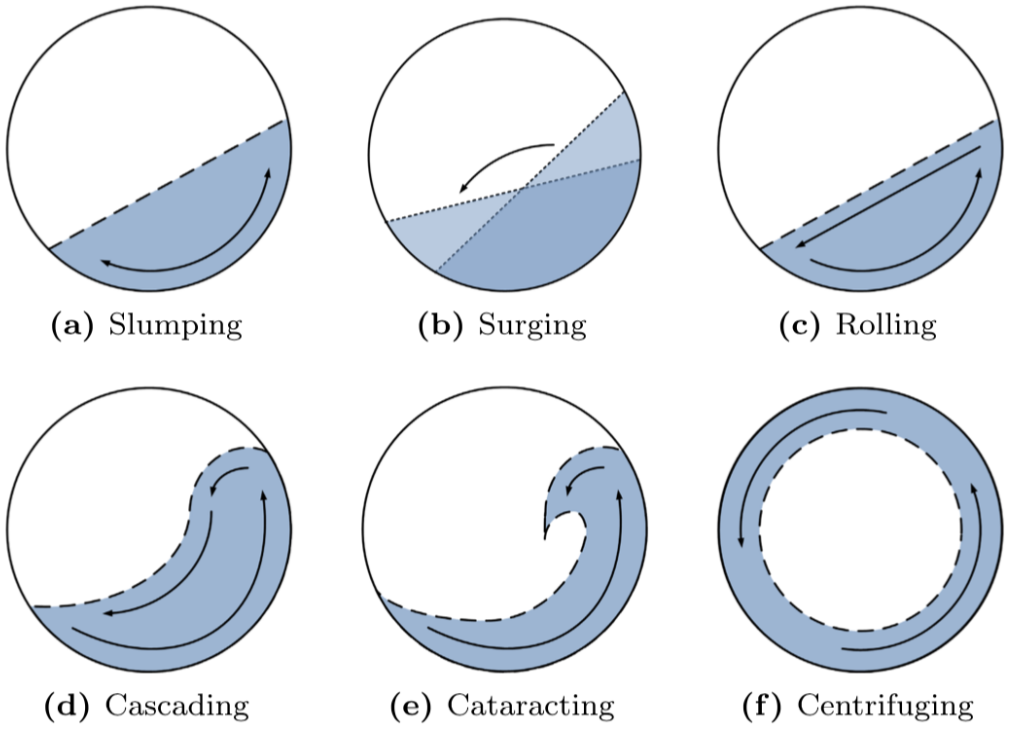

FIGURE 4.1: The different phases formed by the charge within the tumbling mill

where f is the fraction of the load volume, V_m is the volume of the granular material, V_d is the internal volume of the tumbling mill and η is the packing fraction of the granular material. Knowledge of how the mill charge changes in relation to the rotation speed and fraction of the load volume is used to determine the optimal rotation speed required for the best comminution within the tumbling mill. From the shape of the mill charge, the optimal rotation speed is achieved when the total ball angle and average ball lift angle, intersect [74]. Ball here refers to this type of tumbling mill charge and the angles are presented in Figure 4.2 where,

$$\begin{aligned} \text{Total Ball Angle} &= \text{Ball Shoulder} - \text{Ball Toe} \\ \text{Average Ball Lift} &= (\text{Ball Shoulder} + \text{Ball Toe})/2 \end{aligned} \tag{4.2}$$

being dependent on the rotation speed of the mill.

The average ball lift is associated with the amount of granular material of the mill charge present in the best grinding volume of the tumbling mill and the total ball angle is associated with the volume of the tumbling mill in which the optimal grinding will occur. From the intersection of the values in Equation (4.2), the optimal rotation speed of the tumbling mill for the best comminution, will be obtained.

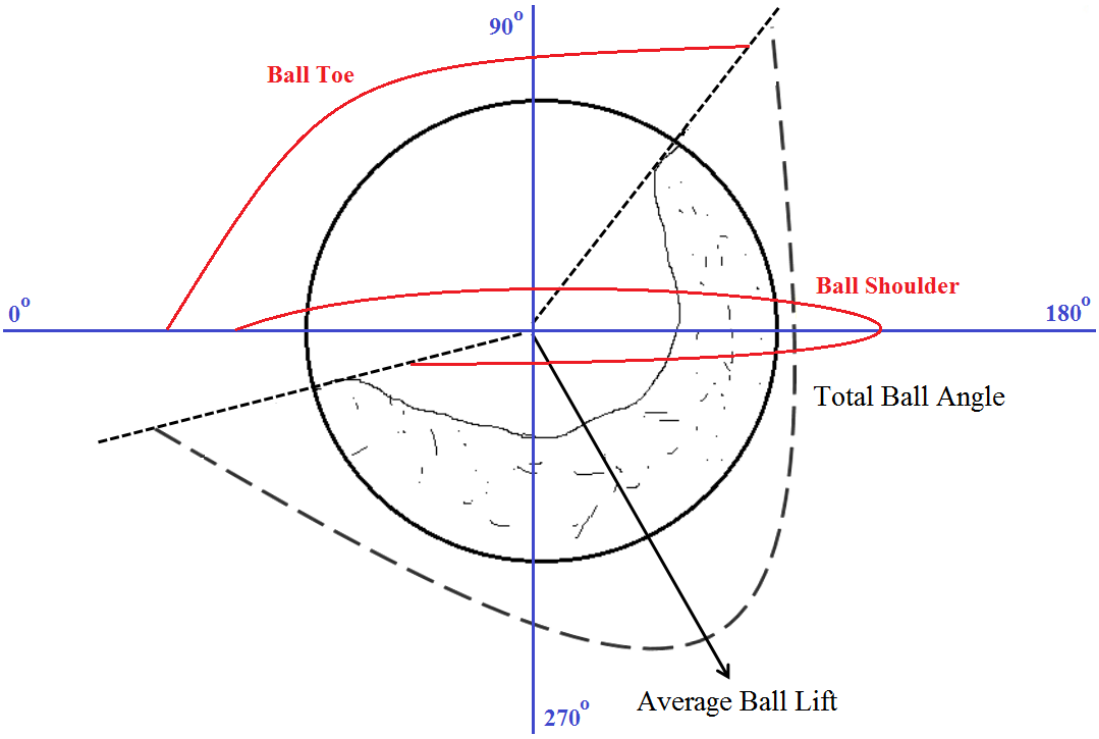

FIGURE 4.2: Representation of the mill charge showing the total ball angle and average ball lift

This observation of the total ball angle and average ball lift of the mill charge is sufficient to obtain the optimal rotation speed, however the shoulder, toe and mill charge can be further subdivided into independent sections that each give an in-depth view of the mill charge while in the dynamic state. This is presented in Figure 4.3 [73] which shows the regions, shoulders, and toes of the mill charge during the steady state of dynamic flow.

The regions of the mill charge are further subdivided into rising, active, in-flight and empty regions shown in Figure 4.3. The definition of each region is:

- Rising region: the region that moves up and shows the quasi-rigid motion of the mill charge.

- Active region: where granular material flows down over the rising region due to gravity. During cataracting and cascading this region together with the toe region is one of the optimal grinding areas within the tumbling mill.

- In-flight region: that part of the mill charge into which granular material is expelled.

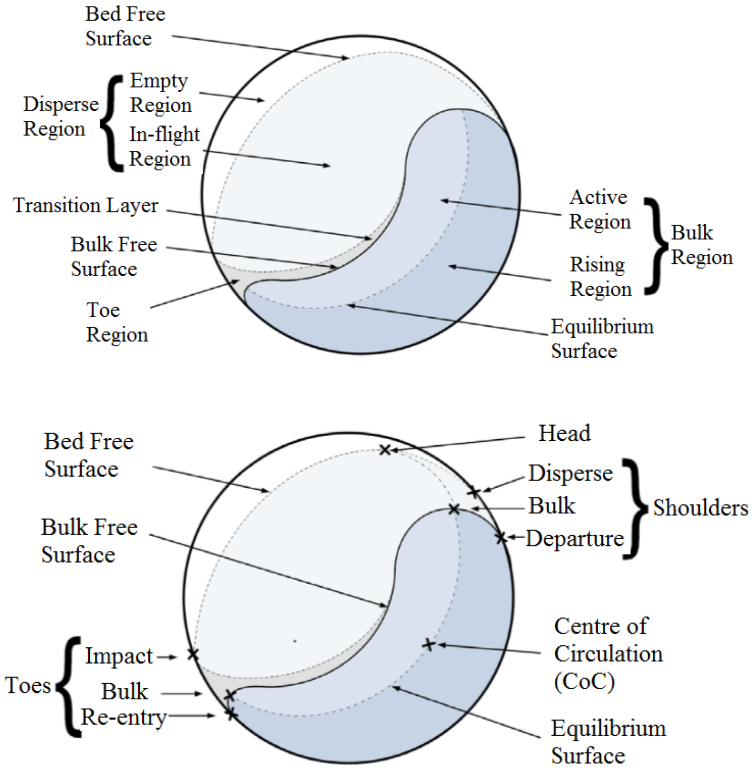

FIGURE 4.3: Important regions and angles of mill charge formed during tumbling

- Empty region: that area of the tumbling mill which none of the granular material will occupy.

The regions are linked together with the rising region being comprised of the majority of the mill charge that then feeds into the active region. The active region, due to its motion, transfers granular material into the in-flight region which is the region that promotes the best mixing and grinding of the mill charge at a given rotation speed and fraction of granular material. The larger active and in-flight regions indicate that a greater volume of the mill charge is undergoing comminution.

Also in Figure 4.3 (right) the shoulders, toes and heights of the charge present in the tumbling mill are illustrated. These provide insight into the movement of the mill charge. These parameters are defined as:

- Head height: the highest point achieved by the outermost layer of the in-flight region.

- Bulk shoulder/toe: granular material in the in-flight region that leaves the region and re-enters in contact with the tumbling mill wall.

- Departure shoulder: granular material from the bulk bed that exits from the tumbling mill wall.

- Impact toe: the point where the granular material in the in-flight regions impacts with those moving in the rising region.

- Re-entry toe: granular material from the active and bulk regions that impact the tumbling mill wall.

The definitions of the shoulder, toes and height together with the distinct regions, give a complete description of the internal dynamics experienced by the mill charge during rotation. This can be used to determine the optimal rotation speed required to achieve the best comminution.

To examine a mill charge with a higher composition of lighter element granular materials requires an interrogating radiation with an interaction cross-section that is higher for the lighter element materials. X-rays have a low cross-section for lighter elements, making it difficult to distinguish the lighter elements [75]. Thermal neutrons, as an interrogating radiation, are limited by their penetration depth and will not be able to penetrate the mill charge in this investigation [76]. The mill charge used in this investigation is therefore interrogated using fast neutrons and the technique of fast neutron radiography. The mill charge, while achieving the steady state of dynamic flow, is observed using fast neutron radiography which shows the phases of the mill charge and also the fill factor of the mill charge along the direction of the penetrating fast neutrons. The shape of the mill charge is used to determine the optimal rotation speed for the best comminution within the tumbling mill.

4.2 Experimental setup

The experiments were carried out on the polychromatic beamline at the PTB facility in Braunschweig. The fast neutron beam is produced via the ^{9}Be(d,n) reaction occurring at the target station of the CN28 isochronous cyclotron. The cyclotron has an incident deuteron beam energy of up to 11.50 MeV. A 3.0 mm thick ^{9}Be target is used with the reaction, producing a fast neutron beam having an energy spectrum ranging from 2.0 MeV to 15.0 MeV with an average neutron energy of 5.50 MeV [77].

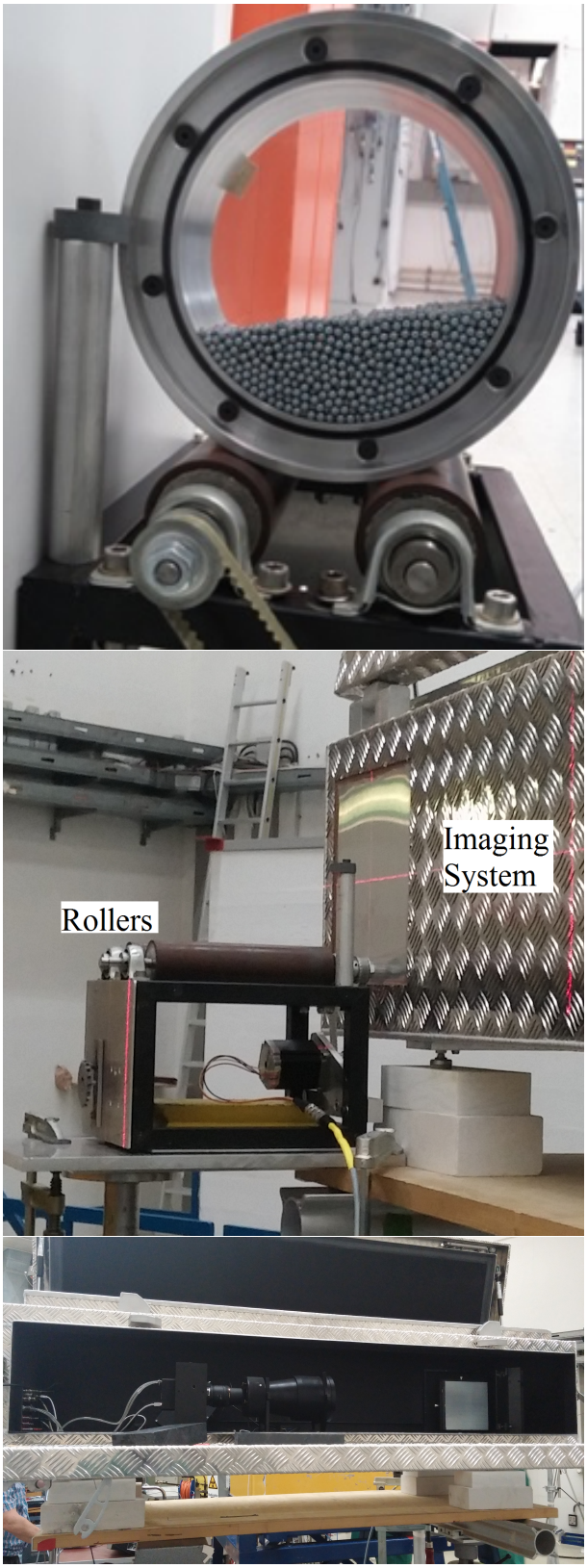

FIGURE 4.4: Experimental setup for the tumbling mill placed on the rollers and the TRION fast neutron radiography system [78]

The deuteron beam spot is approximately 5.0 mm in diameter with a beam current of up to 40.0 μA, yielding a fast neutron flux of 10^8 n s^{-1} cm^{-2}. Fast neutrons are favoured for this study due to the abundance of lighter elements making up the mill charge and the thickness of the sample cannot be traversed by thermal neutrons. The tumbling mill has a cross-sectional length of 7.60 cm and an inner diameter of 14.90 cm. The mill is placed on two rollers, which are connected to a stepper motor via a pulley system and is presented in Figure 4.4. The rotational speed of the drum is determined from the characteristics of the stepper motor used to drive the pulley system. The stepper motor takes 1408 steps to complete a single rotation of the drum.

Each tumbling mill has an intrinsic theoretical speed namely the critical speed V_c, which is determined by its dimensions and is therefore a parameter of the mill itself dependent on its diameter and the size (radius) of the load material constituents making up the mill charge. If the radius of the load material constituents are significantly less than the diameter of the mill, the critical speed will depend solely on the diameter. Every rotation speed used in this study is expressed as a percentage of V_c. The critical speed is calculated using,

$$V_c = \frac{1}{2\pi}\sqrt{\frac{2g}{D-2r}} \tag{4.3}$$

where D is the internal diameter of the tumbling mill, g the acceleration due to gravity and r the average radius of the granular material components. In this study $r \ll D$, the critical speed is [79],

$$V_c = \frac{42.3}{\sqrt{D}}. \tag{4.4}$$

The critical speed for the tumbling mill shown in Figure 4.4 is calculated using Equation (4.4).

$$\begin{aligned} V_c &= \frac{1}{2\pi}\sqrt{\frac{2g}{D-2r}}, \\ \text{with } r \ll D &= \frac{42.3}{\sqrt{D}} \\ \text{and } D &= 7.6 \text{ cm} \\ \implies V_c &= 110.0 \text{ rev min}^{-1} \\ &= 1.80 \text{ rev s}^{-1}. \end{aligned}$$

The images were recorded using the fast neutron imaging detector developed at PTB [78]. The system has a 20.0 $\times$ 20.0 cm^2 optical screen using Bicron plastic fibres of 0.70 mm diameter and 5.0 cm length, manufactured by Crytur [80]. The image is

reflected off the neutron beam axis by a mirror placed at 45° and focussed onto an image intensifier by a lens with an entrance aperture of 12.6 cm at a distance from the scintillator of approximately 75.0 cm. The image is then focussed onto a FLI 4k × 4k CCD camera. The fast neutron radiographs are then analysed using Image J and MATLAB.

The setup presented in Figure 4.4 is placed 1.20 m away from the output of the target collimator of the cyclotron. The mill is placed directly in front of the scintillation screen of the fast neutron imaging detector. When taking a fast neutron image the tumbling mill is started at low speed, accelerates gradually to its end speed and rotates for some time until a steady state of dynamic flow inside the mill is achieved. Then the neutron image is taken. The phase of the mill charge is imaged using the fast neutron detector with several images acquired for an acquisition time of 5.0 seconds.

4.3 Internal mill dynamics and associated parameters

The tumbling mill is filled with different kinds of beads and mixtures of these and is set to rotate at different percentages of the critical speed. Different mill charges are used in the tumbling mill and the phases formed during rotation are captured using fast neutron radiography, for each of the mill charge configurations. For each configuration the regions, angles, shoulders and toes are obtained from the fast neutron radiograph and presented, after the corrections for the flat field, readout noise and beam-off is performed. From the calculated parameters obtained using the fast neutron radiograph, the optimal rotation speed for the mill charge configuration is inferred.

Figure 4.5 illustrates how fast neutron radiography can be used to observe the associated parameters formed by the mill charge during rotation, and this is applied to all the mill charge configurations that were examined. The radiographs were analysed using the ImageJ [24] software. The resulting radiograph is transformed into a colour 'heat' map and the occupied regions are isolated by manually selecting specific regions, using the built-in function of ImageJ.

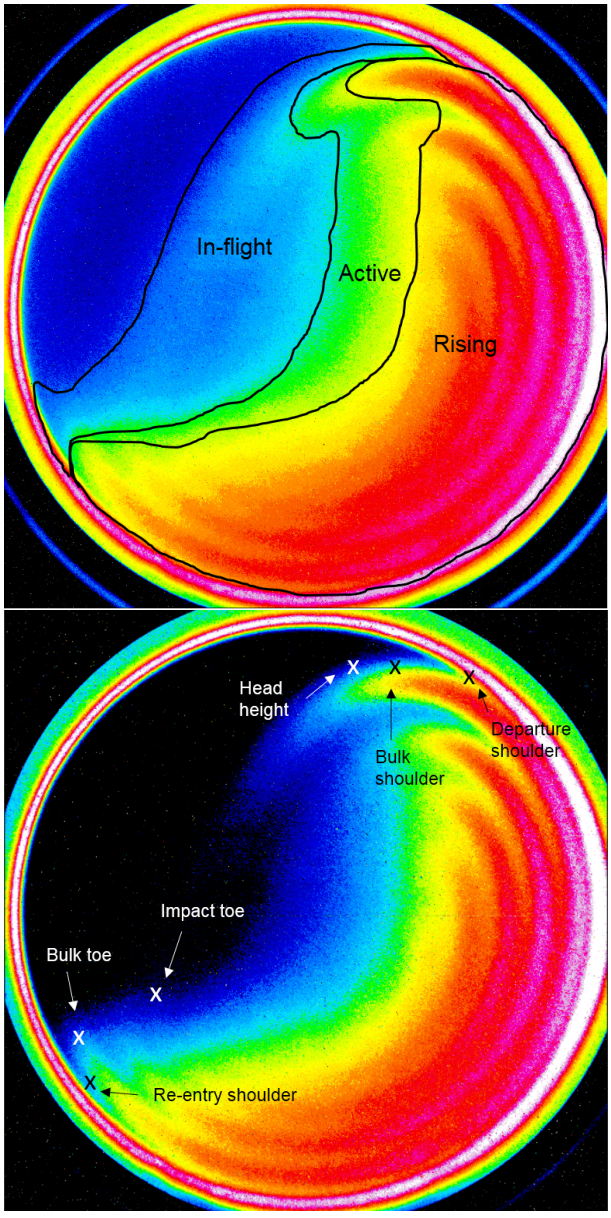

FIGURE 4.5: Important regions and angles of the mill charge made up of 10.0 mm wooden beads rotating at 47.0% V_c occurring during the tumbling phase and acquired using the TRION system

4.3.1 Wooden beads

The tumbling mill was filled with 230.0 g wooden beads of diameter 10.0 mm, which was subjected to a number of different rotation speeds. The mill charge fills the critical volume of the tumbling mill with a packing fraction of $\eta = 0.54$. The mill was set up as shown in Figure 4.4. The resulting fast neutron radiographs are presented in Figure 4.6. Figure 4.6 shows the different phases formed by the mill charge, at different rotation speeds and when compared to Figure 4.5, the mill charge parameters for the case of the 10.0 mm diameter wooden beads, were measured.

The increasing rotation speed results in an increase in the total ball angle and average ball lift [81] of the tumbling mill which is presented in Figure 4.7. The angles presented in Figure 4.7 are normalised to the maximum angle measured during the experimental run while the power drawn by the stepper motor is normalised to the maximum power drawn in a single experimental run. This shows the relationship between the three parameters as a function of the percentage of the critical speed.

An intersection of the total ball angle and average ball lift occurs at 47.0% of the critical speed, for this mill charge, which infers that this is the best rotation speed for comminution to occur in this case. At this speed, Figure 4.7 also shows the power being drawn by the stepper motor. To reaffirm this, a determination of the regions and angles formed by the mill charge, as shown in Figure 4.5, was done and presented in Figure 4.8 and Figure 4.9.

Figure 4.8 shows the area of the rising region decreasing with increasing rotational speed while the areas which promote comminution, the active and in-flight regions, increase in area. The shoulder angles shown in Figure 4.9 also increase with rotational speed which is related to the movement of the mill charge from the rising region into the active region.

The head height position increases with critical speed, as presented in Figure 4.10, which relates to more of the mill charge moving into the in-flight region.

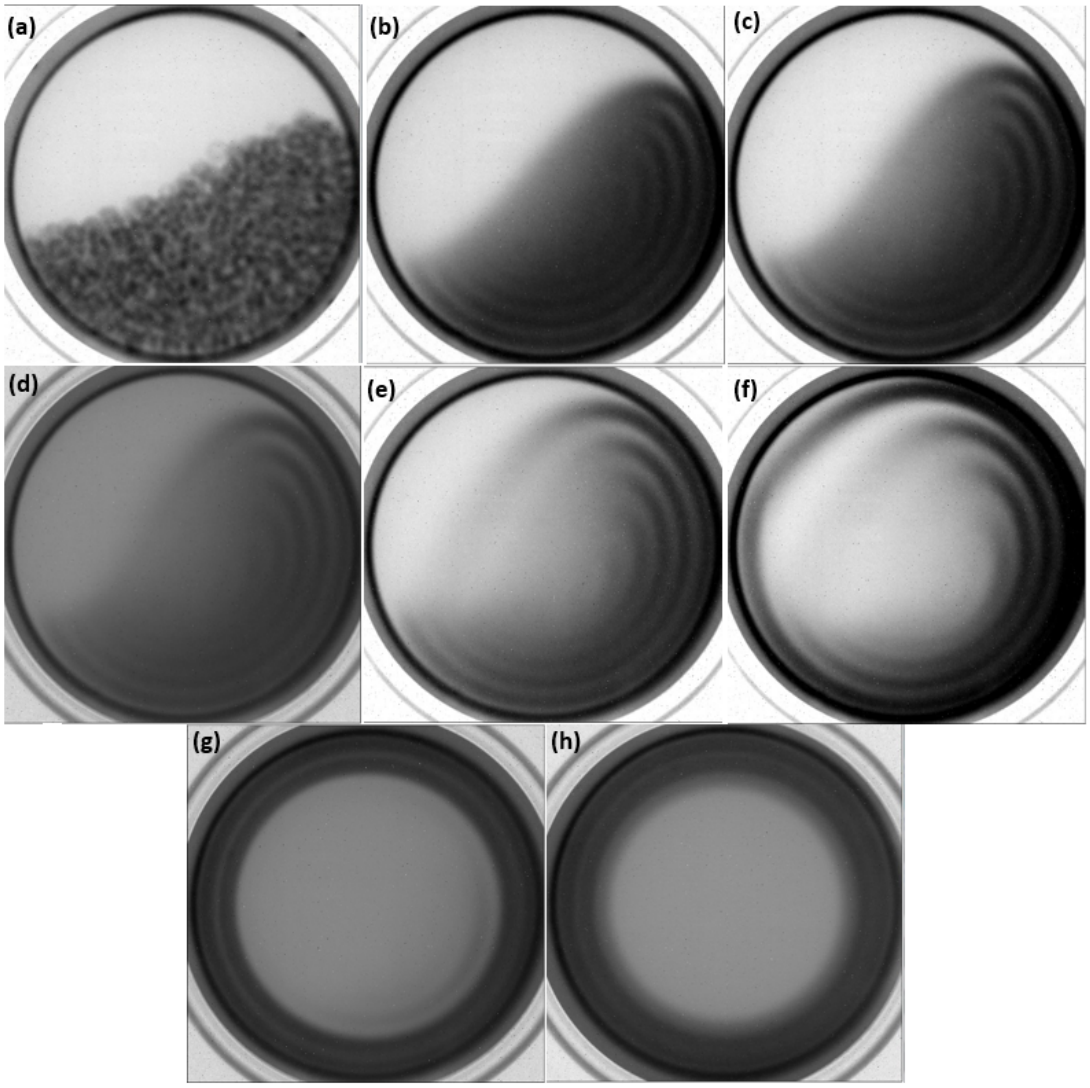

FIGURE 4.6: Fast neutron radiographs showing the phases formed by the mill charge comprised of 10.0 mm diameter wooden beads, for different percentages of the critical speed at (a) rest, (b) 19.5% V_c, (c) 31.0% V_c, (d) 39.0% V_c, (e) 47.0% V_c, (f) 54.5% V_c, (g) 78.0% V_c and (h) 117.0% V_c

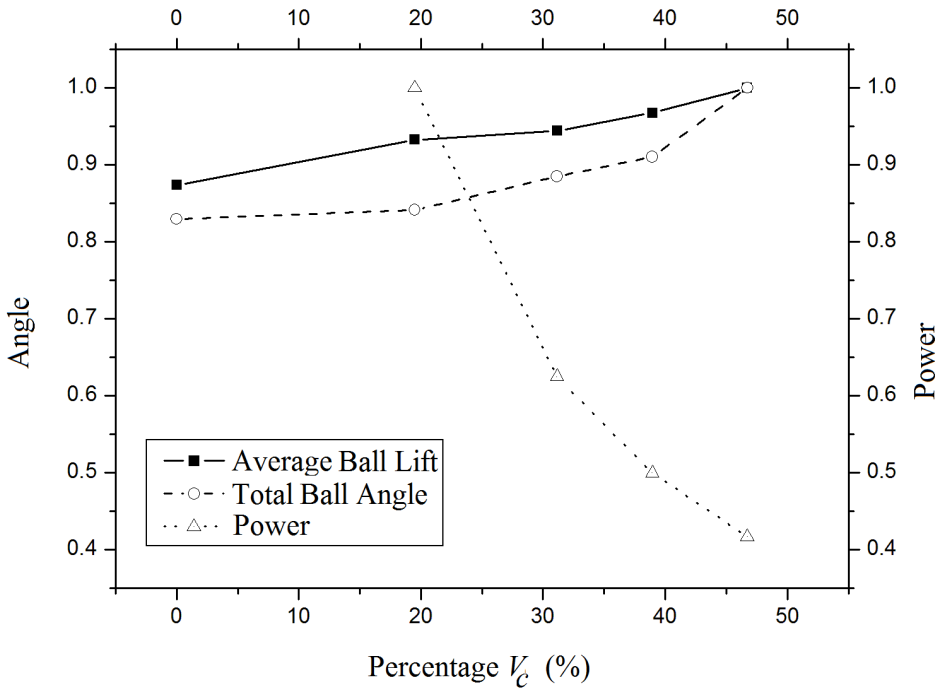

FIGURE 4.7: The total ball angle, average ball lift and power usage of the tumbling mill system with a mill charge comprised of 10.0 mm wooden beads

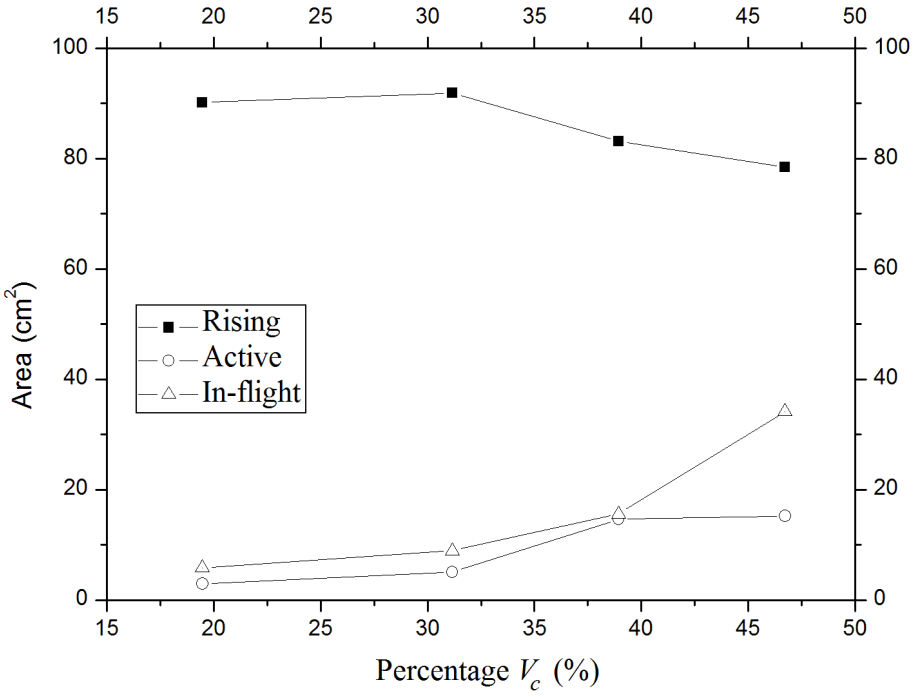

FIGURE 4.8: Area of regions formed by the mill charge comprised of 10.0 mm wooden beads as a function of the percentage of the critical speed

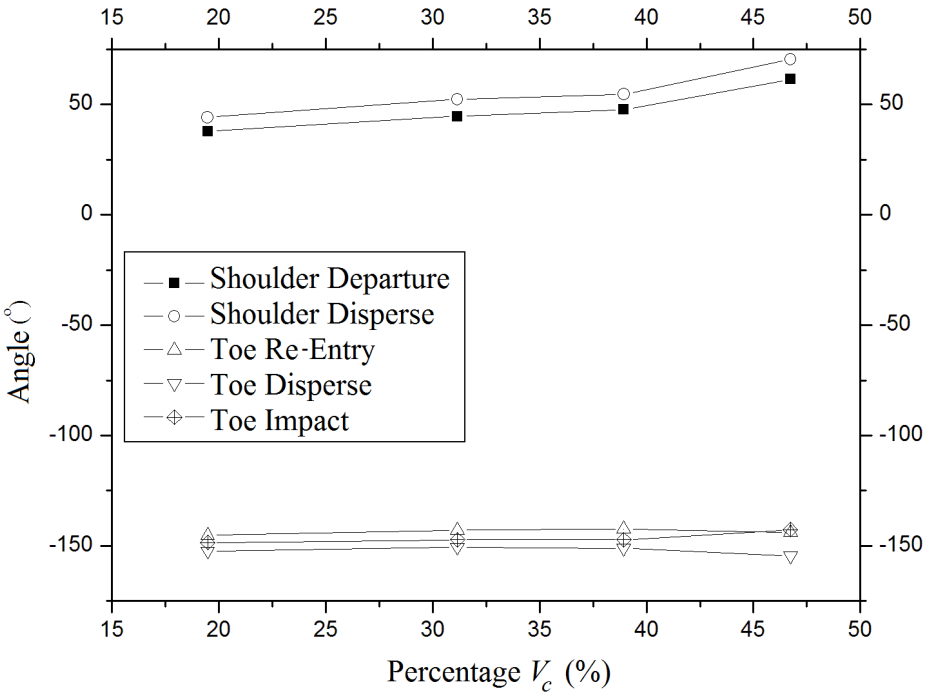

FIGURE 4.9: Angles formed by the mill charge comprised of 10.0 mm wooden beads as a function of the percentage of the critical speed

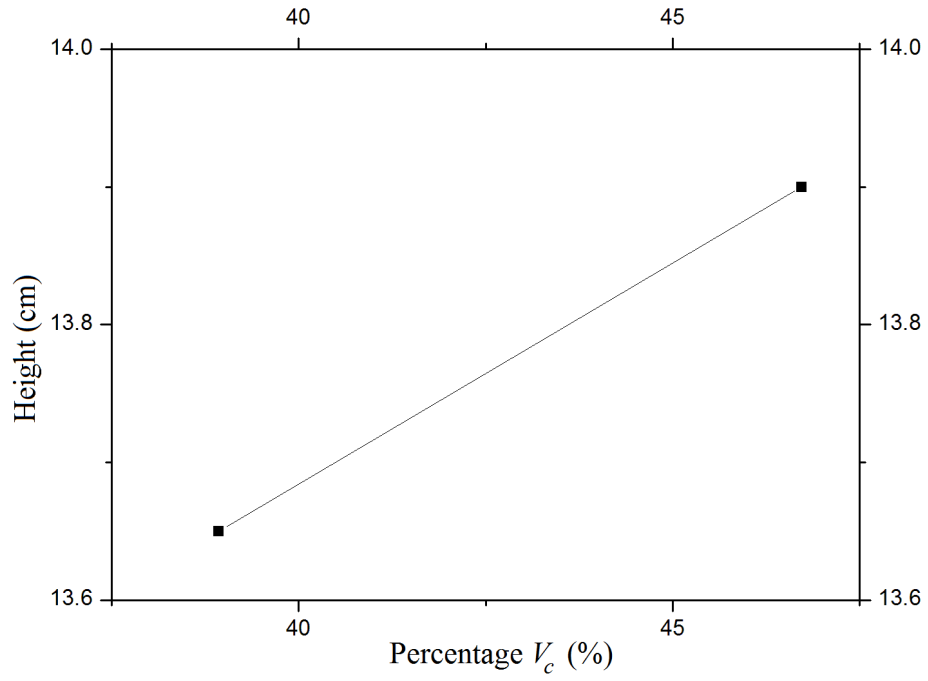

FIGURE 4.10: The head height formed by the mill charge comprised of 10.0 mm wooden beads as a function of the percentage of the critical speed

4.3.2 Glass beads

In this scenario, the tumbling mill was filled with glass beads having diameters of 6.0 mm, 8.0 mm and 12.0 mm with an associated mass of 275.0 g, 293.0 g and 334.0 g, respectively. This mixture of glass beads was subjected to a number of different rotation speeds. The mill charge fills the critical volume of the tumbling mill with a packing fraction of $\eta = 0.449$. The mill was set up as shown in Figure 4.4. The resulting fast neutron radiographs are presented in Figure 4.11. Figure 4.11 shows the different phases formed by the mill charge, at different rotation speeds and when compared to Figure 4.5, the mill charge parameters for the case of the mixture of glass beads were measured.

The increasing rotation speed results in an increase in the total ball angle and average ball lift [81] of the tumbling mill which is presented in Figure 4.12. The angles presented in Figure 4.12 are normalised to the maximum angle measured during the experimental run while the power drawn by the stepper motor is normalised to the maximum power drawn in a single experimental run. This shows the relationship between the three parameters as a function of the percentage of the critical speed.

An intersection of the total ball angle and average ball lift occurs at 47.0% and 70.0% of the critical speed, shown in Figure 4.12, for this mill charge which infers that these are the best rotation speeds for comminution to occur. It is at 70.0% V_c that the power being drawn by the stepper motor is lowest. To determine which of the two rotational speeds are best suited to the best comminution, further analyses of the regions and angles formed by the mill charge, as shown in Figure 4.5, were done and presented in Figure 4.13 and Figure 4.14.

Figure 4.13 shows the area of the rising region decreasing with increasing rotational speed while the areas which promote comminution, the active and in-flight regions, increase in the area. Comparing this to the increasing shoulder angles presented in Figure 4.14, the optimal rotation speed range is narrowed to between 62.0% and 70.0% of the critical speed.

The head height position is maximum at 70.0% of the critical speed, as shown in Figure 4.15, which relates to more of the mill charge moving into the in-flight region and is therefore the optimal rotation speed for the best comminution for this mill charge.

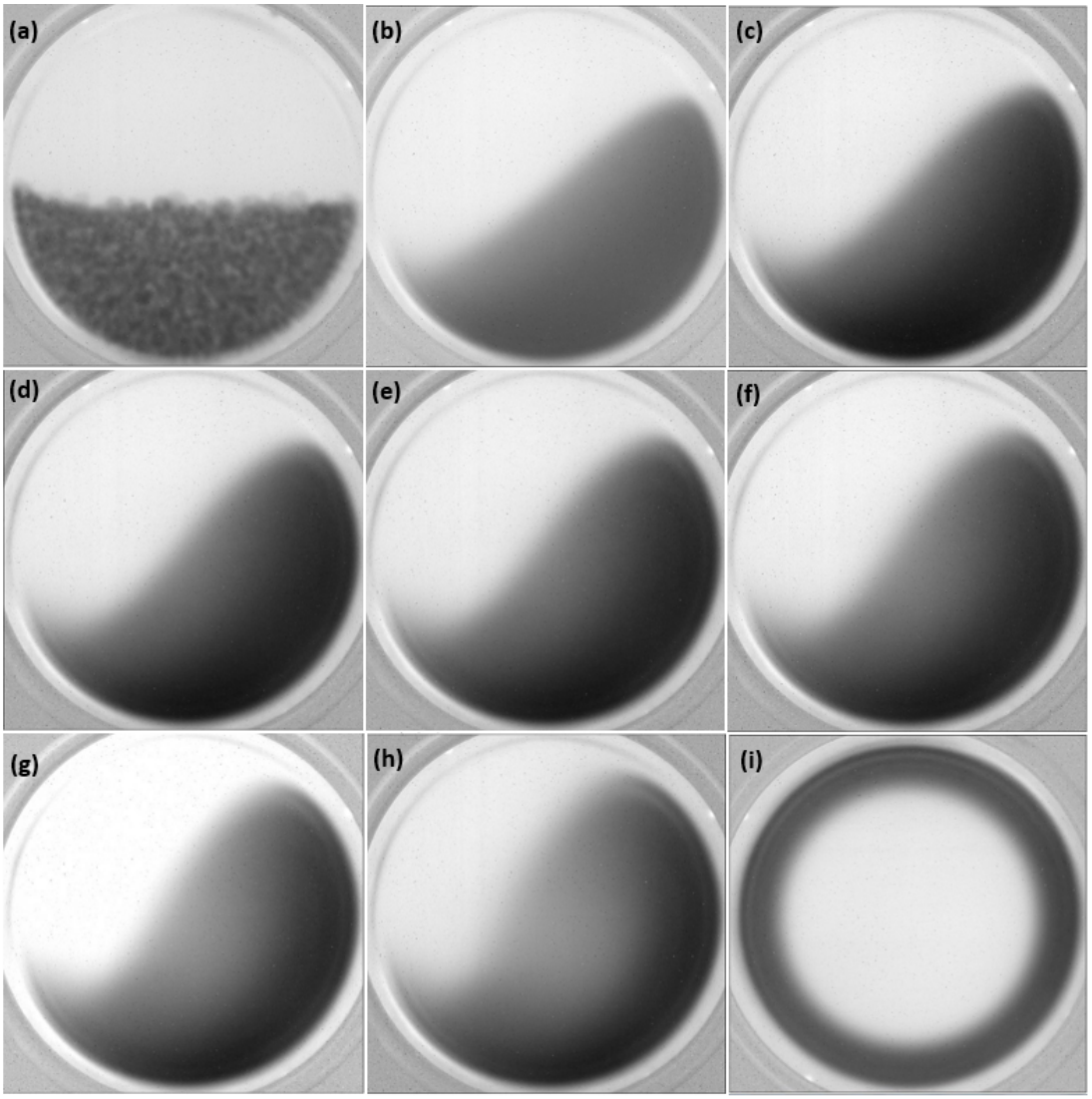

FIGURE 4.11: Fast neutron radiographs showing the phases formed by the mill charge comprised of 6.0 mm, 8.0 mm and 12.0 mm diameter glass beads, for different percentages of the critical speed with (a) rest, (b) 19.5% V_c, (c) 31.0% V_c, (d) 39.0% V_c, (e) 47.0% V_c, (f) 54.5% V_c, (g) 62.0% V_c, (h) 70.0% V_c and (i) 101.0% V_c

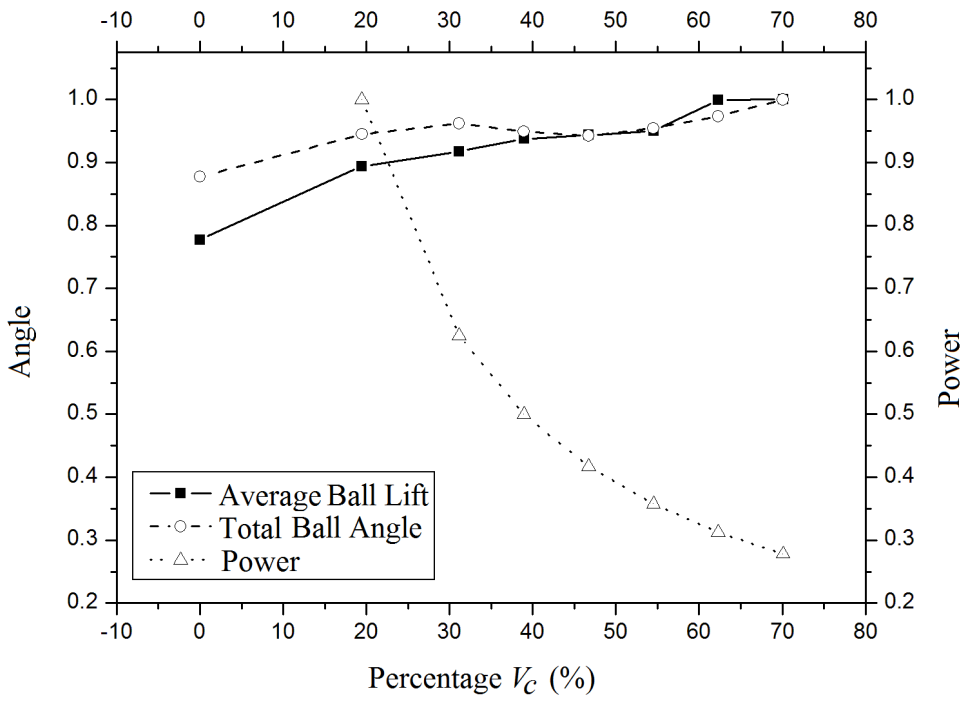

FIGURE 4.12: The total ball angle, average ball lift and power usage of the tumbling mill system with a mill charge comprised of 6.0 mm, 8.0 mm and 12.0 mm glass beads

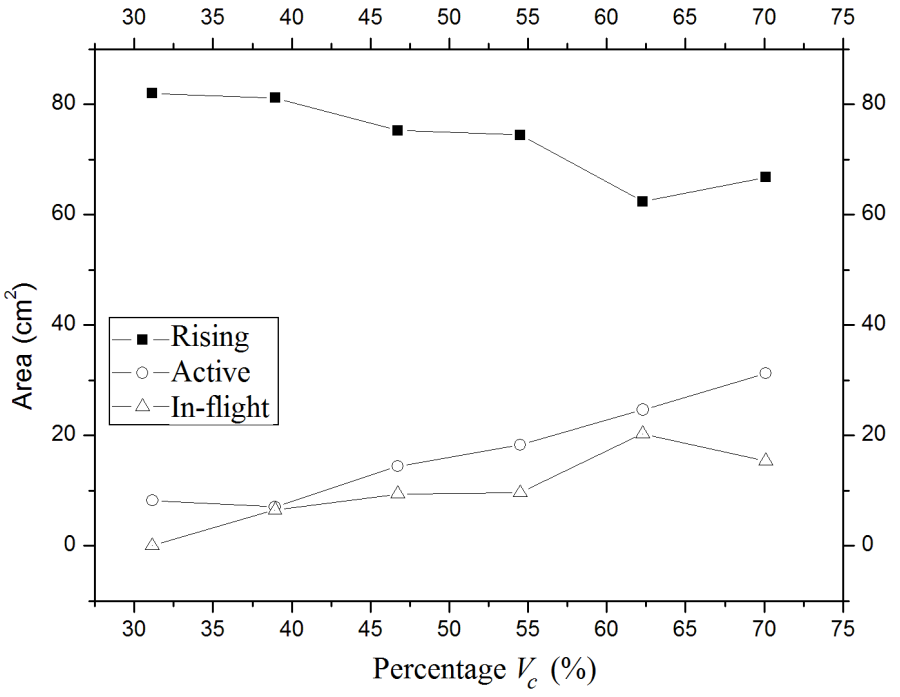

FIGURE 4.13: Area of regions formed by the mill charge comprised of a mixture of 6.0 mm, 8.0 mm and 12.0 mm diameter glass beads as a function of the percentage of the critical speed

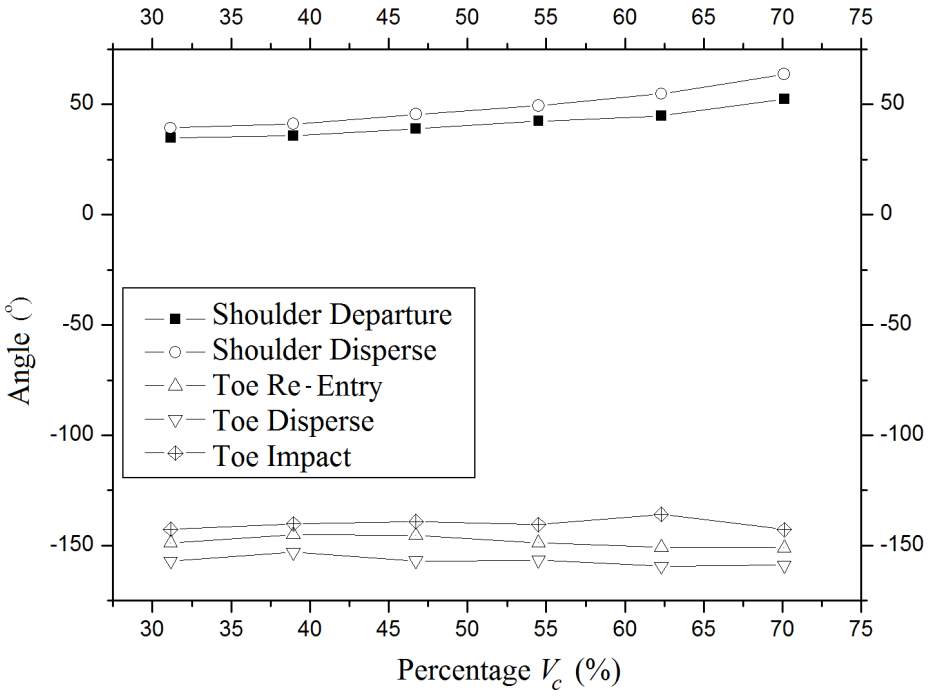

FIGURE 4.14: Angles formed by the mill charge comprised of a mixture of 6.0 mm, 8.0 mm and 12.0 mm diameter glass beads as a function of the percentage of the critical speed

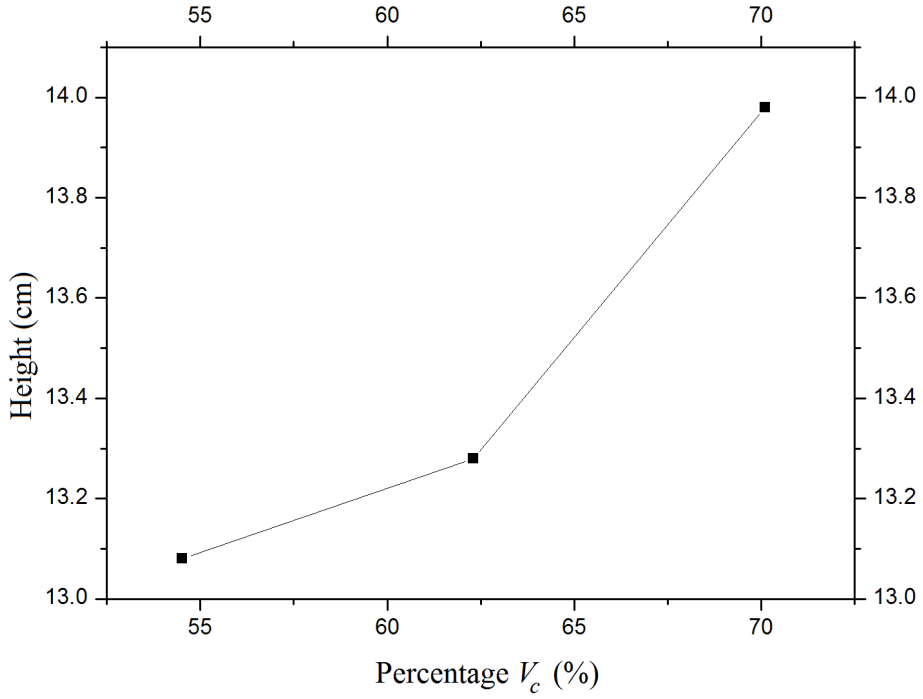

FIGURE 4.15: The head height formed by the mill charge comprised of 6.0 mm, 8.0 mm and 12.0 mm glass beads as a function of the percentage of the critical speed

4.3.3 Wood and plastic beads

In this scenario, the tumbling mill was filled with a mixture of wood and plastic beads having diameters of 6.0 mm and 5.50 mm with an associated mass of 340.0 g and 114.0 g, respectively. This mixture of beads was subjected to a number of different rotation speeds. The mill charge fills the critical volume of the tumbling mill with a packing fraction of $\eta = 0.59$. The mill was set up as shown in Figure 4.4. The resulting fast neutron radiographs are presented in Figure 4.16. Figure 4.16 shows the different phases formed by the mill charge, at different rotation speeds and when compared to Figure 4.5, the mill charge parameters for the case of the mixture of wood and plastic beads were measured.

The increasing rotation speed results in an increase in the total ball angle and average ball lift [81] of the tumbling mill which is presented in Figure 4.17. The angles presented in Figure 4.17 are normalised to the maximum angle measured during the experimental run while the power drawn by the stepper motor is normalised to the maximum power drawn in a single experimental run. This shows the relationship between the three parameters as a function of the percentage of the critical speed.

An intersection of the total ball angle and average ball lift occurs at 54.5% of the critical speed, shown in Figure 4.17, for this mill charge which infers that this is the best rotation speed for comminution to occur. At this speed, Figure 4.17 also shows a lower power being drawn by the stepper motor. To reaffirm this, a determination of the regions and angles formed by the mill charge, as shown in Figure 4.5, was done and presented in Figure 4.18 and Figure 4.19.

Figure 4.18 shows the area of the rising region decreases with increasing rotational speed while the areas which promote comminution, the active and in-flight regions, increase in the area. Comparing this to the shoulder angles presented in Figure 4.19, the rotation speed for the best comminution for this mill charge is 54.5% of the critical speed.

The head height position is maximum at 54.5% of the critical speed, as shown in Figure 4.20, which relates to more of the mill charge moving into the in-flight region and is therefore the optimal rotation speed for the best comminution for this mill charge.

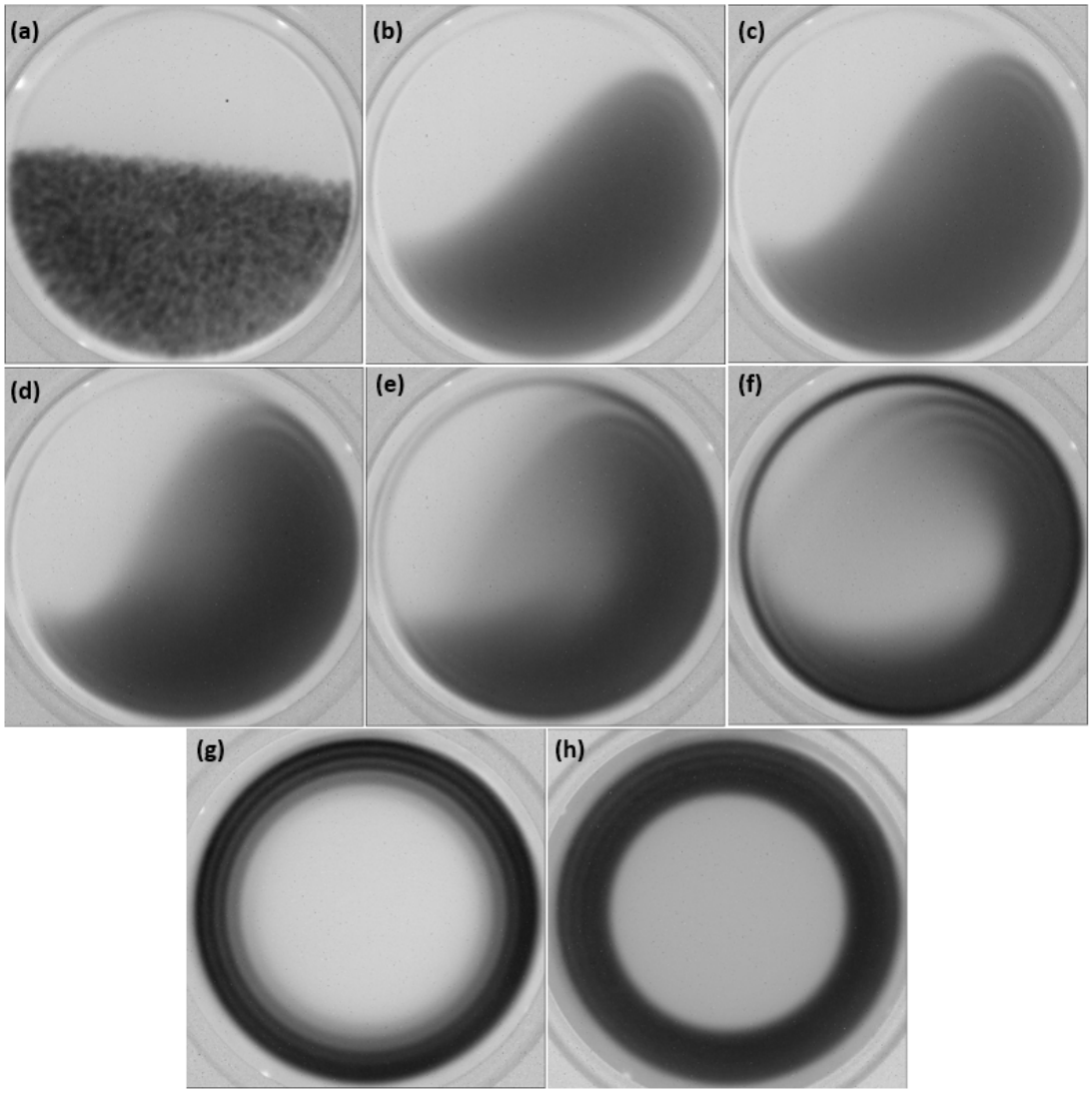

FIGURE 4.16: Fast neutron radiographs showing the phases formed by the mill charge comprised of 6.0 mm and 5.50 mm diameter wood and plastic beads, for different percentages of the critical speed with (a) rest, (b) 19.5% V_c, (c) 31.0% V_c, (d) 39.0% V_c, (e) 47.0% V_c, (f) 54.5% V_c, (g) 78.0% V_c and (h) 101.0% V_c

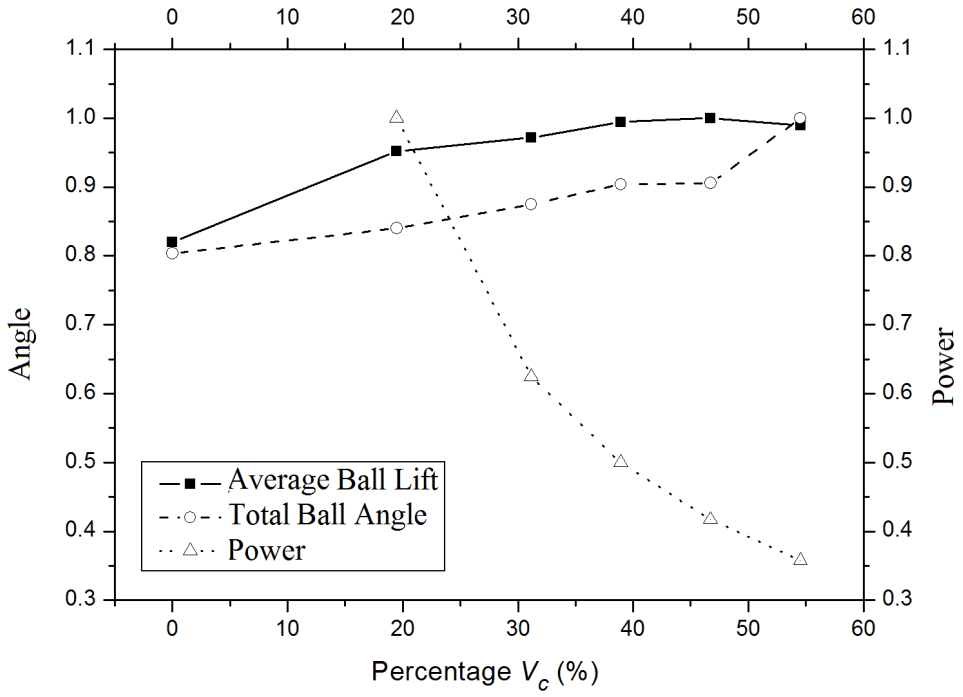

FIGURE 4.17: The total ball angle, average ball lift and power usage of the tumbling mill system with a mill charge comprised of 6.0 mm diameter wooden beads and 5.50 mm diameter plastic beads

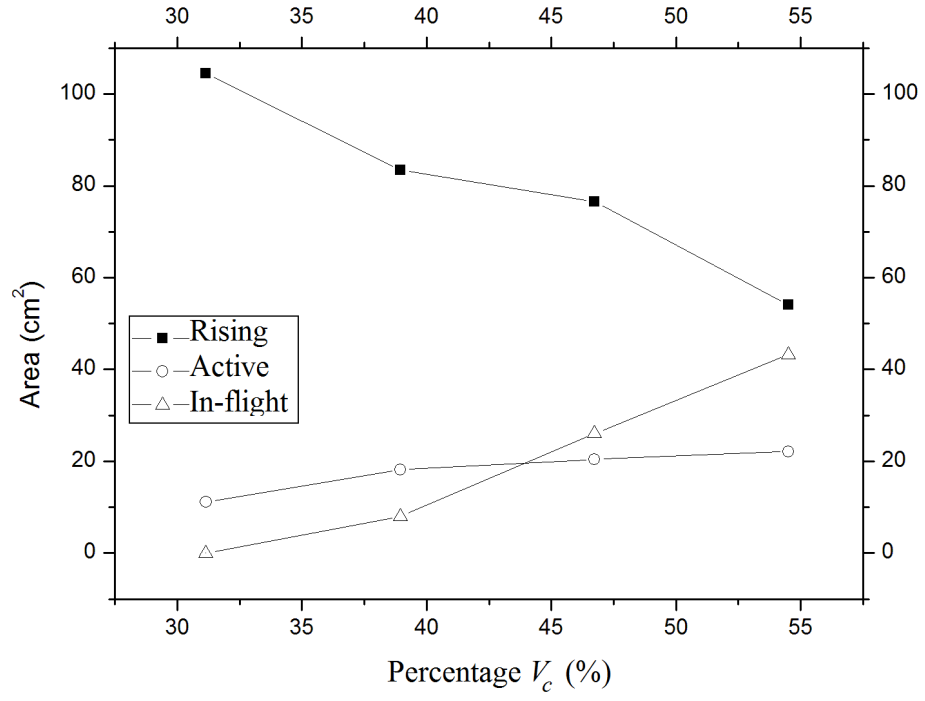

FIGURE 4.18: Area of regions formed by the mill charge comprised of a mixture of 6.0 mm diameter wooden beads and 5.50 mm diameter plastic beads as a function of the percentage of the critical speed

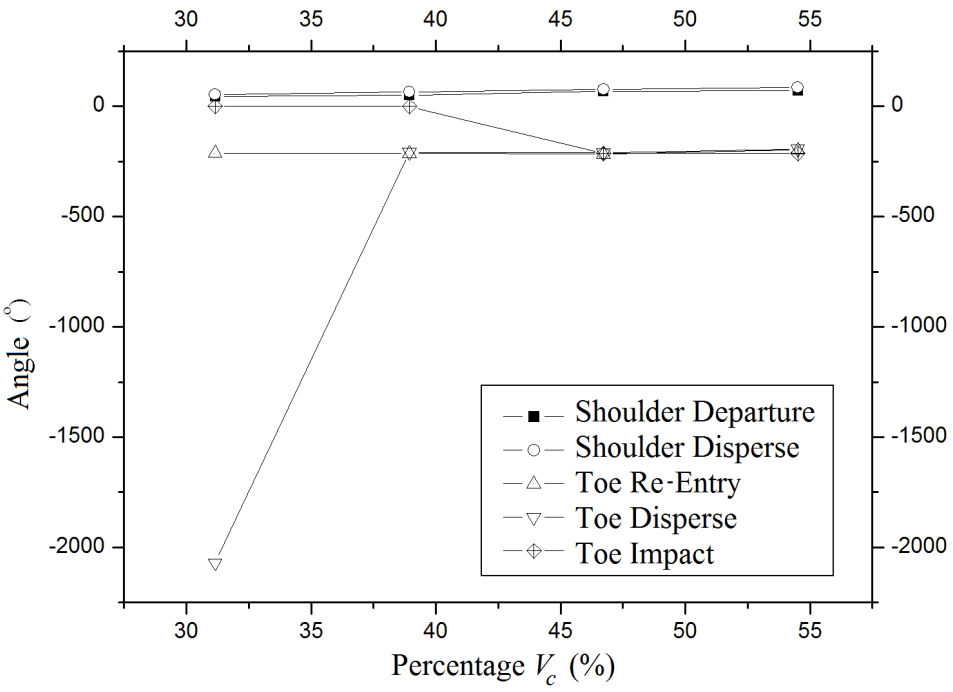

FIGURE 4.19: Angles of regions formed by the mill charge comprised of a mixture of 6.0 mm diameter wooden beads and 5.50 mm diameter plastic beads as a function of the percentage of the critical speed

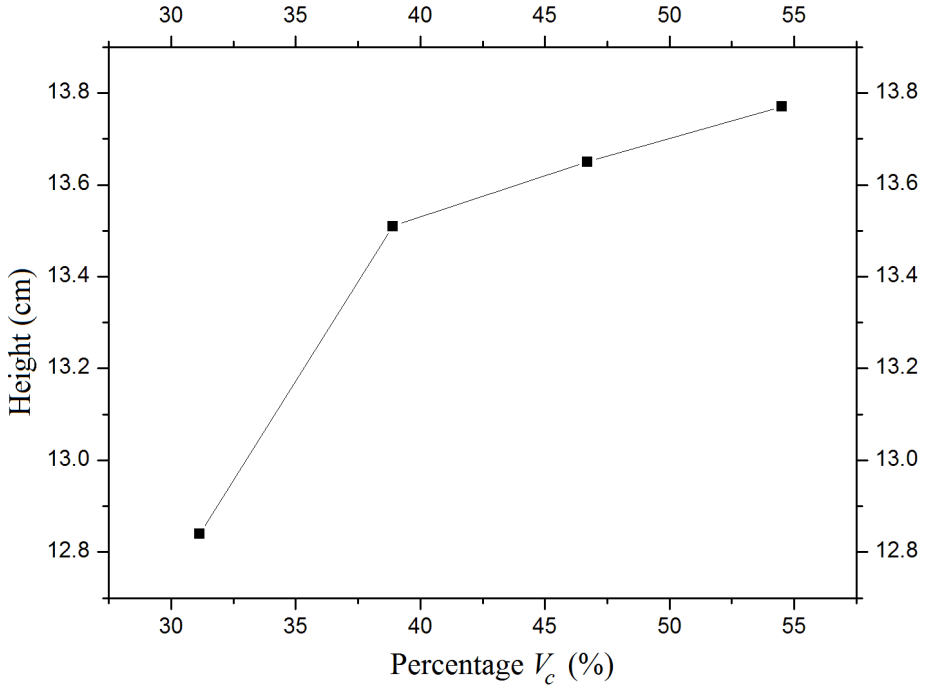

FIGURE 4.20: The head height formed by the mill charge comprised of 6.0 mm diameter wooden beads and 5.50 mm diameter plastic beads as a function of the percentage of the critical speed

4.3.4 Wood, steel and plastic beads

In this scenario, the tumbling mill was filled with a mixture of wood, steel and plastic beads having diameters of 6.0 mm, 5.0 mm and 5.50 mm with an associated mass of 106.0 g, 1725.0 g and 114.0 g, respectively. This mixture of beads was subjected to a number of different rotation speeds. The mill charge fills the critical volume of the tumbling mill with a packing fraction of η = 0.535. The mill was set up as shown in Figure 4.4. The resulting fast neutron radiographs are presented in Figure 4.21.
Figure 4.21 shows the different phases formed by the mill charge, at different rotation speeds and when compared to Figure 4.5, the mill charge parameters for the case of the mixture of beads were measured.

The increasing rotation speed results in an increase in the total ball angle and average ball lift [81] of the tumbling mill which is presented in Figure 4.22. The angles presented in Figure 4.22 are normalised to the maximum angle measured during the experimental run while the power drawn by the stepper motor is normalised to the maximum power drawn in a single experimental run. This shows the relationship between the three parameters as a function of the percentage of the critical speed.

An intersection of the total ball angle and average ball lift occurs at 19.5% and 62.0% of the critical speed, shown in Figure 4.22. At this speed, Figure 4.22 also shows a lower power being drawn by the stepper motor to be at 62.0% which, for this mill charge, infers that this is the best rotation speed for comminution to occur. A determination of the regions and angles formed by the mill charge, as shown in Figure 4.5, was done and presented in Figure 4.23 and Figure 4.24.

Figure 4.23 shows the area of the rising region decrease with increasing rotational speed while the areas which promote comminution, the active and in-flight regions, increase in the area. Comparing this to the shoulder angles presented in Figure 4.24, the rotation speed for the best comminution for this mill charge is 62.0% of the critical speed.

The head height position is maximum at 62.0% of the critical speed, as shown in Figure 4.25, which relates to more of the mill charge moving into the in-flight region and is therefore the optimal rotation speed for the best comminution for this mill charge. The technique of fast neutron radiography provides useful quantitative information into the structure and dynamics of the mill charge. The important parameters of the mill charge namely the total ball angle, average ball lift, rising region, active region, in-flight region, shoulder and toe angles as well as the head height are determined, from which the optimal rotation speed for the best comminution is inferred. The ability to determine the optimal rotation speed for a specific mill design, is a key aspect of tumbling mills used in the grinding/crushing of ore within the mining sector. The optimal design saves in the cost of up-scaling the mill for full scale operation.

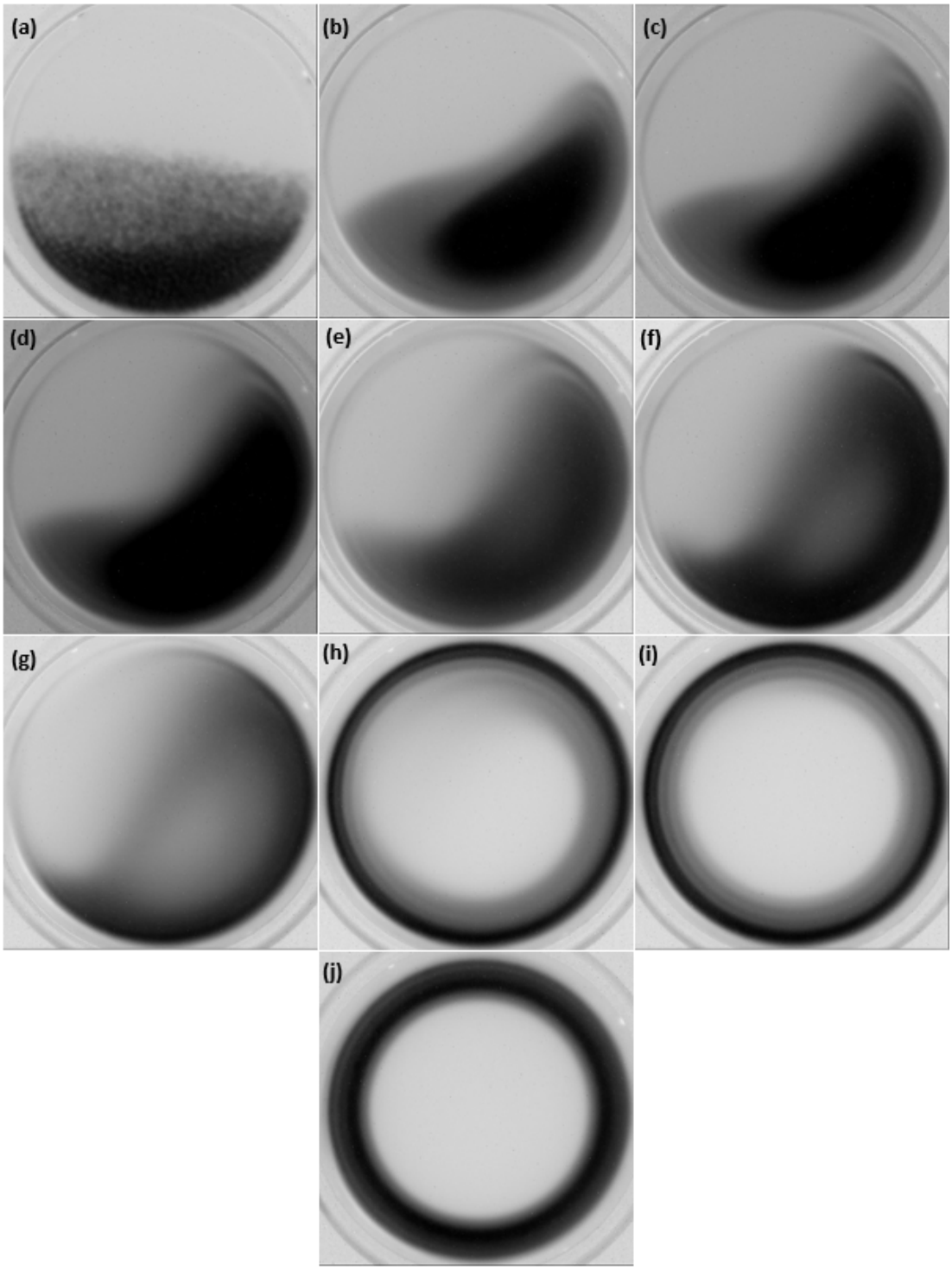

FIGURE 4.21: Fast neutron radiographs showing the phases formed by the mill charge comprised of 6.0 mm diameter wooden, 5.0 mm diameter steel and 5.50 mm diameter plastic beads, for different percentages of the critical speed with (a) rest, (b) 19.5% V_c, (c) 31.0% V_c, (d) 39.0% V_c, (e) 47.0% V_c, (f) 54.5% V_c, (g) 62.0% V_c, (h) 70.0% V_c,(i) 78.0% V_c and (j) 101.0% V_c

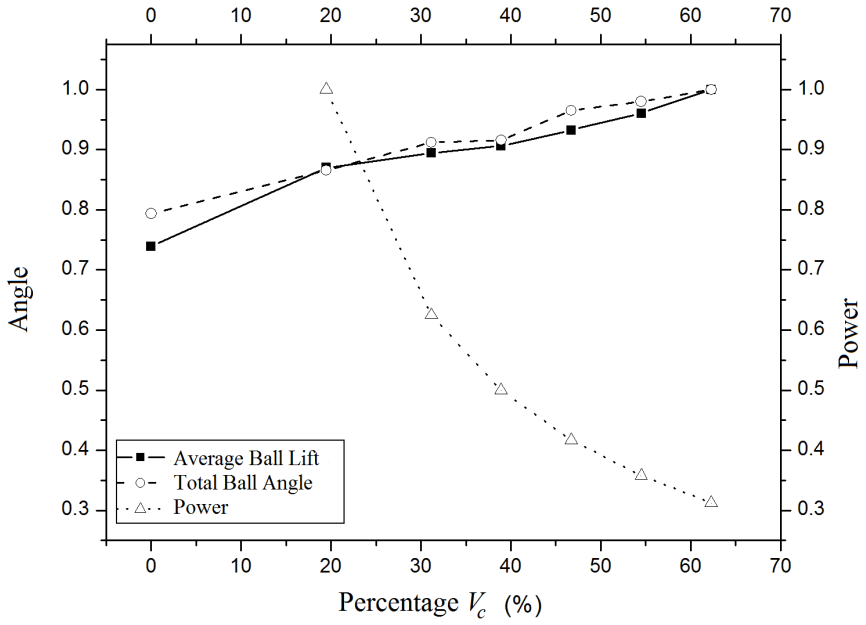

FIGURE 4.22: The total ball angle, average ball lift and power usage of the tumbling mill system with a mill charge comprised of 6.0 mm diameter wood beads, 5.0 mm diameter steel beads and 5.50 mm diameter plastic beads

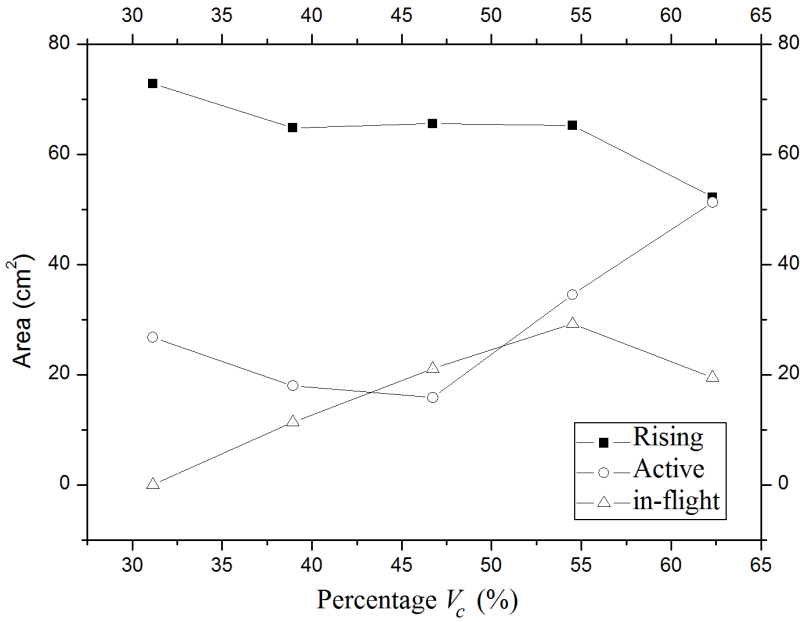

FIGURE 4.23: Area of regions formed by the mill charge comprised of a mixture of 6.0 mm diameter wooden beads, 5.0 mm diameter steel beads and 5.50 mm diameter plastic beads as a function of the percentage of the critical speed

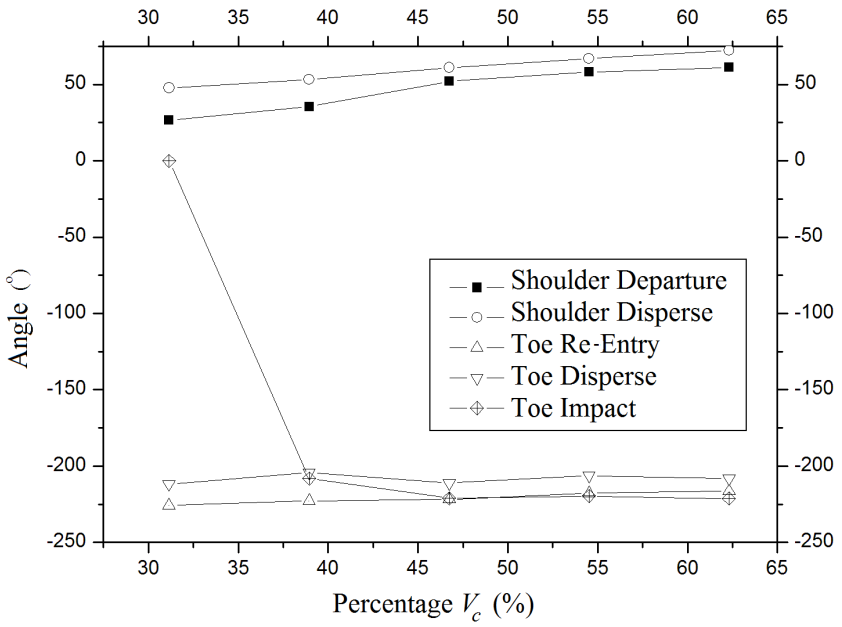

FIGURE 4.24: Angles formed by the mill charge comprised of a mixture of 6.0 mm diameter wooden beads, 5.0 mm diameter steel beads and 5.50 mm diameter plastic beads as a function of the percentage of the critical speed

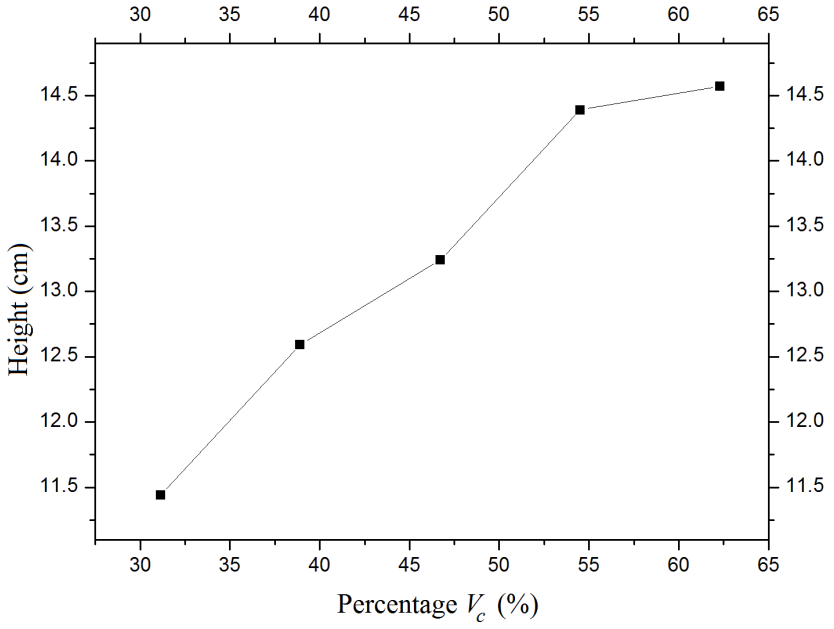

FIGURE 4.25: The head height formed by the mill charge comprised of 6.0 mm diameter wooden beads, 5.0 mm diameter steel beads and 5.50 mm diameter plastic beads as a function of the percentage of the critical speed

4.4 Fill factor of the mill charge within the tumbling mill

As fast neutrons travel through the mill charge and interact with the granular material, we are able to determine the shape of the mill charge using fast neutron radiography, as presented in Section 4.2. The fast neutrons are attenuated by the mill charge along their direction of propagation. The material used is comprised of wood, glass, plastic and steel, each of which have their own attenuation coefficient. These are calculated by employing the Beer-Lambert Law [82], Equation (4.5), to the transmission of fast neutrons through standard wood, glass, plastic and steel samples and is presented in Table 4.1.

$$I = I_0 exp(-\Sigma_i \mu_i x_i). \tag{4.5}$$

Equation (4.5) applies strictly to a mono-energetic incident neutron beam. When a broad energy neutron spectrum is used, the attenuation coefficient μ determined using this equation, represents an average value of μ weighted by the shape of the incident energy spectrum and is dependent on the sample thickness, x. If the thickness of the calibration standard is not drastically different from the thickness of the analysed sample, the error in μ introduced by the above effect is minimal.

For the wooden standard, the attenuation coefficient is calculated below, with I_{wood} being the transmission of the neutron beam through a wooden standard of thickness 4.0 cm and I_0 the transmission of the neutron beam with no wooden sample present. A similar process is done for glass, plastic and steel.

$$\begin{aligned}
\frac{I_{wood}}{I_0} &= \exp\left(-\mu_{wood} x\right) \\
\log\left(\frac{I_{wood}}{I_0}\right) &= -\mu_{wood} x \\
\mu_{wood} &= -\left(\frac{1}{x}\right) \log\left(\frac{I_{wood}}{I_0}\right) \\
\mu_{wood} &= -\left(\frac{1}{4.0}\right) \log\left(0.794\right) \\
&= 0.058 \text{ cm}^{-1}.
\end{aligned}$$

TABLE 4.1: Attenuation coefficient of beads making up the mill charge

Material	Attenuation Coefficient (cm^{-1})
Wood	0.058
Glass	0.048
Plastic	0.069
Steel	0.146

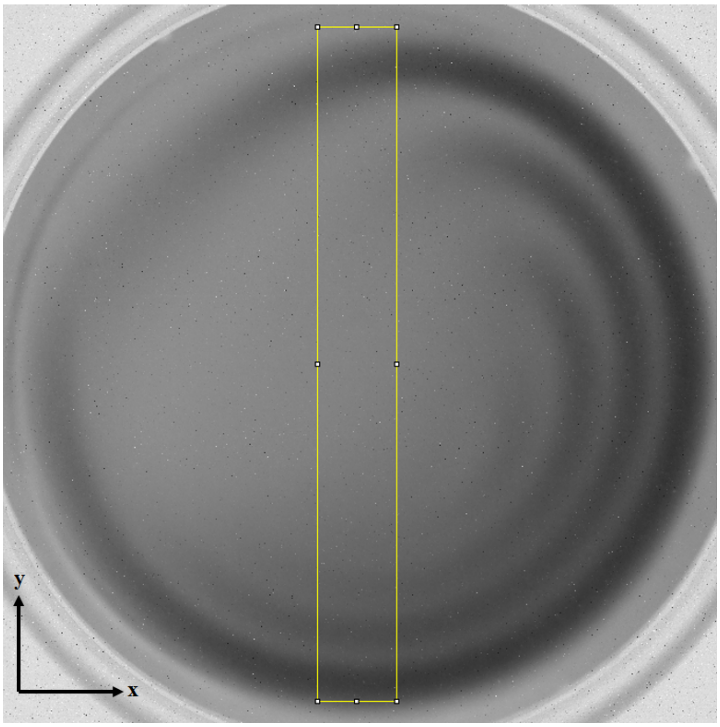

FIGURE 4.26: The region of interest used to calculate the length of the mill charge at different rotation speeds

The attenuation coefficient for wood, glass, plastic and steel presented in Table 4.1 is used to calculate the mixing of the mill charge. The fill factor of the mill charge that caused the attenuation of the fast neutrons, was calculated by using the standard attenuation coefficients presented in Table 4.1 and applied in Equation (4.5). Focus is placed on the region of interest shown in Figure 4.26, which is going through the centre of the mill charge for different rotation speeds. The fill factor of the mill charge is calculated through the region of interest and shown as a function of the y pixel range of the fast neutron radiograph.

The fill factor is calculated by changing the subject of Equation (4.5), which is shown in Equation (4.6) below,

$$x_i = -\frac{1}{\mu_i} \ln\left(\frac{I}{I_0}\right) \tag{4.6}$$

with i = wood, glass, plastic and steel and μ_i obtained from Table 4.1.

The I/I_0 is obtained from the fast neutron radiograph through the region of interest, shown in Figure 4.26, together with the attenuation coefficient, is used to calculate the fill factor, which is shown in the example for wood below,

$$\begin{aligned} x_{wood} &= -\frac{1}{0.0577}\log\left(\frac{I}{I_0}\right) \\ &= -\frac{1}{0.0577}\log\left(0.8112\right) \\ &= 3.63 \text{ cm}. \end{aligned}$$

This gives the fill factor for the wooden beads that causes the attenuation of the fast neutrons along their direction of propagation, through the region of interest, at a rotation speed of 47.0% of the critical speed. This is obtained using the radiograph presented in Figure 4.6(e). A case by case determination of the length of the mill charge follows.

4.4.1 Wooden beads

The mill was filled with 10.0 mm wooden beads as in Section 4.3.1. Figure 4.6 shows the phases formed by the mill charge at different rotation speeds. The cascade condition occurs at rotation speeds that are between 19.5% and 39.0% of the critical speed, cataracting occurs between 47.0% and 78.0% and the full centrifuge of the mill charge occurs beyond 80.0% of the critical speed. The fill factor of the mill charge through the region of interest, Figure 4.26, was determined for the rest, cascade, and full centrifuge conditions. The I/I_0 for the cascade condition was obtained by applying the region of interest defined in Figure 4.26 to the radiographs shown in Figure 4.6 and is presented as a function of the y pixel range in Figure 4.27.

In a similar way, the I/I_0 for the conditions of rest and full centrifuge were also obtained and presented separately in Figure 4.28.

Inserting the values of I/I_0 into Equation (4.6), the fill factor of the mill charge x_{wood} that attenuates the fast neutrons, was calculated and shown in Figure 4.29.

Figure 4.29 shows the fill factor of the mill charge for this mill configuration that attenuates the fast neutrons and how that factor changes with different rotation speeds. This also indicates the presence of 10 mm diameter wooden beads through the region of interest.

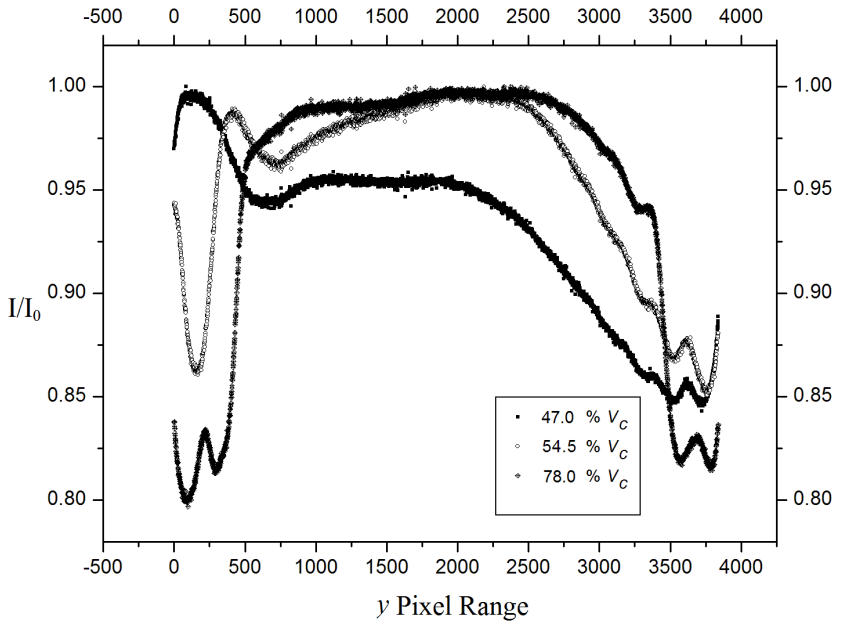

FIGURE 4.27: I/I_0 for the 10.0 mm diameter wooden beads making up the mill charge, through the defined region of interest, for speeds of 47.0%, 54.5% and 78.0% of the critical speed

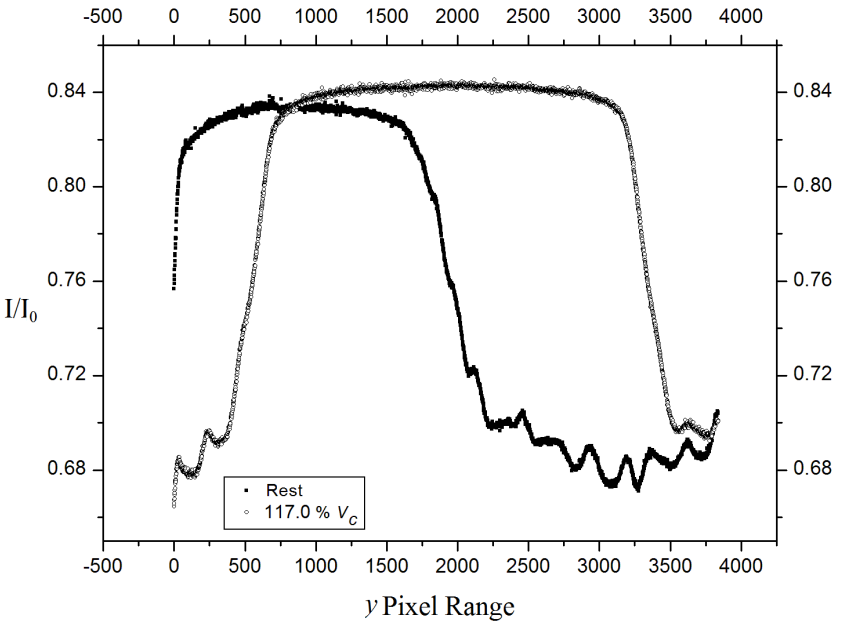

FIGURE 4.28: I/I_0 for the 10.0 mm diameter wooden beads making up the mill charge, through the defined region of interest, for the rest and full centrifuge condition

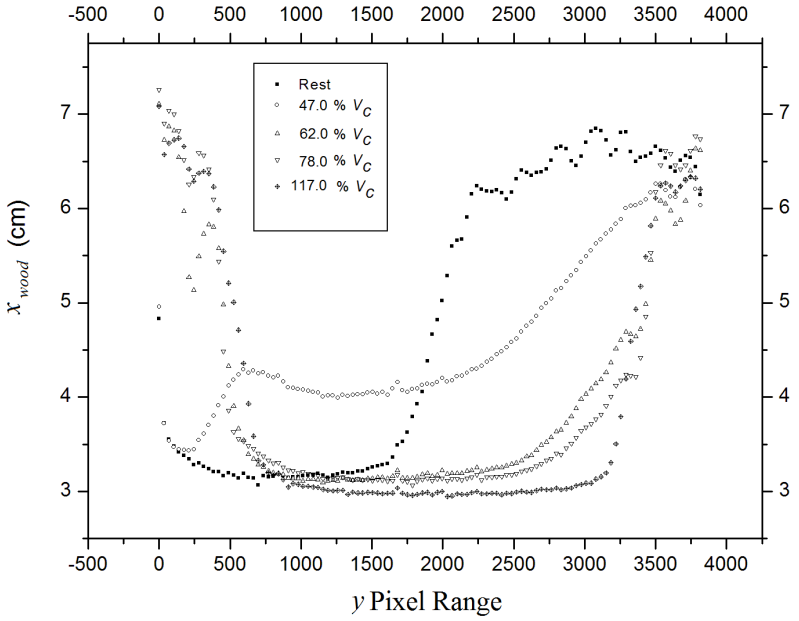

FIGURE 4.29: Fill factor of the mill charge, x_{wood}, that attenuates the fast neutrons at varying rotation speeds

4.4.2 Glass beads

The mill was filled with 6.0 mm, 8.0 mm and 12.0 mm glass beads as in Section 4.3.2. Figure 4.11 shows the phases formed by the mill charge at different rotation speeds. The cascade condition occurs at rotation speeds that are between 19.5% and 47.0% of the critical speed, cataracting occurs between 54.5% and 70.0% and the full centrifuge of the mill charge occurs beyond 71.0% of the critical speed. The fill factor of the mill charge through the region of interest, Figure 4.26, was determined for the rest, cascade, and full centrifuge conditions. The I/I_0 for the cascade condition was obtained by applying the region of interest defined in Figure 4.26 to the radiographs shown in Figure 4.11. It is presented as a function of the y pixel range in Figure 4.30.

In a similar way, the I/I_0 for the conditions of rest and full centrifuge was also obtained and presented separately in Figure 4.31.

Inserting the values of I/I_0 into Equation (4.6), the fill factor of the mill charge x_{glass} that attenuates the fast neutrons, was calculated and shown in Figure 4.32.

Similarly as done for the wooden beads above, Figure 4.32 shows the fill factor of the mill charge for this mill configuration, that attenuates the fast neutrons and how that factor changes with different rotation speeds.

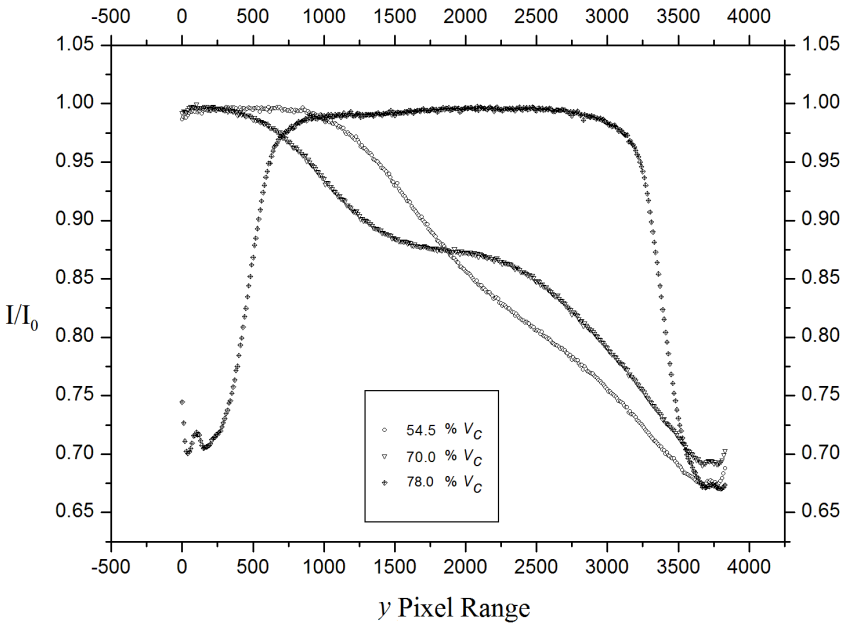

FIGURE 4.30: I/I_0 for the 6.0 mm, 8.0 mm and 12.0 mm diameter glass beads making up the mill charge, through the defined region of interest, for speeds of 54.5%, 70.0% and 78.0% of the critical speed

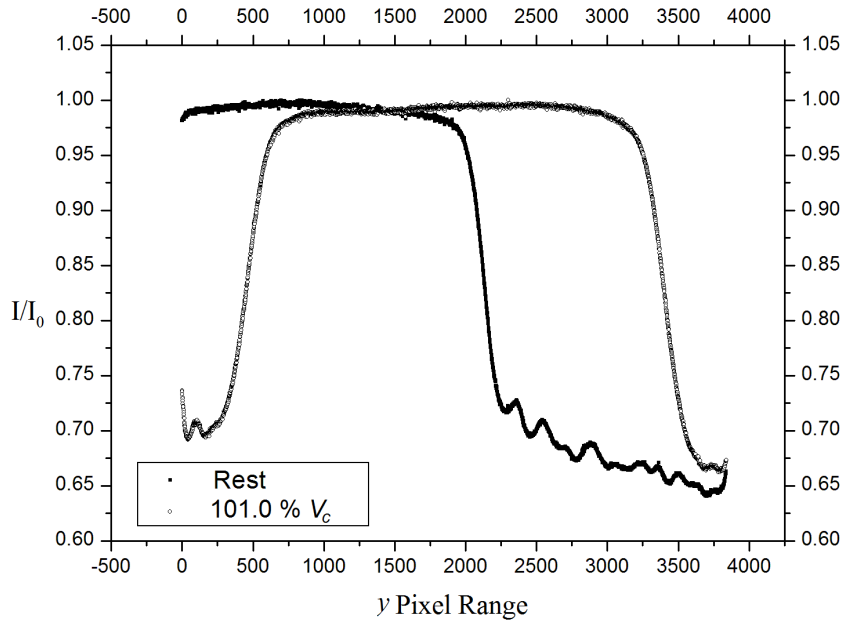

FIGURE 4.31: I/I_0 for the 6.0 mm, 8.0 mm and 12.0 mm diameter glass beads making up the mill charge, through the defined region of interest, for the rest and full centrifuge condition

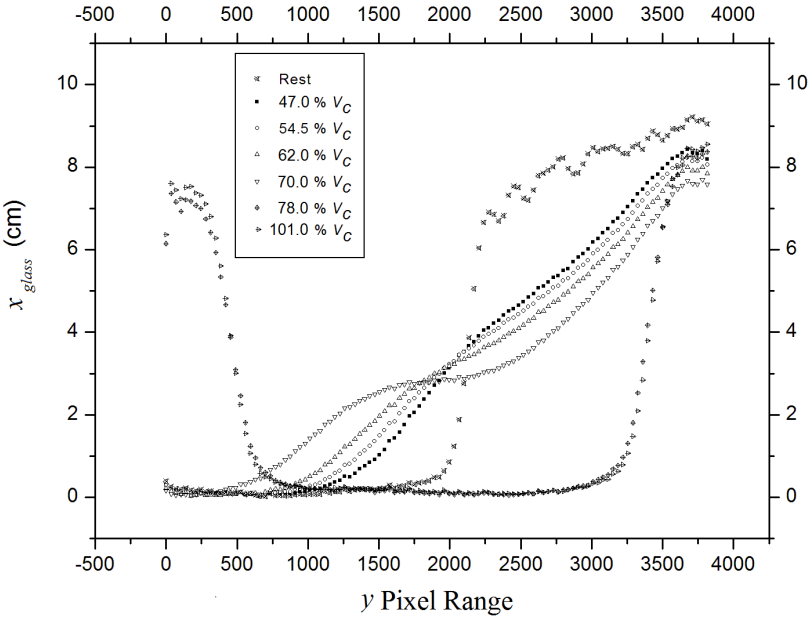

FIGURE 4.32: Fill factor of the mill charge, x_{glass}, that attenuates the fast neutrons at varying rotation speeds

4.4.3 Wood and plastic beads

The mill was filled with 6.0 mm diameter wood and 5.50 mm diameter plastic beads as in Section 4.3.3. Figure 4.16 shows the phases formed by the mill charge at different rotation speeds. The cascade condition occurs at rotation speeds that are between 19.5% and 39.0% of the critical speed, cataracting occurs between 47.0% and 78.0% and the full centrifuge of the mill charge occurs beyond 80.0% of the critical speed. The fill factor of the mill charge through the region of interest, Figure 4.26, was determined for the rest, cascade, and full centrifuge conditions. The I/I_0 for the cascade condition was obtained by applying the region of interest defined in Figure 4.26 to the radiographs shown in Figure 4.16. It is presented as a function of the y pixel range in Figure 4.33.

In a similar way, the I/I_0 for the conditions of rest and full centrifuge was also obtained and presented separately in Figure 4.34.

Inserting the values of I/I_0 into Equation (4.6), the fill factor of the mill charge $x_{wood/plastic}$ that attenuates the fast neutrons, was calculated and shown in Figure 4.35.

Figure 4.35 shows the fill factor of the mill charge for this mill configuration that attenuates the fast neutrons and how that factor changes with different rotation speeds. This also indicates the presence of the mill charge through the region of interest.

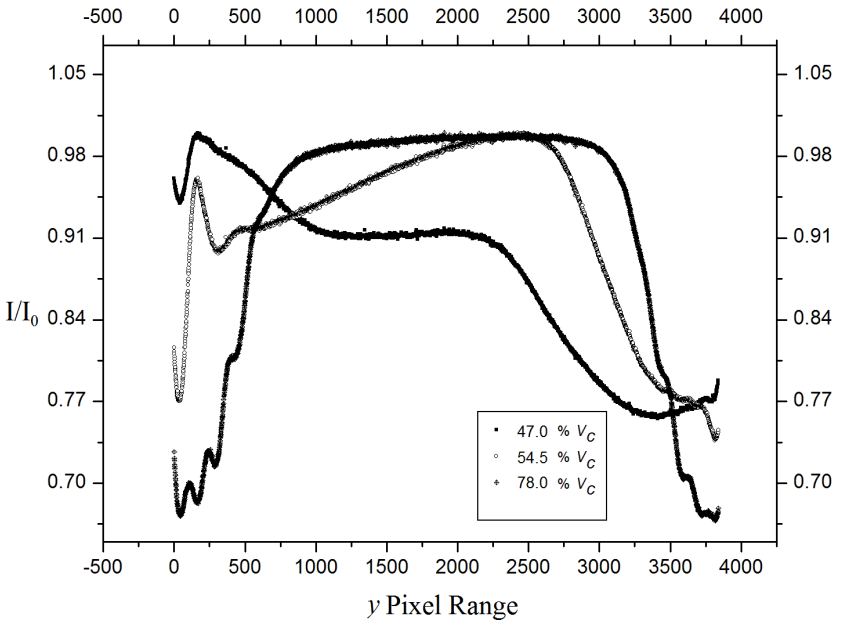

FIGURE 4.33: I/I_0 for the 6.0 mm diameter wooden beads and 5.50 mm diameter plastic beads, through the defined region of interest, for speeds of 47.0%, 54.5% and 78.0% of the critical speed

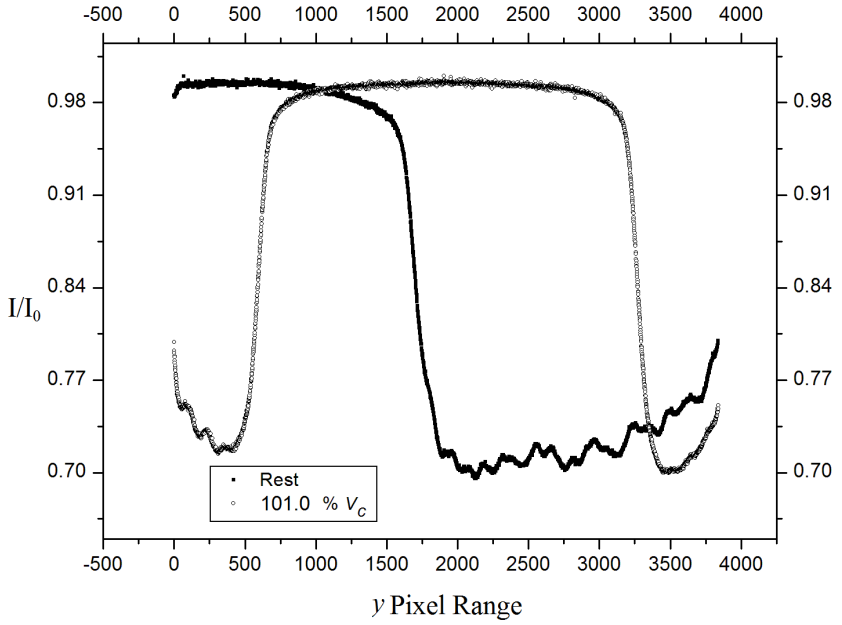

FIGURE 4.34: I/I_0 for the 6.0 mm diameter wooden beads and 5.50 mm diameter plastic beads making up the mill charge, through the defined region of interest, for the rest and full centrifuge condition

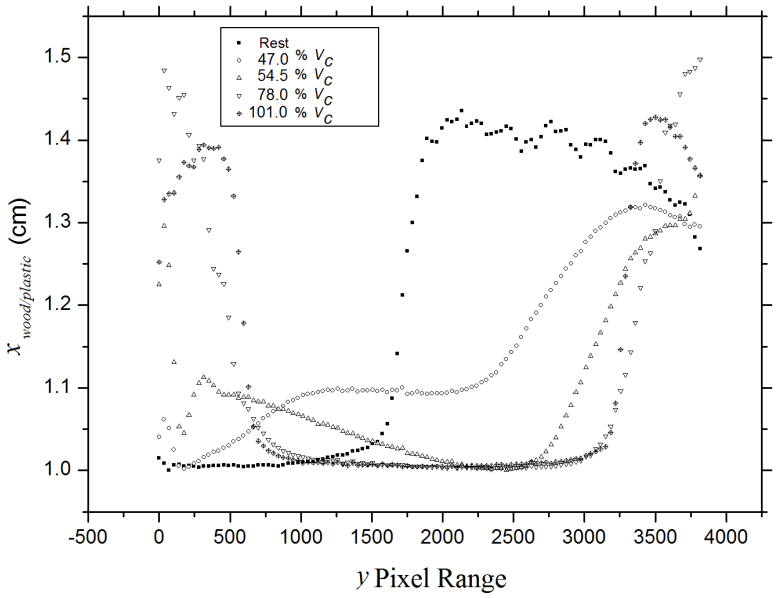

FIGURE 4.35: Fill factor of the mill charge, $x_{wood/plastic}$, that attenuates the fast neutrons at varying rotation speeds

4.4.4 Wood, steel and plastic beads

The mill was filled with 6.0 mm diameter wood, 5.0 mm diameter steel and 5.50 mm diameter plastic beads as in Section 4.3.4. Figure 4.21 shows the phases formed by the mill charge at different rotation speeds. The cascade condition occurs at rotation speeds that are between 19.5% and 39.0% of the critical speed, cataracting occurs between 47.0% and 78.0% and the full centrifuge of the mill charge occurs beyond 80.0% of the critical speed. The fill factor of the mill charge through the region of interest, Figure 4.26, was determined for the rest, cascade, and full centrifuge conditions. The I/I_0 for the cascade condition was obtained by applying the region of interest defined in Figure 4.26 to the radiographs shown in Figure 4.21. It is presented as a function of the y pixel range in Figure 4.36.

In a similar way, the I/I_0 for the conditions of rest and full centrifuge was also obtained and presented separately in Figure 4.37.

Inserting the values of I/I_0 into Equation (4.6), the fill factor of the mill charge $x_{wood/plastic/steel}$ that attenuates the fast neutrons, was calculated and shown in Figure 4.38.

Similarly as done for the other cases, Figure 4.38 shows the fill factor of the mill charge for this mill configuration that attenuates the fast neutrons and how that factor changes with different rotation speeds.

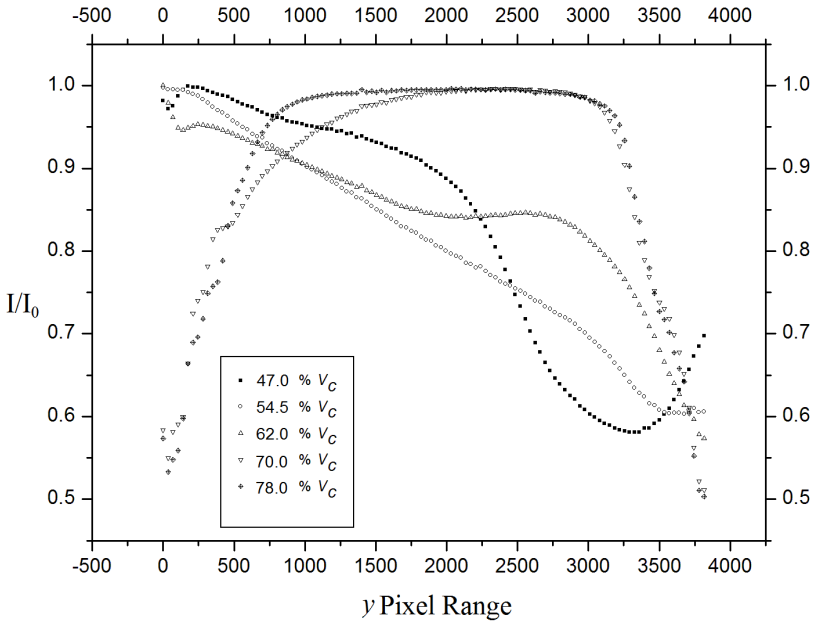

FIGURE 4.36: I/I_0 for the 6.0 mm diameter wooden beads, 5.0 mm steel beads and 5.50 mm diameter plastic beads, through the defined region of interest, for speeds of 47.0%, 54.5%, 62.0%, 70.0% and 78.0% of the critical speed

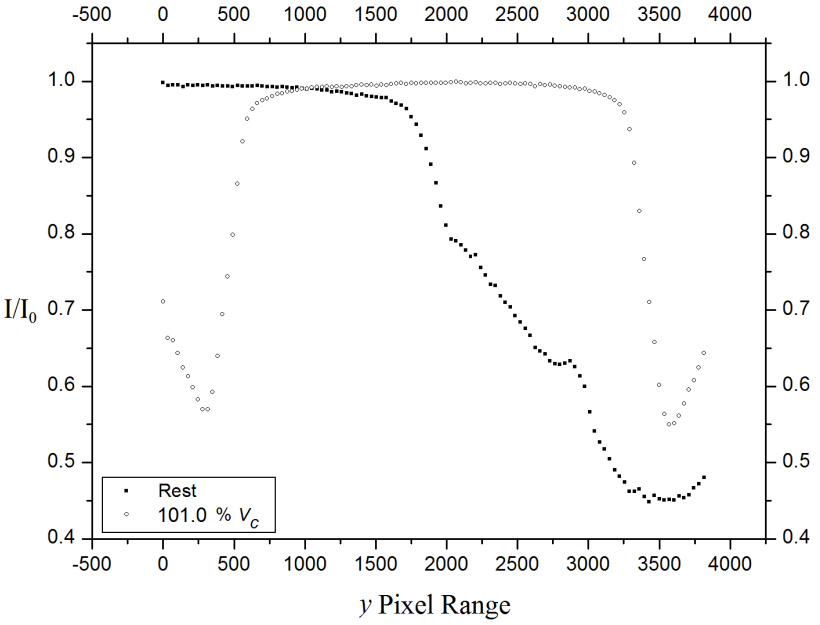

FIGURE 4.37: I/I_0 for the 6.0 mm diameter wooden beads, 5.0 mm diameter steel beads and 5.50 mm diameter plastic beads making up the mill charge, through the defined region of interest, for the rest and full centrifuge condition

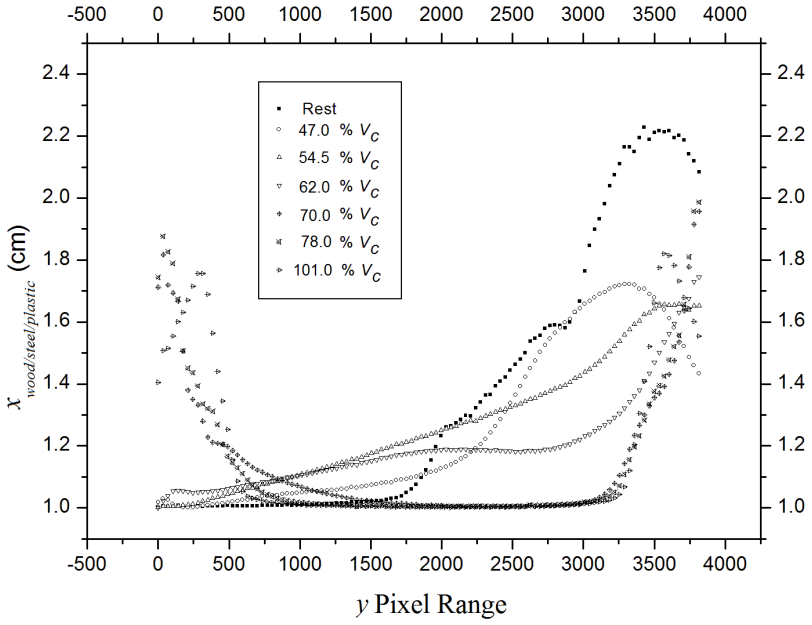

FIGURE 4.38: Fill factor of the mill charge, $x_{wood/plastic/steel}$, that attenuates the fast neutrons at varying rotation speeds

Fast neutron radiography can be used to infer the presence of the mill charge through the region of interest, which passes through the centre of the tumbling mill. This is of interest to assist in the building of mathematical models used to determine the flow of mill charge within the tumbling mill. The results observed through this region of interest show this as a complementary technique to PEPT, which cannot observe the movement of the mill charge through this region and is examined in the following chapter.

Chapter 5

Combining FNR with Positron Emission Particle Tracking (PEPT)

5.1 Introduction

Positron Emission Particle Tracking (PEPT) has developed into a useful technique for measuring the trajectory of a single tracer particle, moving within a system of granular or liquid flow or attached to a moving rigid body [83] [84] [85] [86] [87] [88]. The tracer is labelled with a radionuclide that decays via positron emission. The nearly collinear 511 keV annihilation gamma-rays are detected, in coincidence, by a modified Positron Emission Tomography (PET) camera. This coincidence detection defines their Line Of Response (LOR). The chronologically measured LORs may be used to triangulate the position of the moving tracer. In principle, only two LORs are necessary, but the recording of non-useful LORs from the detection of gamma-rays after undergoing Compton scattering between creation and detection and the coincident detection of two gamma-rays unassociated with the same annihilation event means that a larger number of measured LORs are required. However, up to 4.0 MHz of raw coincidence events can be processed by a PET camera, the tracking of particles moving as fast as 10.0 m s^{-1} may be realized. Velocities and accelerations are determined from measured position-time coordinates (t; x, y, z) via an interpolation and differentiation algorithm [86] [89] [90]. Other parameters, such as occupancy, residence time, mixing indices, diffusion constants, vorticity and porosity are also routinely determined from the measured coordinates.

PEPT was formally postulated in the early 1990s by a group at the University of Birmingham [83] [84] [85]. PEPT Cape Town [91] became the second operational PEPT facility in the world in 2009, after the Positron Imaging Centre at the University of Birmingham. The laboratories of PEPT Cape Town [91] are situated at iThemba LABS (Laboratory for Accelerator-Based Sciences) in Cape Town, South Africa. This is a national laboratory that operates a number of accelerators, including a k = 200 separated-sector cyclotron. The cyclotron facility routinely produces light and heavy particle beams for nuclear physics research and radioisotope production. The PEPT Cape Town laboratories house the ECAT EXACT3D HR++ (Model: CTI/Siemens 966)

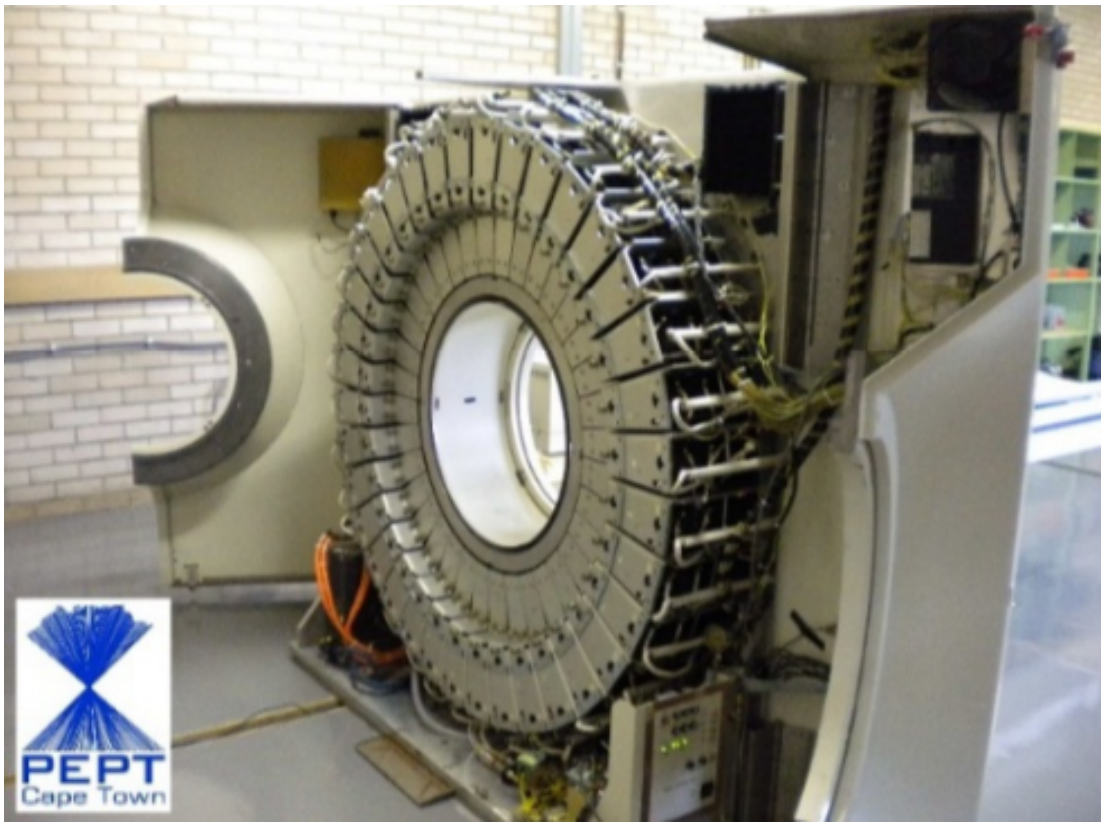

FIGURE 5.1: The ECAT EXACT3D HR++ PET scanner at PEPT Cape Town, which has been adapted for PEPT

PET camera, shown in Figure 5.1, and a number of smaller PET systems. The PET scanner was designed to achieve high resolution and high sensitivity for PET-based research [92]. The camera consists of 27 000 detector elements with a ring diameter of 82.0 cm, producing a 23.40 cm axial field of view. The data-acquisition system can maintain a maximum acquisition rate of about four million coincidence events per second, with a much higher data-acquisition rate possible, in short bursts [92].

Over the last decade, a wide range of PEPT applications has been explored, both at the Positron Imaging Centre and PEPT Cape Town, in particular: powder mixing [93], particle and fluid behaviour in granular beds [94] [95], fluidization phenomena [96] [97], rotating drums [98] [99] and minerals processing [100] [101] [102]. Data are recorded chronologically, where each coincidence event is written to a circular buffer that is written to disk as a list-mode stream every half buffer, describing the two detector elements in the ring that give rise to each LOR and a time-stamp accurate to one millisecond per event, with the coincidence timing having a 1.0 ns resolution. Data representing a single LOR contains 32 bits of information. To represent the LORs in software, each event is de-constructed into Cartesian coordinates describing position and time for each LOR. The analysis of list-mode data from a PEPT run begins with slicing a series of chronological coincidence events (recorded LORs) into equal groups of events N. For a chosen N, the uncertainty scales as $1/\sqrt{N}$ and therefore a larger N

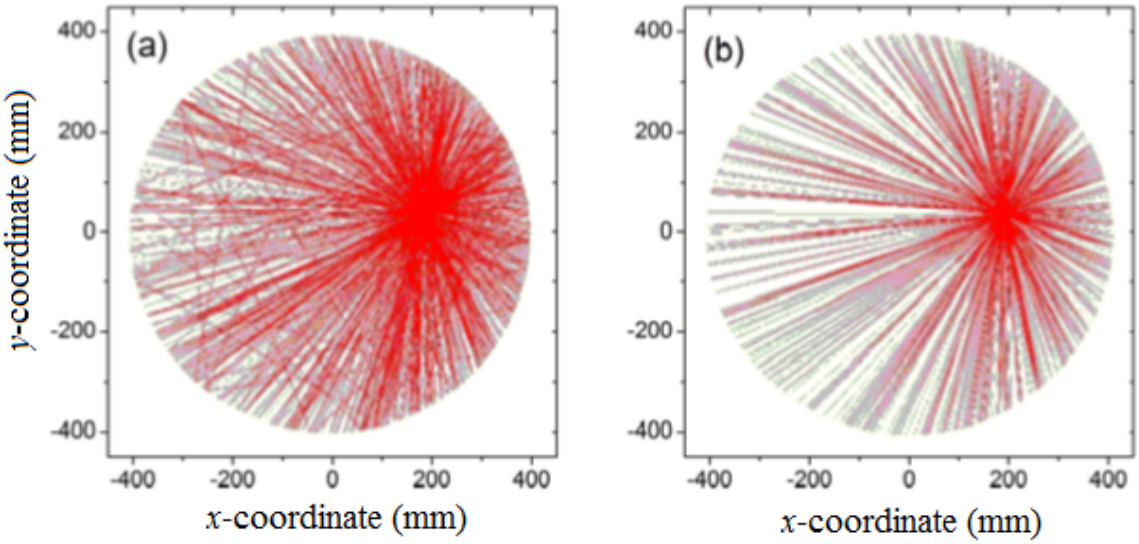

FIGURE 5.2: An axial projection of one thousand lines of response measured in about one second by the ECAT EXACT3D HR++ PET scanner (a) before and (b) after application of the PEPT algorithm

gives a higher precision. The ctrack algorithm is used to determine the location of the tracer and is based on the premise that for a given N, all uncorrupted LORs should ideally intersect at a single point in space, i.e. the location of the tracer [83]. In practice, LORs typically do not all intersect, for a variety of reasons (some are caused by the effect of Compton Scattering); thus, the approach is to find the point in space that minimizes the sum of the perpendicular distances to the LORs. Since a proportion of the LORs are corrupted by one or both of the coincident gamma-rays undergoing Compton scattering before detection, or by the detection of uncorrelated gamma-rays in coincidence, the algorithm must disregard these events and determine the location from a set of uncorrupted LORs. The current implementation of the algorithm requires the specification of the set size N, the percentage f of N LORs to use in the triangulation of each location and a maximum acceptable uncertainty for the final solution [83]. The choice of N and f depend on the total LORs recorded in the run and the proportion that have been corrupted. An acceptable range for f in practice is between 40% to 50%. The ctrack algorithm is used to obtain the final solution [83] [88] [89].

As an illustration, Figure 5.2 shows an axial projection of roughly 1 000 LORs measured in about one second by the ECAT EXACT3D HR++ PET scanner, before and after application of the triangulation algorithm, which has to be optimized for f, to diminish the contribution resulting from Compton effects and non coincidental gamma-rays.

As an example, PEPT measurements of a tracer tumbling inside a small rotating drum of internal diameter 7.0 cm and volume of 1.0 l, filled with glass beads of diameter 5.0 mm are shown in Figure 5.3. The left panel shows a few thousand coordinates

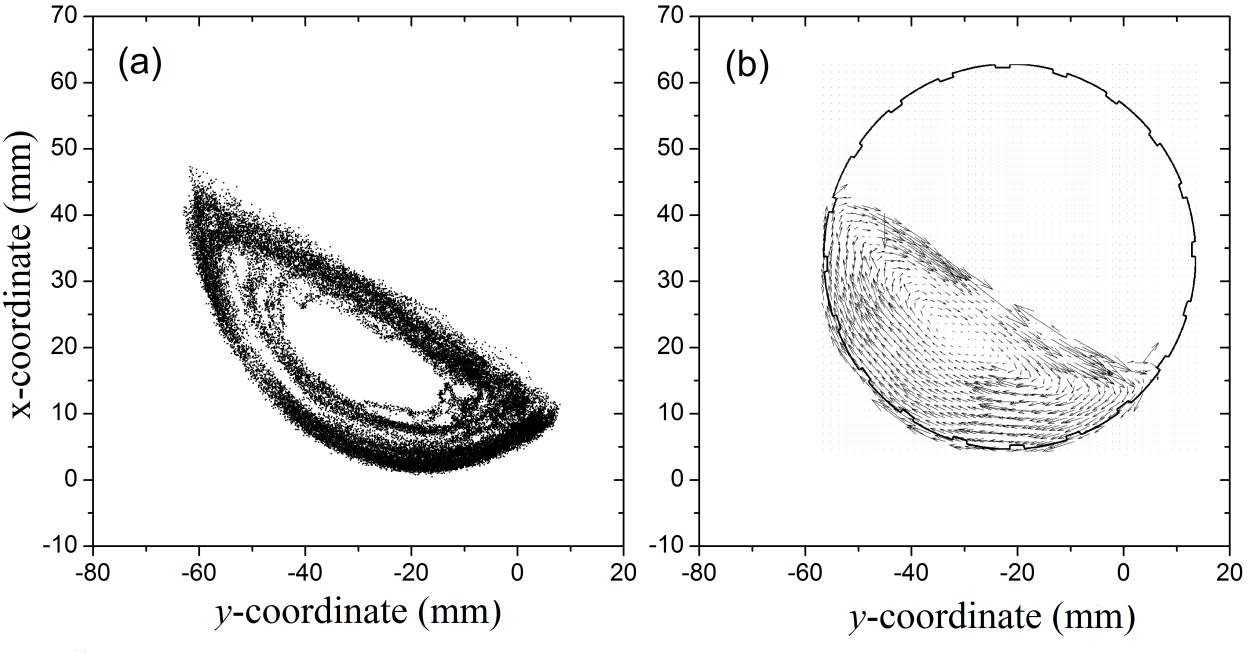

FIGURE 5.3: An example of a PEPT measurement of (a) a few thousand locations (z-axis projection) of a tracer moving within a small rotating drum filled with glass beads of diameter 5.0 mm; and (b) the average velocity field determined for the tumbling tracer

measured with a frequency of a few kHz, axially projected onto the x-y plane, and the right panel, the axially projected average velocity field determined for voxels of volume 2.0 $\times$ 2.0 $\times$ 2.0 mm^3. This figure presents the velocity field, which is shown by the arrows in the right panel of Figure 5.3. It is meant to show the axially projected average velocity field determined for voxels.

In PEPT studies, it is usually important for the shape and composition of the tracer to be as similar as possible to the material represented. Furthermore, the activity of the tracer must be such that sufficient LORs are recorded per second to produce a measurement of the trajectory of the tracer with a high location frequency and minimal uncertainty, as the PEPT technique is widely open to accept all combinations in the ring scan making it a 3D PEPT image. There is often a trade-off between tracer activity and physical characteristics. A large number of positron-emitting radioisotopes, with half-lives ranging from minutes to years, are in principle suitable for PEPT tracers. However, since it is frequently unrealistic to recover a tracer particle from the bulk of the liquid or powder under study, the half-life ($t_{\frac{1}{2}}$) of the radioisotope should ideally be long enough to enable tracking over a practical experimental timescale but short enough for the tracer to be discarded as radioactive waste after use. Radioisotopes commonly used for PEPT experiments are ^{68}Ga ($t_{\frac{1}{2}}$ = 68 minutes) and ^{18}F ($t_{\frac{1}{2}}$ = 109 minutes). ^{22}Na ($t_{\frac{1}{2}}$ = 2.6 years) is often useful in experiments where the tracer can definitely be recovered or for calibration.

A number of different techniques are used for the production of tracers. The method used worked on the principle of drill and fill. Larger tracers are manufactured at the PEPT facility at iThemba-LABS by absorbing ^{68}Ga into a small resin bead, which is then inserted into the active material by micro-drilling into the particle and then backfilling and sealing the aperture with a resin [72]. The activity with which a tracer particle may be labelled depends strongly on its size and composition. For typical PEPT applications, it has been found that tracer activity must be between 10 to 40 MBq (about 300 to 1000 μCi). In the absence of significant scattering and absorbing material in the system under study, the number of measured LORs per second is directly proportional to the activity with which the tracer is labelled [103]. However, the system under study often presents a scattering environment that is dynamically changing with respect to the location of the tracer within the system, which can add complexity to the tracking analyses.

In this chapter the PEPT technique is applied to the tumbling mill experiment, when the mill charge is filled with 10.0 mm wooden beads and a mixture of 6.0 mm, 8.0 mm and 12.0 mm glass beads. The results achieved using PEPT are compared to those obtained when using FNR.

5.2 Experiment

The tumbling mill apparatus was positioned axially at the centre of the field of view of the ECAT EXACT3D HR++ PET scanner, as shown in Figure 5.4, providing a stable platform onto which the mill can rotate. ^{68}Ga was embedded into a 10.0 mm wooden bead, an 8.0 mm glass bead and a 12.0 mm glass bead and used as tracers for the studies. Each type of bead has a hole through the centre in which a drop of ^{68}Ga solution was inserted with a pipette, allowed to evaporate, and sealed with resin. The initial activities ranged from 1.20 mCi to 2.0 mCi. The mill rotation speed was set at 39.0% of the critical speed V_c(with an approximate total of 20448 revolutions for the entire acquisition period), for the tumbling mill filled with wooden beads and 31.0% V_c for the tumbling mill filled with a mixture of glass beads (with an approximate total of 16368 revolutions for the entire period). The chosen speeds induce the interim cascade/cataracting phase formed by that mill charge, as highlighted in Chapter 4. To prevent the tracer from getting trapped in a specific region, the rotation of the tumbling mill is paused and the mill charge re-mixed before the collection of PEPT data resumes. This is done every 15 minutes to increase the probability that the tracer will visit every location of the rotating mill charge. PEPT data was acquired for eight hours a day, per tracer per mill charge, with the number of recorded events diminishing over the eight hours, as the tracer activity reduces. After LOR reduction, the processed data was analysed and plotted using python based routines available at PEPT CT.

FIGURE 5.4: Experimental setup at PEPT Cape Town with the rollers and mill set in the middle of the ECAT EXACT3D HR++ PET Scanner

5.3 Results

The results obtained using the PEPT technique are presented here, for 10 mm wooden beads and a mixture of glass beads. These are also compared to the results from the fast neutron radiography study.

5.3.1 Optimization

Prior to the tumbling experiment a ^{22}Na stationary tracer was placed in the centre of the PET scanner and used to determine the best N and f values for the current experimental configuration [92], with each event defined with a global clock of frequency 1.0 kHz and a temporal resolution of 1.0 ms. The optimal values of N and f are obtained when the uncertainty from the LOR reduction for the ^{22}Na stationary tracer, using the ctrack algorithm, is minimized. Various N and f values were examined with the results presented in Figure 5.5. A larger N requires a greater time to perform the LOR reduction, therefore the optimal value of N for this experimental configuration was chosen to be 500, as its uncertainty is comparable to when N is 750 (The 22% discrepancy between N=500 and N=750 in relation to each other, Figure 5.5, covers a range of 0.45 mm to 0.55 mm in the position for the stationary ^{22}Na source. However, in the PEPT rotating mill data, the range this is applied to covers 120.0 mm x 120.0 mm from which the contribution of each error, to the overall data, is between 0.38% and 0.45%. These both fall in the acceptable range, with N=500 taken to accommodate for the aforementioned minimizing of time in LOR reduction). The optimal f is 45% with these optimal values used to perform the LOR reduction for the tracer in the 10.0 mm wooden beads, during rotation.

The best N and f values for the mixture of 6.0 mm, 8.0 mm and 12.0 mm glass beads were obtained in the same manner. Various N and f values were examined and presented in Figure 5.6 from which the optimal conditions were chosen as N = 500 and f = 35% for the 8.0 mm glass bead tracer, Figure 5.6(a). For the 12.0 mm glass bead tracer, the optimal values chosen were N = 500 and f = 45%, Figure 5.6(b). These optimal N and f values were used to perform the LOR reduction for the data acquired using the 8.0 mm glass bead tracer and the 12.0 mm glass bead tracer.

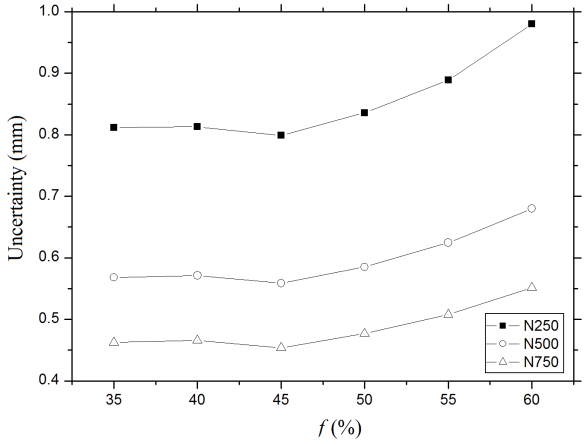

FIGURE 5.5: Uncertainties in the LOR reduction as a function of f and N, measured for a stationary tracer positioned near the centre of the ECAT EXACT3D HR++ scanner for the 10.0 mm wooden tracer

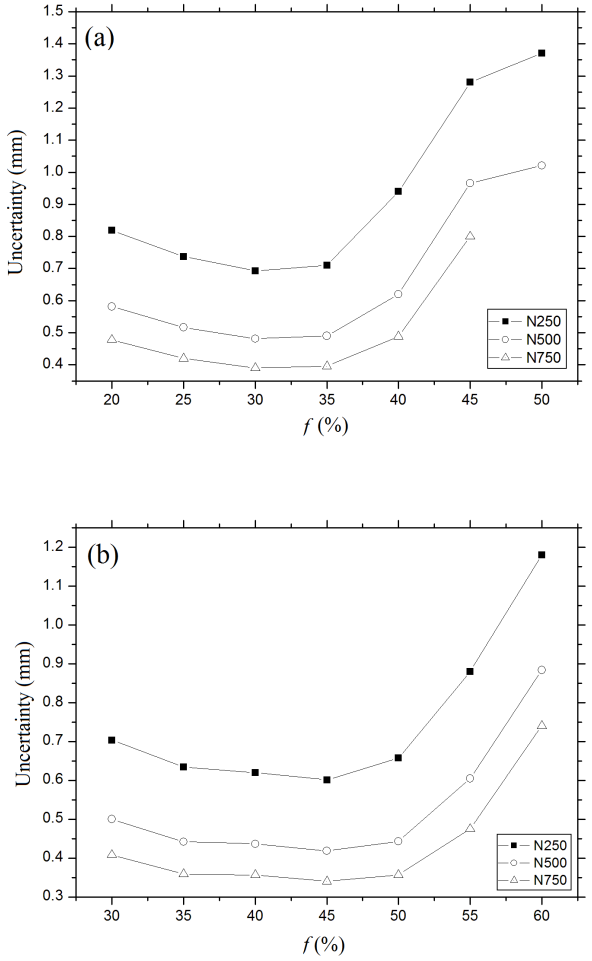

FIGURE 5.6: Uncertainties in the LOR reduction as a function of f and N, measured for a stationary tracer positioned near the centre of the ECAT EXACT3D HR++ PET scanner for (a) 8.0 mm glass tracer and (b) 12.0 mm glass tracer

5.3.2 Wooden beads

The tumbling mill was filled with 230.0 g of 10.0 mm diameter wooden beads. ^{68}Ga, with an activity of 2.0 mCi, was embedded into one of the wooden beads and sealed using resin. This bead acts as the tracer and was added to the wooden beads making up the mill charge. The mill was placed on rollers, as shown in Figure 5.4, and rotated at a constant speed of 39.0% of the critical speed.

The PET camera records the tracer location, over time, in the x, y and z direction for the duration of the experiment. Following the reduction and processing of the LORs, occupancy plots showing the xy projection and zy projection were obtained and represent the shape of the mill charge during this constant rotation speed, showing the achieved steady state of dynamic flow within the tumbling mill system. The xy projection is shown in Figure 5.7(a) which is obtained by mapping the 3D radial PEPT measurements onto a 2D Cartesian grid. This process causes the effect of pixelation in the 2D projection image. The blank pixels (areas) are a result of no significant data above a statistical threshold. The dark blue region represents a lower occupancy as the tracer passed through that specific location at a lower frequency for the duration of the experiment. The red region represents a higher occupancy as the tracer passed through that location with a higher frequency for the duration of the experiment. The shape of the mill charge is observed in Figure 5.7(a), and this shows that tracking the single tracer particle can be used to derive the shape formed by the mill charge, for the duration of the experiment. The xy projection is compared to the fast neutron radiograph taken at the same rotation speed and is shown in Figure 5.7(b), this being the xy projection.

Figure 5.7 shows an agreement between the shape of the mill charge obtained when using PEPT to that using FNR. Each technique shows the formation of layers as the steady state of dynamic flow is achieved within the mill. From the shape of the mill charge during rotation, the optimal parameters for the best grinding conditions can be calculated using PEPT, as conducted in Chapter 4 using FNR. The agreement in the shape of the mill charge, presented by PEPT and FNR, assists in verifying and understanding the movement of the mill charge when rotating. In Figure 5.7(a), the PEPT occupancy xy projection shows a higher presence of the tracer at the centre locations of the tumbling mill, during the tumbling phase, which is the active region of the mill charge. The increased occupancy of the tracer at the centre can be used to infer a uniform distribution of 10.0 mm wooden beads through the centre of the mill during rotation. However, the FNR measurement shows this as a less dense region, which is highlighted in Figure 4.29. To confirm this, the zy projection was examined and is shown in Figure 5.8. PEPT records data in three dimensions and therefore allows the examination of different projects under the same running conditions and from the same file, a capability that is not present in FNR.

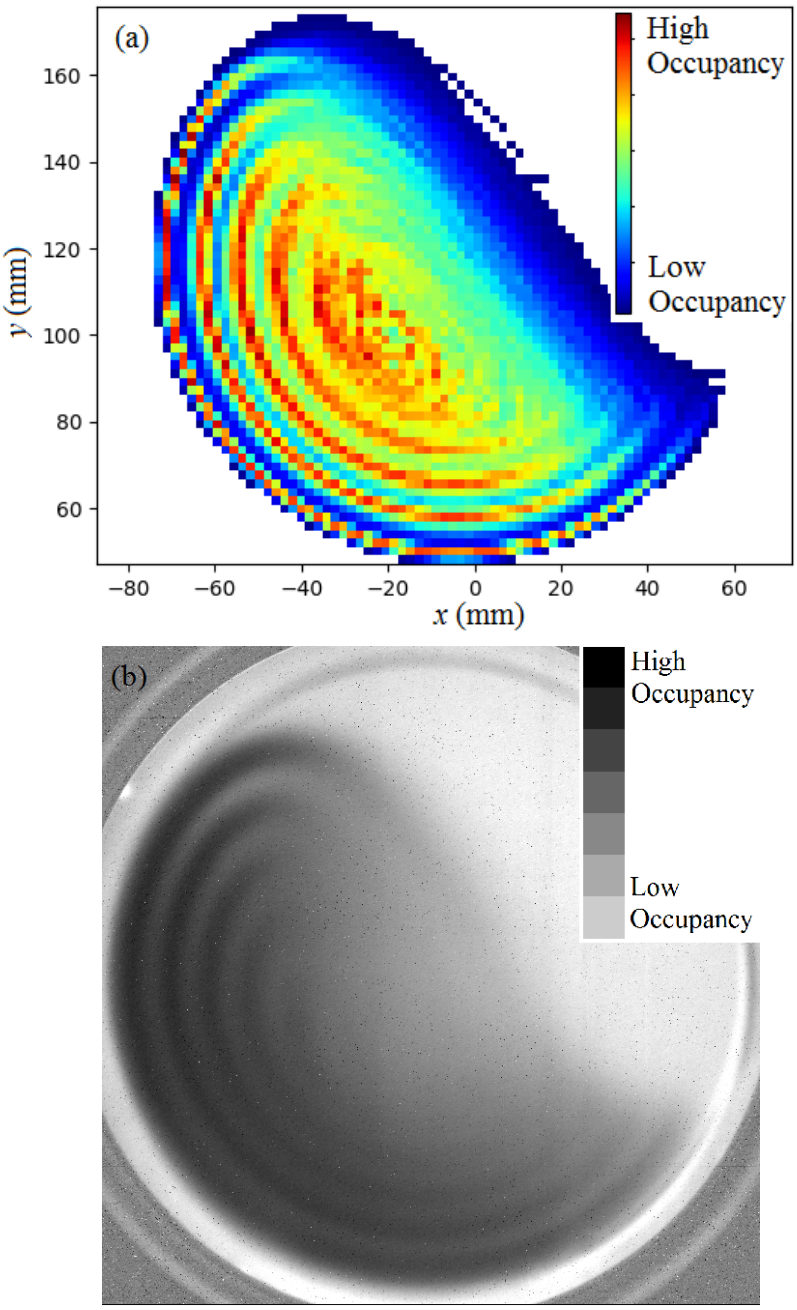

FIGURE 5.7: Results for the 10.0 mm wooden beads, showing (a) the PEPT occupancy *xy* projection and (b) the associated fast neutron radiograph for the same rotation speed

Figure 5.8 shows that the tracer visits, at a higher frequency, the areas at the edges of the *zy* projection and is not uniformly distributed through the centre of the mill which supports Figure 5.7(b), which shows a lower occupancy through the centre of the mill.

As PEPT chronologically records the locations of the tracer during rotation, the speed at which the tracer moves was also calculated. The three dimensional speed of the tracer in the two dimensional *xy* projection is presented in Figure 5.9. The speed data is related to the specific regions formed within the mill charge as described in Chapter 4 and is shown in Figure 5.9.

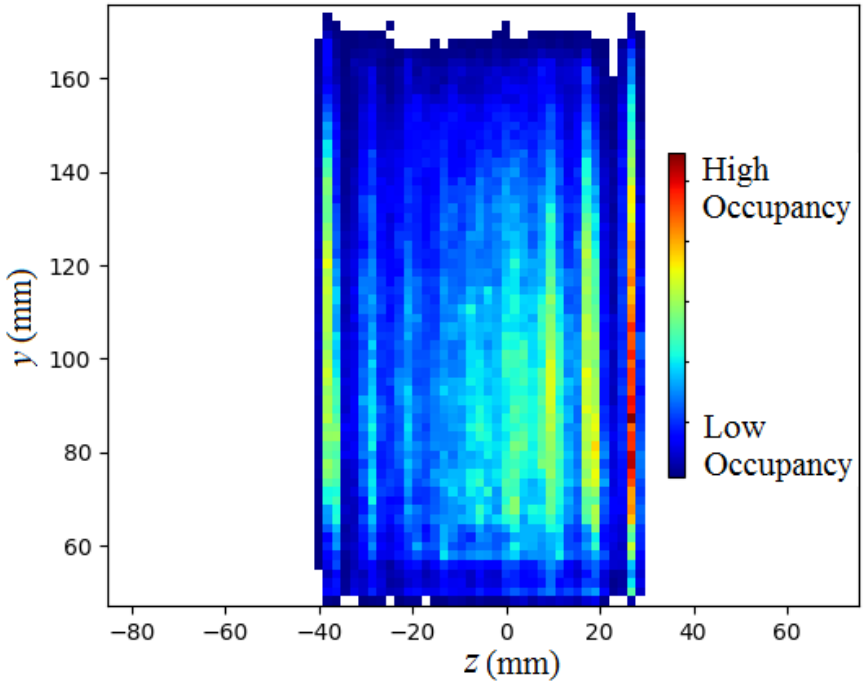

FIGURE 5.8: PEPT occupancy *zy* projection for the 10.0 mm wooden beads in the mill charge, during rotation

In Figure 5.9 the blue regions represent the tracer moving slower at that location, when compared to the tracer moving faster in the red regions. The blue region forms the majority of the mill charge at this rotation speed and is a part of the rising region of the mill charge, which is related to Figure 4.8 in Chapter 4. The number of beads present in the rising region will become the source of beads that will eventually feed into the active region. The faster moving red region is the active region and is the region that promotes a more active comminution of the mill charge. The faster beads have higher speed when falling into the impacted toe which is shown by the high speed region on the cascade surface of the mill charge. This also contributes to better comminution. The speed data obtained from the PEPT technique shows the different

regions formed in the mill charge, which is a result of its rotation, which is also confirmed in the average velocity field shown in Figure 5.10.

The time average velocity field, Figure 5.10, shows the movement of the mill charge for each specific region and also the speed at which the tracer moves within the region, re-affirming the data given by occupancy and speed, where it is observed that the rising region feeds into the active region.

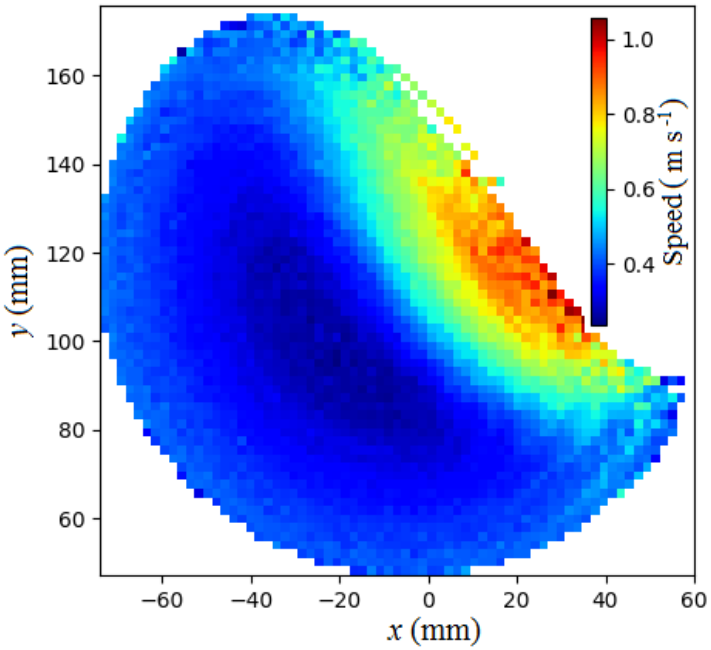

FIGURE 5.9: Speed of the tracer in the *xy* projection for a mill charge comprised of 10.0 mm wooden beads

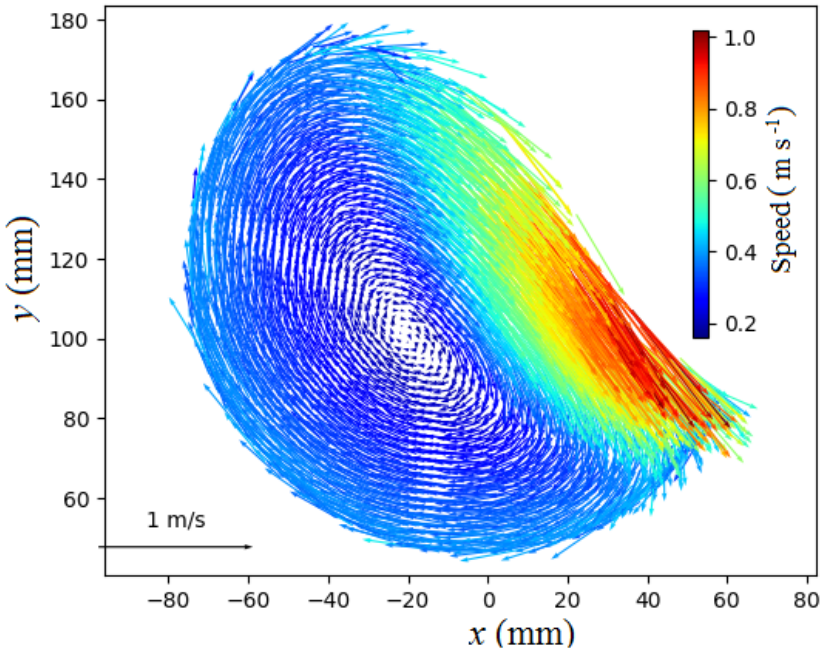

FIGURE 5.10: The average velocity field in the *xy* projection for a mill charge comprised of 10.0 mm wooden beads

5.3.3 Glass beads

The tumbling mill was filled with glass beads having the characteristics presented in Table 5.1. For the first case ^{68}Ga, with an activity of 1.20 mCi, was embedded into a 8.0 mm glass bead and sealed with resin to make the tracer, followed by a second tracer which was made by embedding ^{68}Ga, with an activity of 1.20 mCi, into a 12.0 mm glass bead, sealed with resin. The LORs from this tracer were chronologically recorded and analysed, as done for the 10.0 mm wood case.

The mill rotated at a constant speed of 31.0% of the critical speed. The PEPT occupancy *xy* projection is presented in Figure 5.11, with Figure 5.11(a) showing the occupancy given by the 8.0 mm glass tracer and the behaviour of the 8.0 mm glass

TABLE 5.1: Characteristics of glass beads used to perform the PEPT experiments

Bead diameter (mm)	Mass (g)
6.0	275.0
8.0	293.0
12.0	334.0

beads on average. Figure 5.11(b) shows the occupancy given by the 12.0 mm glass tracer and the behaviour of the 12.0 mm glass beads on average.

The recorded tracer location over the duration of the experiment shows the shape of the mill charge during rotation, Figure 5.11, with the pixelation and empty spaces occuring as in the 10.0 mm wooden bead tracer scenario. The shape achieved using PEPT is compared to the FNR image, Figure 5.11(c). Figure 5.11(a) shows the tracer visiting the centre of the mill charge more frequently than the other regions as opposed to Figure 5.11(b) which shows the tracer avoiding the centre. The FNR in Figure 5.11(c) cannot distinguish between bead sizes in this way. The comparison shows that both techniques observe the formation of layers and the achieved steady state of dynamic flow during rotation, from which the optimal conditions for grinding can be calculated, as was done in Chapter 4. FNR is dependent on the attenuation of the fast neutrons by the glass beads from which conclusions can be drawn on the overall density distribution of the glass mill charge, but FNR cannot distinguish between bead sizes.

From this observation it is concluded that the different regions of the mill charge are occupied more frequently by beads with specific diameters, i.e. smaller beads collect at the centre and larger beads move to the outer regions of the mill charge during rotation. Therefore the PEPT can selectively study a specific species of particle or phase of material that forms a part of a composite mixture.

The occupancy *xy* projection, for the 8.0 mm glass tracer, shows a higher frequency of occurrence of the tracer through the centre locations of the mill charge. This is confirmed by examining the occupancy *zy* projection, Figure 5.12(a), which also shows the occupancy of the 8.0 mm glass tracer occurring more frequently through the centre of the mill charge during rotation. For the 12.0 mm glass tracer the occupancy *zy* projection, Figure 5.12(b), shows the tracer having a higher frequency of occurrence along the outer layers of the mill charge.

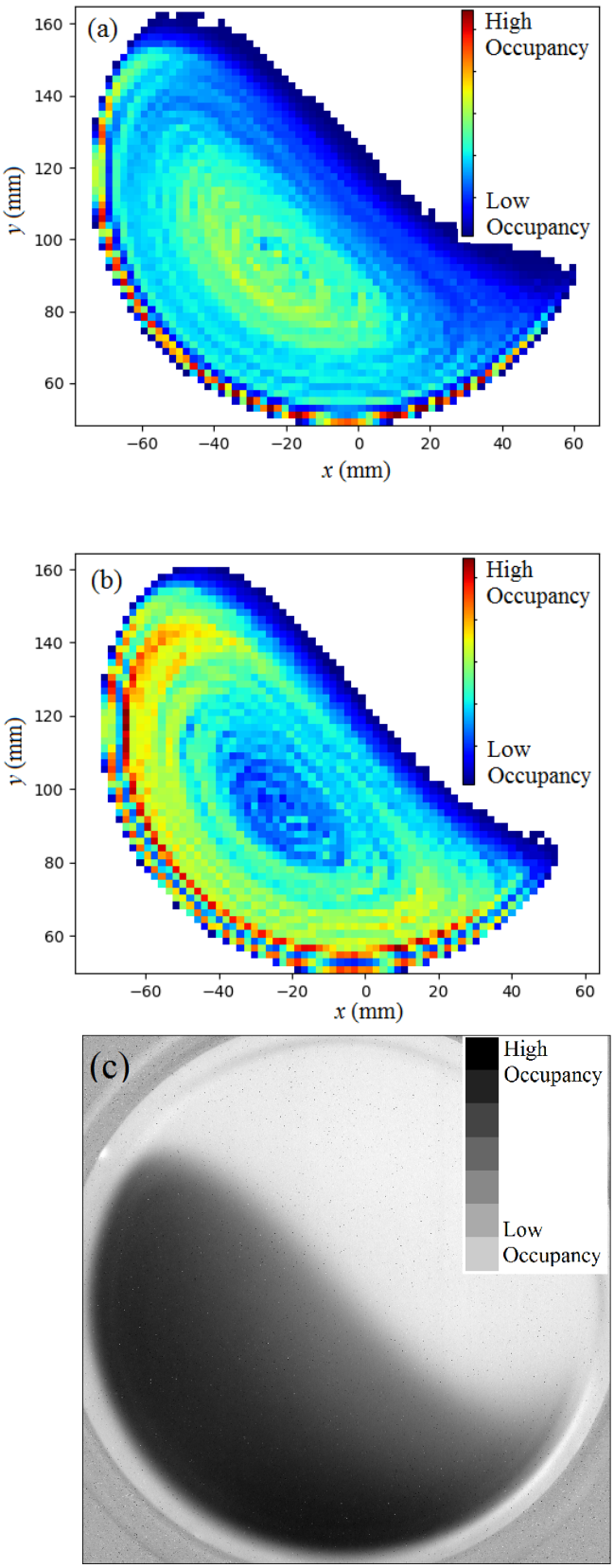

FIGURE 5.11: Results showing the PEPT occupancy *xy* projections for (a) 8.0 mm glass tracer, (b) 12.0 mm glass tracer and (c) the FNR image at the same rotation speed

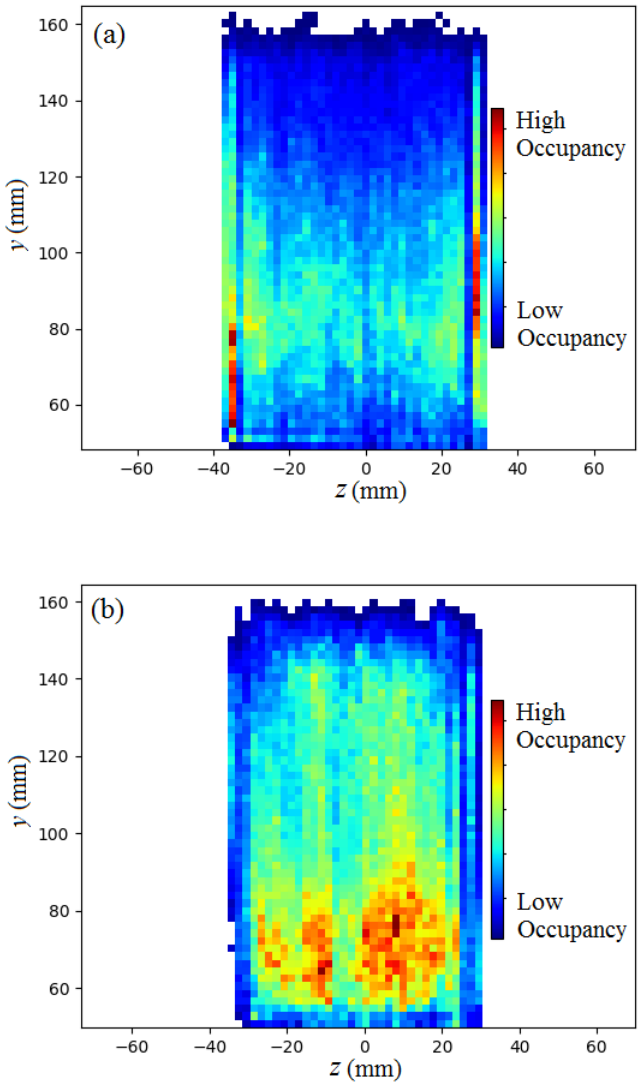

FIGURE 5.12: Results showing the occupancy zy projection for the mix of glass beads with (a) 8.0 mm glass tracer and (b) 12.0 mm glass tracer

The three dimensional speed of the tracer in the two dimensional *xy* projection is presented in Figure 5.13, which shows the speed of the 8.0 mm glass tracer, Figure 5.13(a) and the speed of the 12.0 mm glass tracer, Figure 5.13(b). The speed data shows the areas that contribute to the rising and active regions of the mill charge. The speed data from the 12.0 mm glass tracer has a larger active region when compared to the speed data from the 8.0 mm glass tracer, this is due to the 12.0 mm glass tracer having a higher frequency of occurrence in the outer locations of the mill charge and is thus subject to more of the rotation effects. This is a fundamental characteristic of comminution where bigger particles are broken down into smaller parts by moving through the rising region into the active region of the mill charge.

The time averaged velocity field for the two tracers is presented in Figure 5.14. The fields show the movement of the beads through each of the regions within the mill charge. The average velocity of the 8.0 mm glass tracer and the 12.0 mm glass tracer are affected more by their presence within the specific rising, active or in-flight regions. This relates to the basic process within the tumbling mill during rotation as each region feeds into another, to facilitate better comminution.

This correlation shows the complementarity of the techniques with the PEPT technique being able to record the location of the tracer, in three dimensions, from which the shape of the mill charge can be presented in the *xy* and *zy* projections. Both techniques can be applied to opaque, dense and turbulent systems where optical techniques will fail. The data takes a longer time for an adequate number of LORs to be acquired for these PEPT projections. A minimum of 15.0 minutes per acquisition is needed to get a first estimate of the bulk shape, where FNR takes 5.0 seconds. However to improve the statistical accuracy, both techniques benefit from longer acquisitions.

Both PEPT and FNR can present the shape of the mill charge and layering of the beads, during rotation, and represent the steady state of dynamic flow. In addition, PEPT can distinguish between beads of different diameters and also present the speed of the tracer at each location, which is useful for examining the different regions of the mill charge during rotation. PEPT also records data in three dimensions and allows for the examination of different projections from the same data set which cannot be done using FNR. FNR is a complementary technique to PEPT as it can, from the *xy* projection, show the overall density distribution of the mill charge in *zy* and has a shorter acquisition time. Together these techniques provide a deeper and more complete understanding of the dynamics of the internal mill charge experienced during rotation.

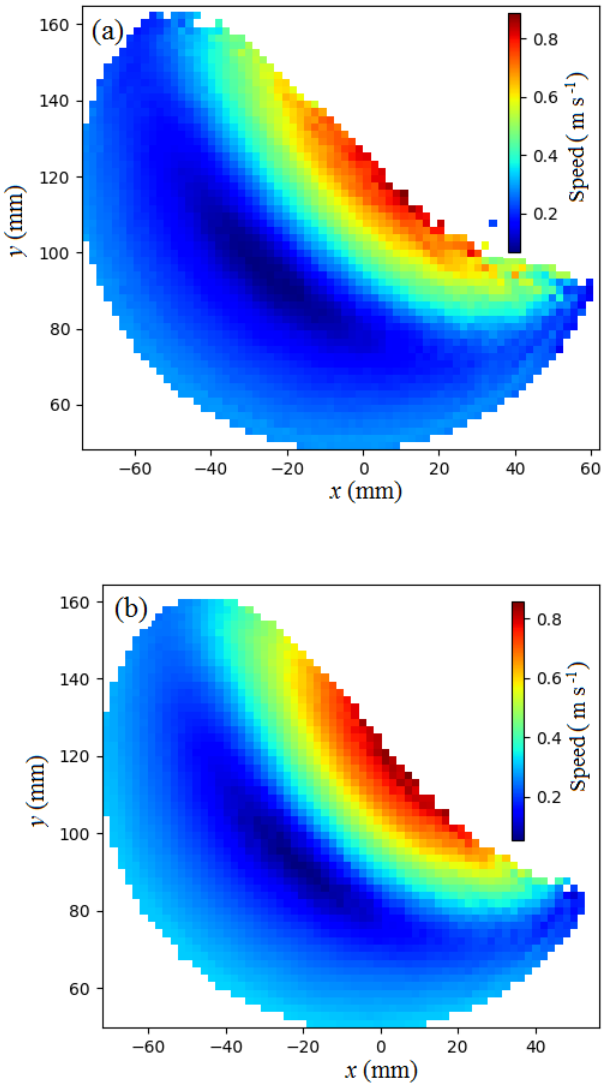

FIGURE 5.13: Speed of the tracer in the *xy* projection for (a) 8.0 mm glass tracer and (b) 12.0 mm glass tracer

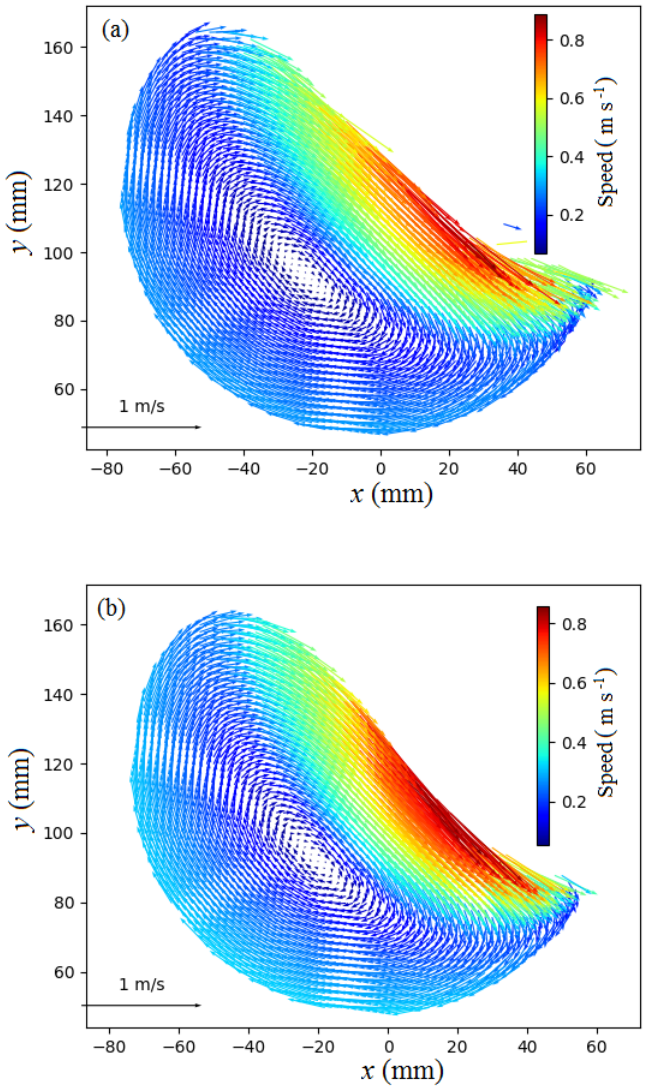

FIGURE 5.14: The average velocity field in the xy projection for a mill charge comprised of (a) 8.0 mm glass tracer and (b) 12.0 mm glass tracer

Chapter 6

Flow of Water through Porous Media

6.1 Introduction

Water content and its associated flow within media such as sand, soil or concrete are important parameters related to structural integrity. The ability to optimize the fluid flow in structures plays a pivotal role in planning for the best structural designs and for the best water saving. The inherent porosity of the media facilitates the internal flow or trapping of the water, which in turn influences the transmutation of water to the dryer areas.

One parameter used to classify the flow of water through media is the hydraulic conductivity, k. This is an intrinsic property of the medium and is related to the ability of the medium to transmit fluid. In sand, for example, it represents the ease with which water can move through the pores of the sand. Hydraulic conductivity is affected by the intrinsic permeability and saturation of the sand as well as the density and viscosity of the water. Knowledge of k is important for understanding the movement of water through sand, transport of water through to roots and the flow of water to drains.

The water content in concrete and sand is also an important parameter related to the structural integrity of a building. One contributing reason to cracking of building structures is the water content present in the concrete or sand, which when insufficient, creates voids in the structure which facilitates cracking or spalling. Slowing the cracking process in concrete or sand is better understood when the internal water content is known [104]. This directly relates to strength, efficiency, safety and life time of structures. Testing a sample for its porosity, sorptivity and water retention capability is a traditionally destructive process and does not allow for quick testing on site [105].

The flow of water moving along a pressure gradient is a feature of the pore structure of sand and is modelled as a capillary tube [106]. Sand pores form capillaries which makes the flow of water through them similar to that of the flow of water

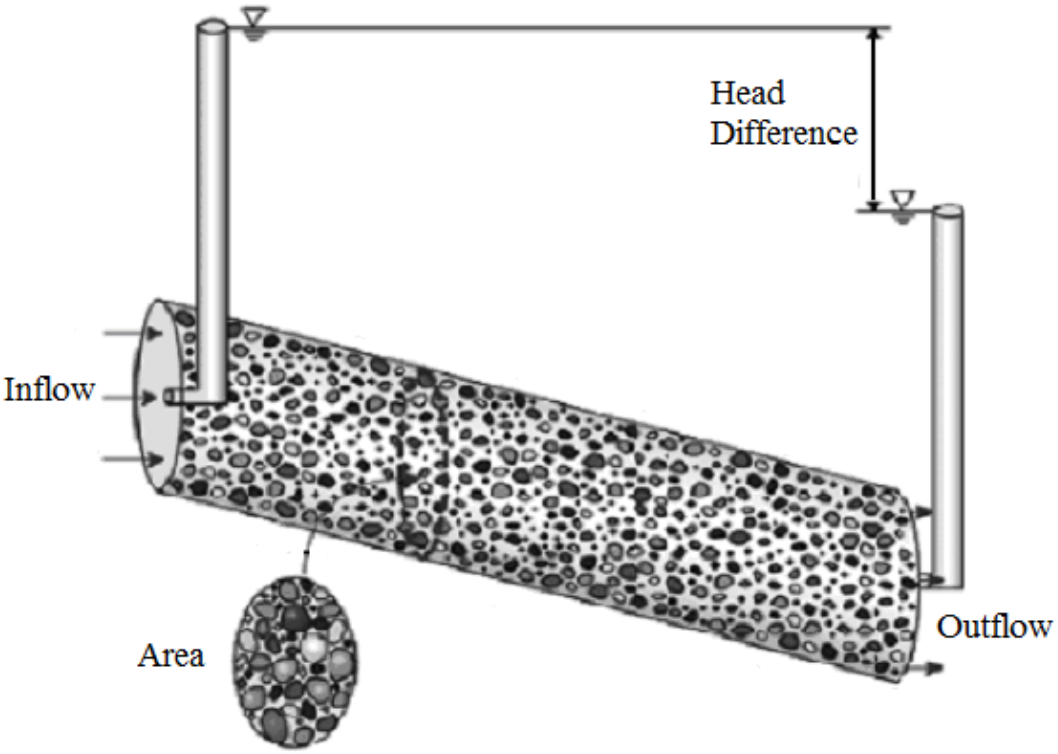

FIGURE 6.1: Representation of the application of Darcy's Law for the flow of water through porous sand

through capillary tubes of a constant diameter. The capillary tube has an internal pressure gradient related to the slope of the tube and this promotes the flow of water along the gradient, which is proportional to the rate of flow. The pressure gradient is directly related to the size of the grains, where small grains act as small pores having a lower hydraulic conductivity and the opposite applies for large grains. It is then possible to account for the water that flows from a point of high matric potential to low matric potential (dry) [107].

The study of the flow of water was quantized by Darcy, who examined the flow of water through saturated sand for the city of Dijon. He derived an equation, the so called "Darcy's Law" Equation (6.1), which describes the hydraulic conductivity (k) [3]. The constant head method is typically applied for granular sand. The hydraulic head (or head) is made up of the pressure head and elevation head, which is a measure of the potential of the water fluid due to gravity, at a measured point, which is represented by the vertical tubes in Figure 6.1. In this procedure, water is observed to move through the sand, under a steady state head condition, while the quantity of water moving through the sand is measured over time.

The hydraulic conductivity, k, is calculated by knowing Q, the quantity of water measured which in this case is the volume of water present, L the length of the specimen at time t, A the cross-sectional area and h the head height. Darcy's Law is thus

expressed as:

$$k = \frac{QL}{tAh}. \tag{6.1}$$

Another method used to calculate hydraulic conductivity makes use of the air entry head and accounts for the rate of decrease of the hydraulic conductivity over the increasing suction head, Figure 6.2, and is given by Gardner's Equation (6.6) [4].

The rate of capillary rise in the soil describes the flow of water from lower to a higher elevation across the hydraulic pressure gradient. The three fundamental aspects of the rise of water are [4]:

- the maximum height of the capillary rise (h_c);
- the fluid storage capacity of capillary rise; and
- the rate of capillary rise.

Each aspect contributes to the water flow. An assumption made in the theoretical development, is that the flow will be governed by Darcy's Law [108] with the hydraulic gradient responsible for the capillary rise given in Equation (6.2),

$$i = \frac{h_c - z}{z} \tag{6.2}$$

where h_c is the maximum height of capillary rise and z is the height measured positively upward. A graphical representation for the movement of water is shown in Figure 6.2 which also shows the air-entry head, h_τ.

Using Darcy's Law, the capillary rise takes on the form given in Equation (6.3),

$$q = k_s i = n\frac{dz}{dt} \tag{6.3}$$

were q is the discharge velocity, k_s the saturated hydraulic conductivity and n the porosity of the soil. Obtaining the time taken, t, for capillary rise is achieved by combining Equation (6.2) and Equation (6.3) and solving as shown below,

$$\begin{aligned}
\frac{dz}{dt} &= \left(\frac{h_c - z}{z}\right)\frac{k_s}{n} \\
\int \frac{z}{h_c - z} dz &= \int \frac{k_s}{n} dt \\
-z - h_c\left[\ln\left(h_c - z\right)\right] &= \frac{tk_s}{n} + cst \\
t &= \frac{nh_c}{k_s}\left[\ln\left(\frac{h_c}{h_c - z}\right) - \frac{z}{h_c}\right]
\end{aligned} \tag{6.4}$$

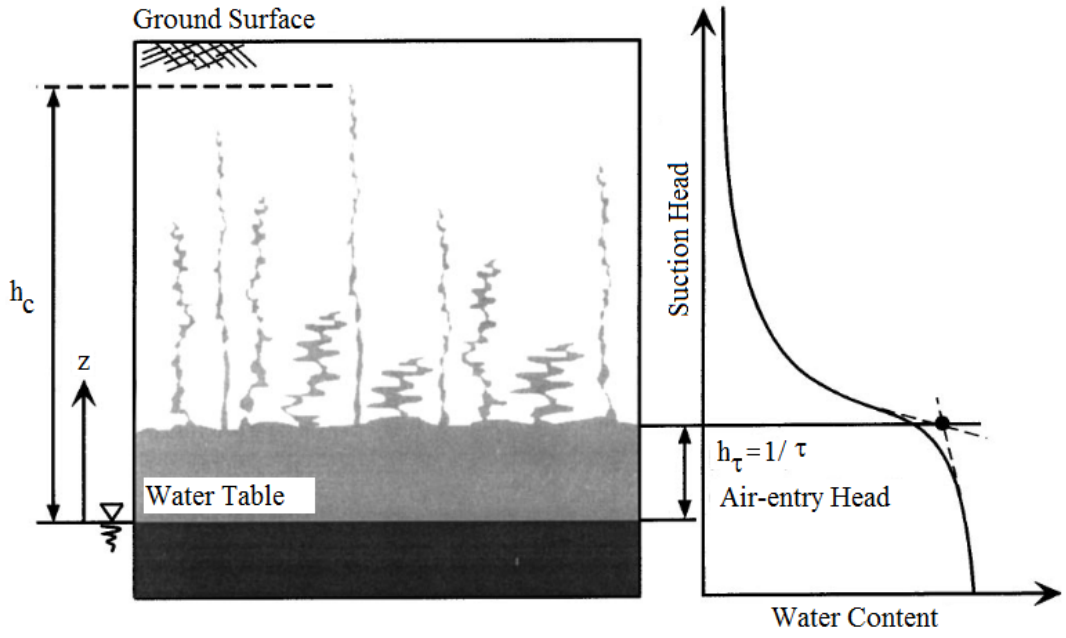

FIGURE 6.2: Conceptual model for capillary rise of water in sand with a water content curve on the right

which has an initial condition of t and z being zero. Equation (6.4) [108] gives a relation between the time and height of capillary rise. Another form for the rate of capillary rise using the inverse of the air-entry head (τ) is given by Equation (6.5),

$$\frac{dz}{dt} = \frac{k}{n}\exp(-\tau z)\frac{h_c - z}{z}, \tag{6.5}$$

from which Gardner's Equation [4] for the hydraulic conductivity is derived and shown in Equation (6.6),

$$k = k_s exp(-\tau z). \tag{6.6}$$

Here k_s is the saturated hydraulic conductivity, τ the inverse of the air-entry head and z the height along the suction head, presented in Figure 6.2.

6.2 Experimental setup

The experiments were carried out on the polychromatic beamline at the PTB facility in Braunschweig. The fast neutron beam is produced via the ^{9}Be(d,n) reaction occurring at the target station of the CN28 isochronous cyclotron. The cyclotron has an incident deuteron beam energy of up to 11.50 MeV. A 3.0 mm ^{9}Be target is used with the reaction producing a fast neutron beam having an energy spectrum ranging from 2.0 MeV – 15.0 MeV with a peak at 5.50 MeV [77].

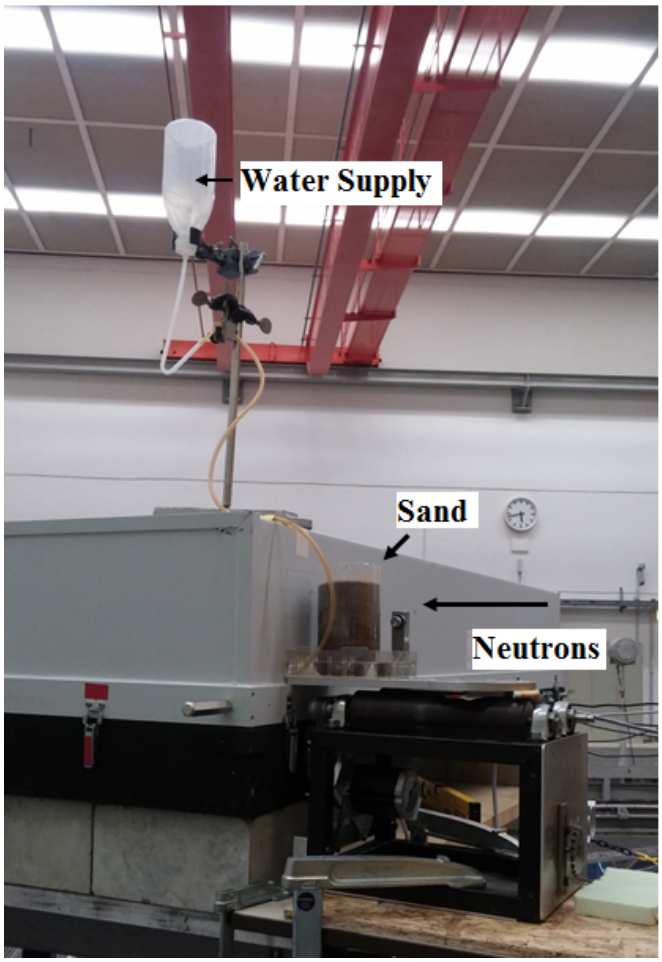

FIGURE 6.3: Experimental setup of the sample showing the directional flow of water while employing the constant head method to determine the hydraulic conductivity

The deuteron beam spot is approximately 5.0 mm with a beam current of 40.0 μA yielding a fast neutron flux of 10^8 n s^{-1} cm^{-2}. As fast neutrons interact with the atomic nuclei and have a higher interaction cross-section for lighter elements [75], they are favoured for this study due to the abundance of lighter elements in water. The constant head method is employed using a cylindrical container with a diameter of 8.70 cm and a height of 14.0 cm, placed in a bath of water. The cylinder is filled with dehydrated sand with the setup presented in Figure 6.3 and the schematic shown in Figure 6.4. The fast neutron radiographs were recorded using the same system described in Section 4.2.

The setup presented in Figure 6.3 is placed 1.20 m away from the target station of the cyclotron and positioned to be in contact with the scintillation screen of the fast neutron imaging detector. Water fills the dish in which the cylinder is placed. The flow of water through sand is imaged using the fast neutron detector with the images obtained for an acquisition time of 12.0 s.

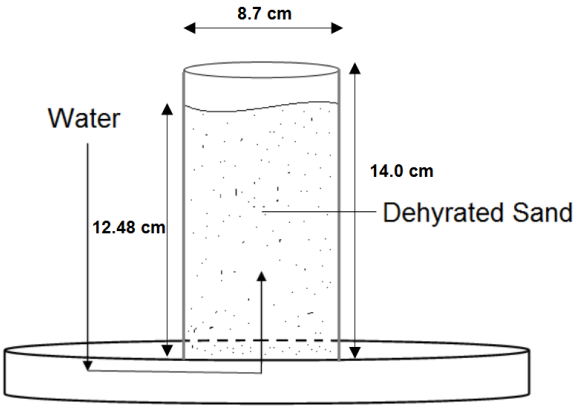

FIGURE 6.4: Schematic showing the flow of water for the setup presented in Figure 6.3

TABLE 6.1: The effective thickness of each region of interest used in the analysis to calculate the hydraulic conductivity k

RoI	x_{RoI} **(cm)**
1	8.70
2	5.17
3	5.17
4	8.70
5	8.70

6.3 Results

The flow of water through sand, shown in Figure 6.3, is imaged using fast neutron radiography and presented in Figure 6.5. The five Regions of Interest (RoIs) are defined and presented in Figure 6.6. The flow of water through these regions of interest is used to calculate the important characteristics related to the flow of water through sand. Each region of interest has a cross-sectional area of 1.45 cm^2 and thickness, x_{RoI}, as given in Table 6.1.

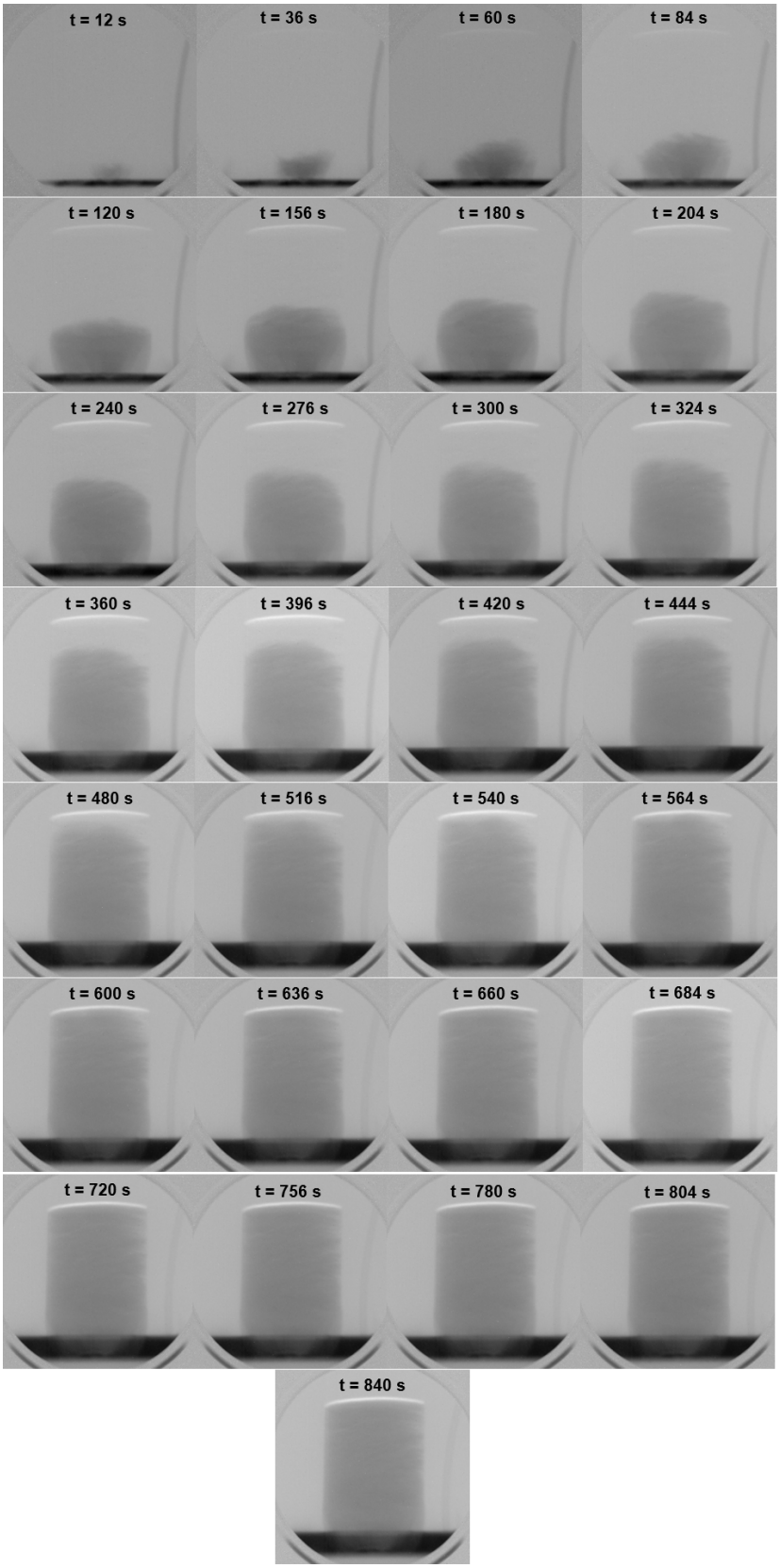

FIGURE 6.5: Fast neutron radiographs showing the absorption of water in a cylinder of sand. The increasing presence of water in the sand is represented by the dark region that grows as a function of time

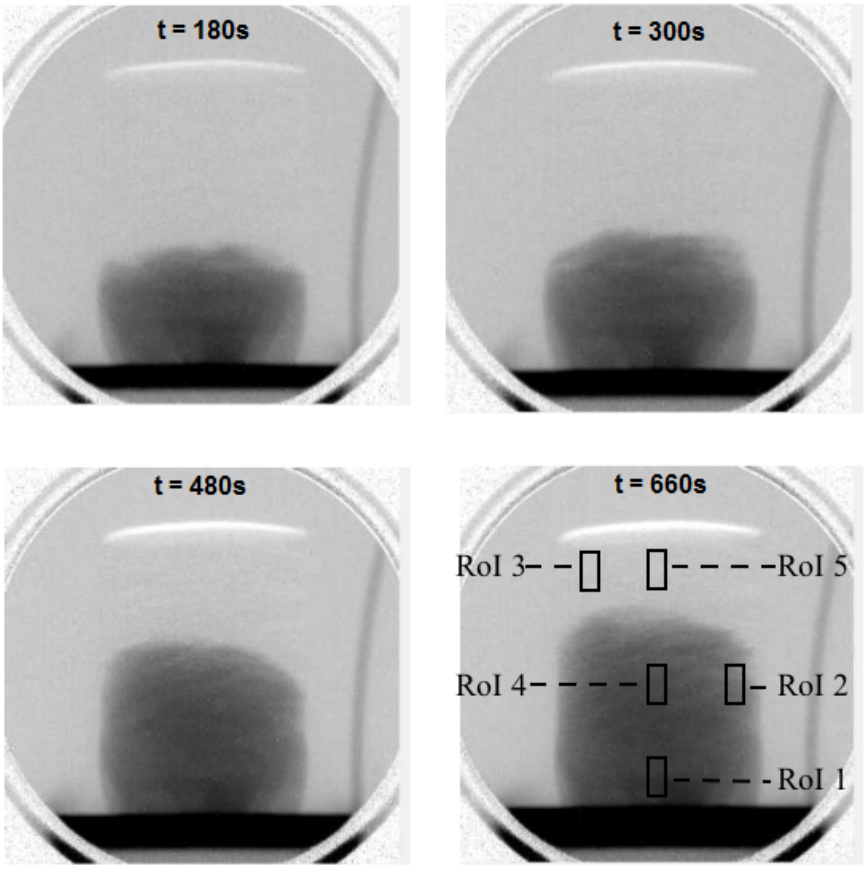

FIGURE 6.6: The regions of interest, referred to in Table 6.3, used to examine the flow of water through the sand sample

The Beer-Lambert Law, Equation (4.5), is applied to the transmission of the fast neutrons through the five regions of interest, I_{ws} and I_s. I_{ws} is the transmission through the water-sand mixture, I_s the transmission through the sand and I_w is the transmission through pure water. These are time dependent and presented in Figure 6.7.

The transmission of the neutrons through the regions of interest decreases with increasing time; this is due to a higher volume of water present within the RoIs. The ratio I_{ws}/I_s plateaus over time which is a result of the region of interest reaching saturation.

RoI1 saturates faster than the other regions of interest and this is due to RoI1 being closer to the source of water. This trend can be observed through each of the other regions of interest, as over time the water progresses up along the hydraulic gradient and begins to saturate the higher lying regions.

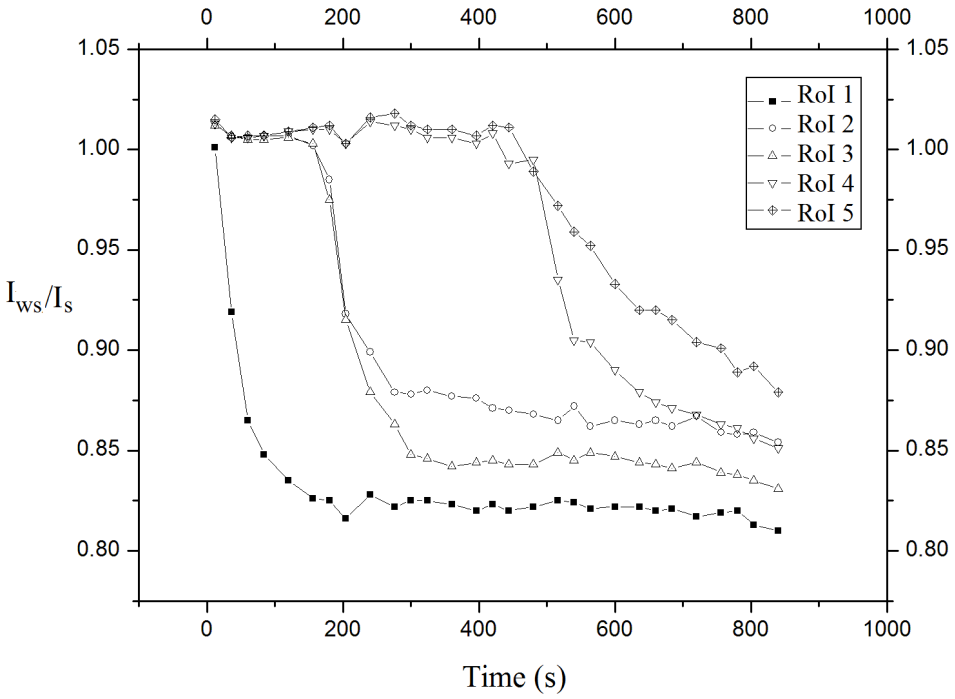

FIGURE 6.7: Comparing the transmission of fast neutrons through the sample during water absorption examined at different regions of interest

This is a complex system with a mixture of materials each having its own attenuation coefficient. There is, therefore, a contribution from both water and sand to the overall attenuation of the sample. Representing the sample as two independent parts, Figure 6.8, which has an overall thickness x_α, the thickness contribution of water and sand to the overall sample thickness, is given by αx_α and $(1-\alpha)x_\alpha$ respectively.

Examining the transmission and attenuation of the mixed sample, a function is derived for the factor α using the technique of Anderson *et.al* [109], which calculates the contribution of water in the complex system. The term α is known as the volume contribution factor and varies with time. If there are more than two contributors to the attenuation, a single neutron energy will not be sufficient to obtain a volume contribution factor, and in this case two neutron energies would be required and is explained in Appendix A. The derivation of factor α follows,

$$\begin{aligned} I_{ws} &= I_0 e^{\Sigma_i^n \mu_i x_i} \\ &= I_0 e^{-\mu_s(1-\alpha)x - \mu_w \alpha x} \\ &= I_0 e^{-\mu_s x + \mu_s \alpha x - \mu_w \alpha x} \\ &= I_0 e^{-\mu_s x - \alpha(\mu_w - \mu_s)x}. \end{aligned} \tag{6.7}$$

Inserting $I_s = I_0 e^{-\mu_s x}$ into Equation (6.7),

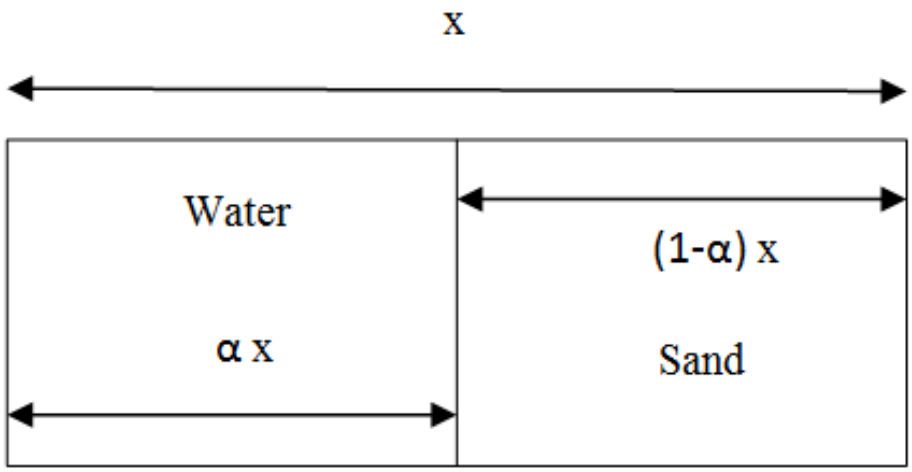

FIGURE 6.8: Volume contribution for a mixed sample

$$\begin{aligned}
\frac{I_{ws}}{I_s} &= e^{-\alpha(\mu_w-\mu_s)x} \\
\implies -\alpha\left(\mu_w-\mu_s\right)x &= \ln\left(\frac{I_{ws}}{I_s}\right) \\
\implies \alpha\left(-\frac{1}{x}\ln\left(\frac{I_w}{I_0}\right)+\frac{1}{x}\ln\left(\frac{I_s}{I_0}\right)\right) &= -\frac{1}{x}\ln\left(\frac{I_{ws}}{I_s}\right) \\
\implies \alpha &= \frac{\ln\left(\frac{I_{ws}}{I_s}\right)}{\ln\left(\frac{I_w}{I_s}\right)}
\end{aligned} \tag{6.8}$$

where Equation (6.8) gives the volume contribution factor α, for the mixed sample.

Equation (6.8) is applied to each region of interest to calculate α, with the results presented in Figure 6.9. The volume contribution factor, α, grows faster in RoI1 when compared to the other regions of interest. Figure 6.9 shows an initial faster growth, indicative of a fast absorption rate and a plateau in the rate after 240 s as RoI1 tends toward saturation.

The presence of water along the height of the suction head at a time of 12 s, 240 s, 360 s, and 480 s respectively, is used to obtain the value for the inverse air-entry head, τ. This is calculated using a water content curve. The inverse air-entry head τ is measured from the profiles presented in Figure 6.10.

Figure 6.10 shows the water content along the height of the cylinder, with the lower regions showing a higher presence of water, over time, and the higher lying regions showing a lower presence of water, which is due to the hydraulic conductivity falling

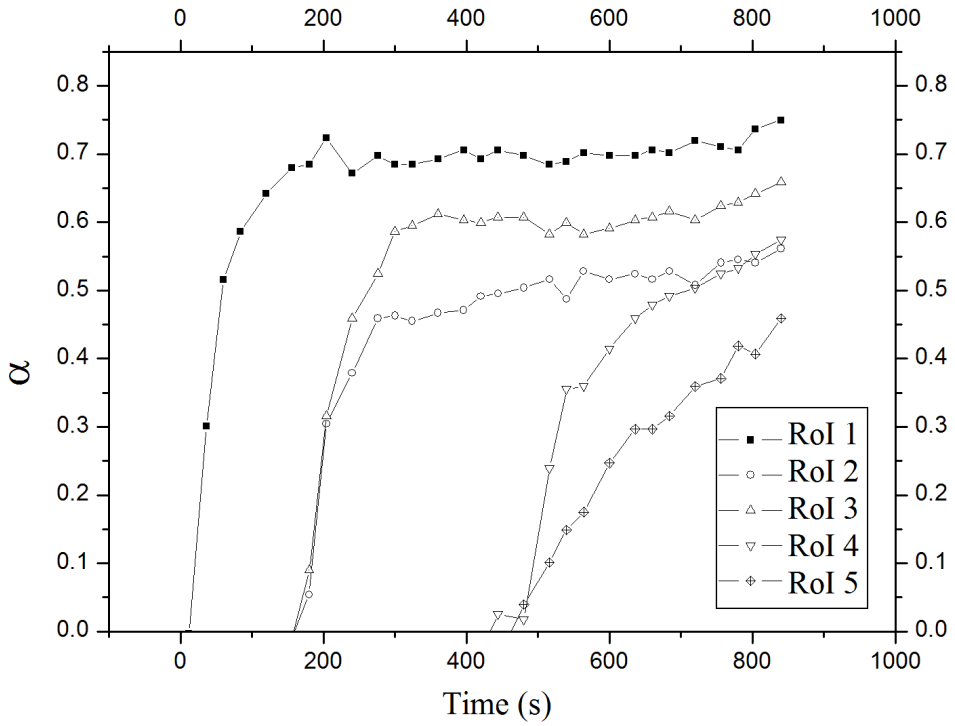

FIGURE 6.9: Increasing volume contribution of water in sand, observed over the acquisition time

off over the increasing suction head. At each time the water content profile changes as the water moves along the suction head and from each profile the inverse air-entry head, τ, is calculated and the values for τ are shown in Table 6.2.

The saturated hydraulic conductivity of sand, k_s, was calculated using the Allen Hazen Approximation, Equation (6.9) [110][111] and ranges from 0.4 cm s^{-1} to 7.2 cm s^{-1},

$$k_s = C(D_{10})^2, \tag{6.9}$$

TABLE 6.2: The inverse air-entry head (τ) values for the sample taken at different times during the absorption of water

Time (s)	τ **(cm^{-1})**
12	4.72
240	1.073
360	0.843
480	0.694

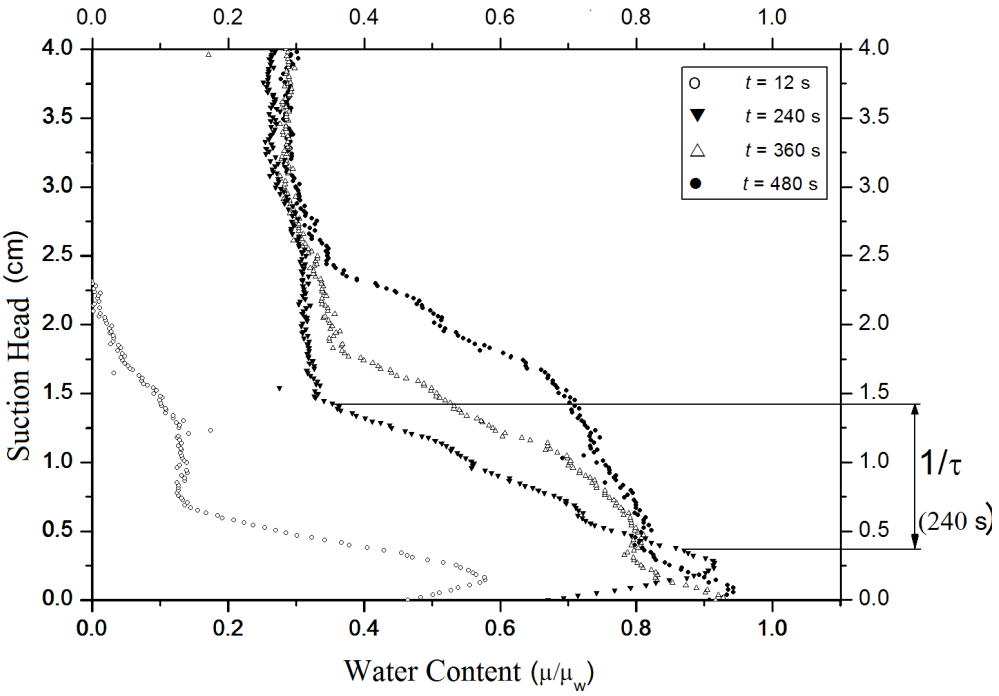

FIGURE 6.10: Water content of the sample along the suction head obtained at times of 12 s, 240 s, 360 s and 480 s

and for garden sand the range for the diameter of the sand particles D and the normalization constant C are given as [110],

$$\begin{aligned} D_{10} &= 0.1 - 0.3 \text{ cm} \\ C &= 40 - 80 \text{ cm s}^{-1} \end{aligned}$$

with the k_s range calculated below

$$\begin{aligned} k_s &= (0.1)^2(40) - (0.3)^2(80) \\ &= 0.4 - 7.2 \text{ cm s}^{-1}. \end{aligned}$$

Using this range of values for k_s and the values in Table 6.2, the hydraulic conductivity k of the sand is calculated using Equation (6.6) along the suction head and presented in Figure 6.11. A hydraulic conductivity k is performed at a time of 360 s, a height of 9.3 cm (a combination of L and h from Darcy's Law below) and k_s of 5.84 cm s^{-1},

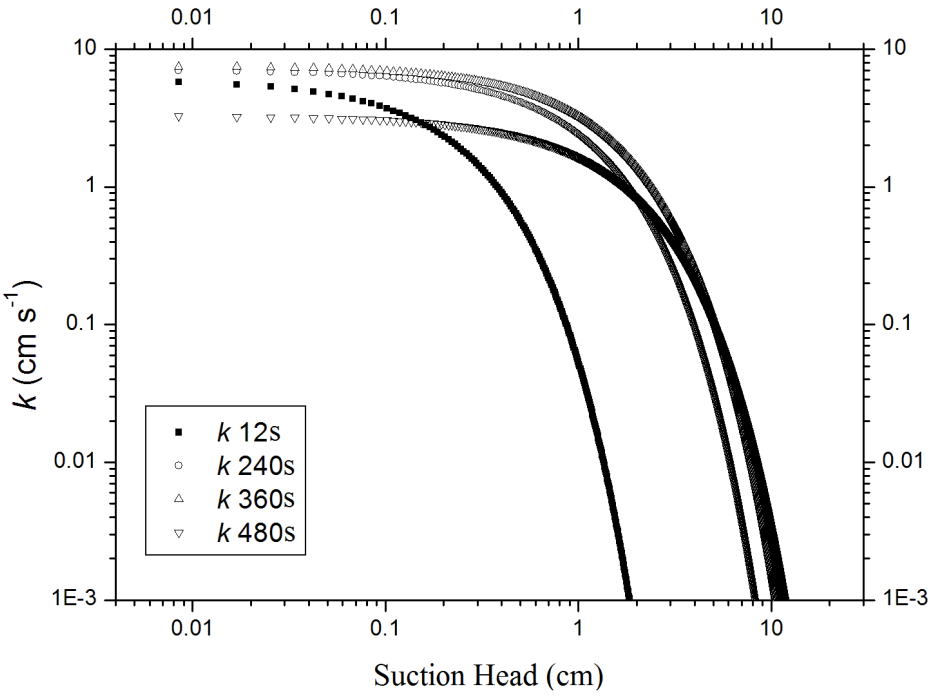

FIGURE 6.11: The hydraulic conductivity along the suction head of the sample obtained from Gardner's Equation at different observation times

$$\begin{aligned} k &= k_s \exp(-\tau z) \\ &= 5.84 \exp(-0.86(9.3)) \\ &= 0.00297 \text{ cm s}^{-1}. \end{aligned}$$

In a similar way, k is calculated for the times mentioned in Table 6.2. Figure 6.11 shows that the higher hydraulic conductivity occurs at the regions of interest closer to the water source when compared to the higher lying regions of interest.

Figure 6.11 shows how the hydraulic conductivity k changes along the suction head as time increases. These results are to be compared to the results obtained when calculating k using Darcy's Law, Equation (6.1), which produces values for k at a specific length L from the quantity (volume) of water Q passing through an area A. These parameters are obtained from the fast neutron radiograph and inserted into Equation (6.1). As water is absorbed along the suction head, there will be a unique L, Q and A at each specific time t. The value of Q is calculated comparing the attenuation coefficient at a length L and the attenuation coefficient of water μ_w. The parameters used to calculate k are given in Table 6.3.

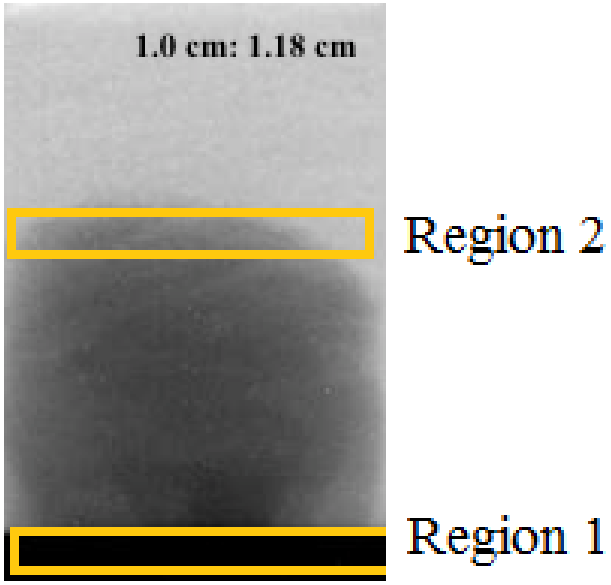

FIGURE 6.12: Regions used to obtain the required parameters for application in Darcy's Law

Figure 6.12 has a Region 1 and a Region 2, both of equal area, A. Region 1 is fully saturated while Region 2 is comprised of both water and sand.

The ratio I_{ws}/I_s from Region 2 is compared to the ratio I_w/I_s from Region 1 and gives a percentage contribution of water present in Region 2. The volume of water in Region 1 is multiplied by the percentage contribution between Region 1 and Region 2, yielding the quantity of water present in Region 2. For t = 360 s the ratios, $(I_{ws}/I_s)/(I_w/I_s)$, give the percentage contribution of water in Region 2 as 12.8% when related to Region 1. Therefore Q at this time is calculated to be

$$\begin{aligned} Q &= 119.38(12.8\%) \\ &= 15.28 \text{ cm}^3 \end{aligned} \tag{6.10}$$

where 119.38 cm^3 is the volume of water in Region 1. Inserting these into Equation (6.1), the value for k is calculated as,

$$\begin{aligned} k_{360s} &= \frac{LQ}{tAh} \\ &= \frac{7.29(15.28)}{360(59.52)(1.75)} \\ &= 0.00297 \text{ cm s}^{-1} \end{aligned} \tag{6.11}$$

TABLE 6.3: Input parameters for Darcy's Law to calculate the hydraulic conductivity, k

Time (s)	**Q (cm^3)**	**L (cm)**	**h (cm)**	**A (cm^2)**
12	0.34	0.97	0.478	10.35
240	8.13	5.92	1.157	56.85
360	15.28	7.29	1.75	59.52
480	54.74	7.67	2.179	147.63

TABLE 6.4: Comparison between the Darcy's Law calculation and Gardner's Equation calculation

Time (s)	***k* - Darcy's Law** (cm s^{-1})	***k* - Gardner's Equation** (cm s^{-1})
12	0.00556	0.00555
240	0.00305	0.00304
360	0.00297	0.00297
480	0.00273	0.00273

which compares favourably to the value calculated using Gardner's Equation, at t = 360 s. Similar calculations are carried out for t = 12 s, 240 s and 480 s.

Inserting these parameters into Equation (6.1), the value of k is calculated using Darcy's Law and presented in Figure 6.13 which shows the values of k calculated at varying times.

Figure 6.13 illustrates the changing hydraulic conductivity when compared to the matric potential, over increasing time [107]. The higher-lying regions are dryer and have a low matric potential with a higher k. As water travels to the higher regions, this increases the matric potential and lowers the value of k, which is shown by the hydraulic conductivity diminishing for t = 12 s, 240 s, 360 s, and 480 s.

Comparing the values for k obtained from Darcy's Law and Gardner's Equation, a good agreement between the results from the two methods is observed and shown in Figure 6.14 and Table 6.4, which emphasises the benefits of FNR to yield quantitative information for this porous media system.

The results given in Figure 6.9 present the amount of water absorbed and the amount of water present in a sample, at a given time, when compared to a dry sample. The benefit of using fast neutron radiography is the high attenuation of fast neutrons

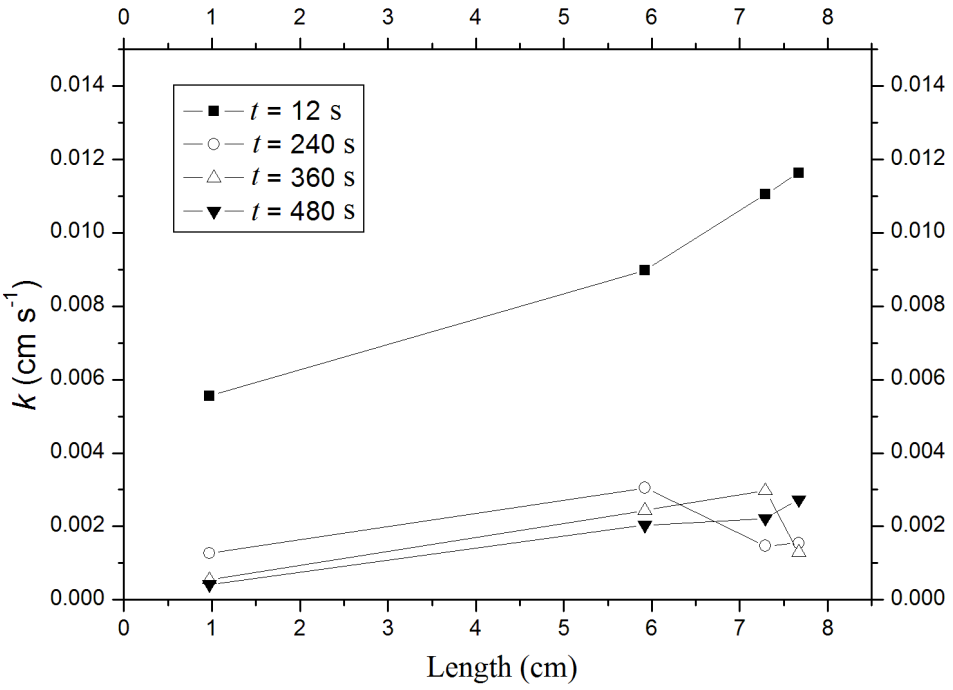

FIGURE 6.13: Hydraulic conductivity of the sample calculated using Darcy's Law, along the length of the sample

by water and an increased penetration of fast neutrons, which allow for the examination of thicker samples. The water is absorbed through the sand and the amount of water present is calculated and shown by an increase in α. When compared to water absorption examined using thermal neutrons [112], the fast neutron radiography investigation can analyse thicker samples.

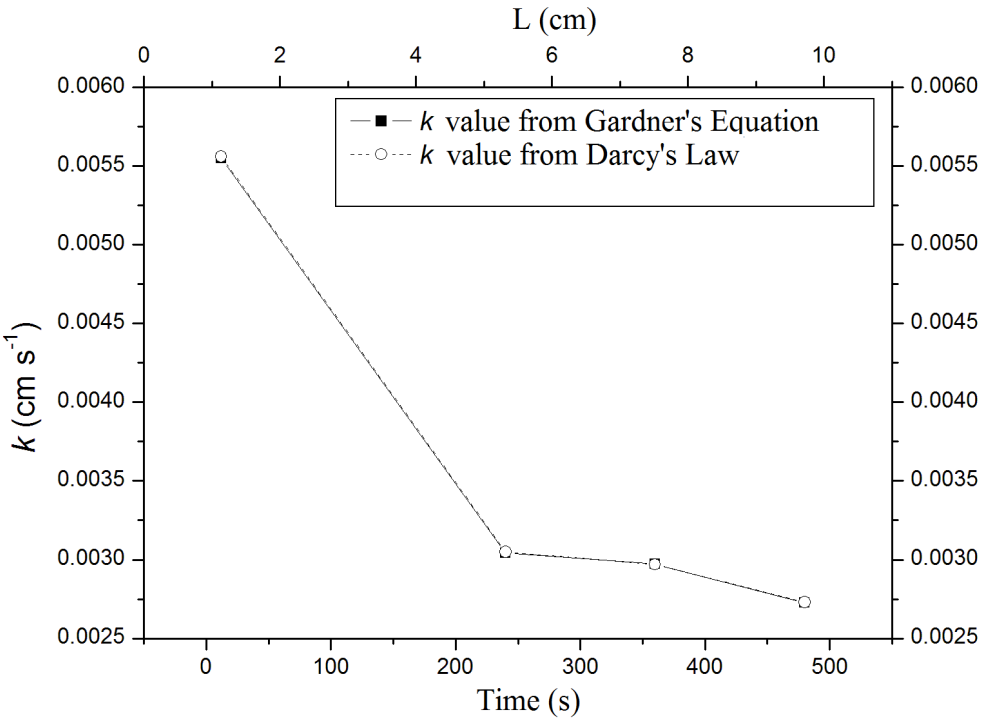

FIGURE 6.14: The comparison of the hydraulic conductivity between Darcy's Law and Gardner's Equation over time on the lower x-axis and length on the upper x-axis

Chapter 7

Conclusion

Fast Neutron Radiography (FNR) exploits the characteristics of fast neutrons to provide a non-destructive method that can determine the structure and elemental composition of materials in bulk. FNR has the potential of adding benefit to industrial applications in order to optimize both constitutional design and operation. Recent advances in fast neutron sources and the electronics associated with FNR systems, enables the FNR technique to positively impact applications requiring a high repetition rate, in order to examine larger samples.

This work had three components, the first of which investigated the development of a new FNR system at Necsa, for the purpose of identifying lower atomic number materials and the internal structures of cultural heritage samples. The second, performed measurements in which FNR was applied to systems that examined the flow within a column and a cylindrical mill. The third combined, for the first time, FNR and PEPT which were used to observe the dynamic flow within a tumbling mill system.

Optimizing the transmission of the deuteron beam onto the target of the Radio Frequency Quadrupole (RFQ) accelerator at Necsa, using the High Energy Beam Transport (HEBT) system, enabled the creation of an intense fast neutron source, which was applied to the preliminary FNR tests. The quantitative evaluation of samples showed the ability of FNR to penetrate larger samples and identify lower Z materials, such as polyethylene. A consequence of the evaluation, in which water in an aluminium cannister was imaged, was an investigation to quantify the movement of water through porous media.

When observing the flow of water through a sample of dehydrated sand, FNR was able to follow the progression of the waterfront, through this porous media, as a function of time. The advantage afforded by FNR in this observation is its ability to observe the flow of water through thicker samples. The presence of water and associated volume within the sand sample was then determined. The hydraulic conductivity, k, of the sand was calculated using both Darcy's Law and Gardner's Equation with a good correlation achieved between the two methods. The present results impact fields

where the movement of water in structures relates directly to the structural integrity and intrinsic permeability.

The FNR technique was also applied to examine the movement of the mill charge within a laboratory-scale tumbling mill during rotation. The steady state formed by the dynamically moving mill charge was observed in the radiographs acquired. The shape of the mill charge, at specific rotation speeds, was used to derive several operational parameters that are related to the overall milling efficiency. Furthermore, the parameters of the tumbling mill used to describe the shape of the mill charge has potential in the modelling of these turbulent flow systems. This benefits the industrial mining sector where the optimal tumbling mill design, before up-scaling, is crucial in the development and success of the ore crushing mills.

The technique of FNR gives one the ability to examine samples with a larger cross-sectional thickness, when compared to thermal neutrons (due to the fast neutron penetration depth into the sample) and samples rich in low z materials. The advantage of this is the ability to examine samples that have a high abundance of elements like hydrogen, or who have distinct fast neutron resonances. FNR provides a complementary advantage over other radiography techniques like thermal neutron radiography and x-ray scanning, whose advantage is in scanning samples with a lower cross-sectional thickness and high z materials, respectively. The rarity of discrete fast neutron sources results in a limitation of this technique, along with sensitivity to setup and scatter, which adversely affect the final image resolution.

The Positron Emission Particle Tracking (PEPT) method was also used to examine the motion of the mill charge by tracking a tracer element that was embedded within the mill charge itself. The sequential recording of the lines of response, which triangulate the position of the tracer with time, was used to determine the overall projected shape of the mill charge for the steady state condition. Emission/PEPT imaging has the advantage of tracking the movement of a single positron emitting particle to ascertain the flow of the bulk media. From this, the time averaged shape and evolution of the media can be tracked and analysed. A disadvantage relates to the time needed to obtain full comprehensive information for this ergodic system.

Comparing the results from the PEPT investigation to those obtained from FNR, showed for the first time a collation for the shape of the mill charge during rotation. PEPT also provides a more detailed account of the motion of the beads within the mill, during the tumbling phase, and this provides a deeper insight into the movement and distribution of the beads during rotation. PEPT also has the capability of selectively tracking beads of different diameters, which adds a further dimension into understanding the interactions between the components that comprise the rotating

mill charge.

7.1 Recommendations and Future Work

To be able to distinguish between two materials with different attenuating coefficients, two neutron energies are required when performing FNR with a theoretical description presented in Appendix A. This will enable FNR to identify and isolate each of the materials within a composite mixture. To test this approach, an experiment is to be performed on a tumbling mill system, having a composite mill charge comprised of two attenuating materials, which must then be exposed to two independent neutron energies when applying the FNR technique. The two independent neutron energies can be obtain by using the D(d,n)He reaction which is explained by Equation 2.8 and Figure 2.18. The method derived in Appendix A will be applied to the acquired FNR data to determine the ability to distinguish between materials with different attenuation coefficients.

Further future studies include the assembly and commissioning of the further developed fast neutron radiography system at Necsa (described in Section 3.7.4). The system will be applied in investigations that require the non destructive examination of valuable cultural heritage samples, which will be used in evolutionary studies and will also be applied to expand into the examination of flowing systems. A future drive of the new FNR system will be to implement a turn table that will launch the development toward a Fast Neutron Tomography (FNT) system.

The technique of PEPT will also be applied in the future to a study that involves the separation of irregularly shaped beads from spherical beads, while using a vibrating plate. The energy transferred onto the beads by the vibrating plate, governs their motion and the separation of the perfect/imperfect beads will be investigated with the outcomes being used to provide valuable parameters that will assist in building up the mathematical framework.

Appendix A

Resolving Multiple Attenuating Materials using FNR

A composite mix of three attenuating materials comprising a sample, is difficult to resolve, using a single neutron energy for the FNR application. The volume fraction calculated in Equation (6.8) can resolve between two independent attenuating materials but not for three, as the equations are coupled and cannot be resolved. The composite system is represented as shown in Figure A.1.

A.1 Single Energy

Applying Equation (4.5) to the composite system in Figure A.1 and simplifying it is obtained,

$$\begin{aligned} I &= I_0 \exp\left(-\Sigma_i \mu_i x_i\right) \\ &= I_0 \exp\left(-\mu_A \alpha x - \mu_B \beta x - \mu_C (1-\alpha-\beta) x\right) \end{aligned} \tag{A.1}$$

where Equation (A.1) shows the volume contribution and attenuating coefficient of the system. Using this together with the attenuation of the pure material C it is derived,

$$I_C = I_0 \exp\left(-\mu_C x\right)$$

and inserting into Equation (A.1) this simplifies to,

$$\begin{aligned} \frac{I}{I_C} &= \exp\left(-\left(\left(\mu_A - \mu C\right)\alpha x - \left(\mu_B - \mu_C\right)\beta x\right)\right. \\ \frac{1}{x}\ln\left(\frac{I}{I_C}\right) &= \alpha(\mu_C - \mu_A) + \beta(\mu_C - \mu_B) \end{aligned} \tag{A.2}$$

with constants $\mu_A, \mu_B, \mu_C, \frac{I}{I_C}$ and x together with the unknowns α and β. This is a

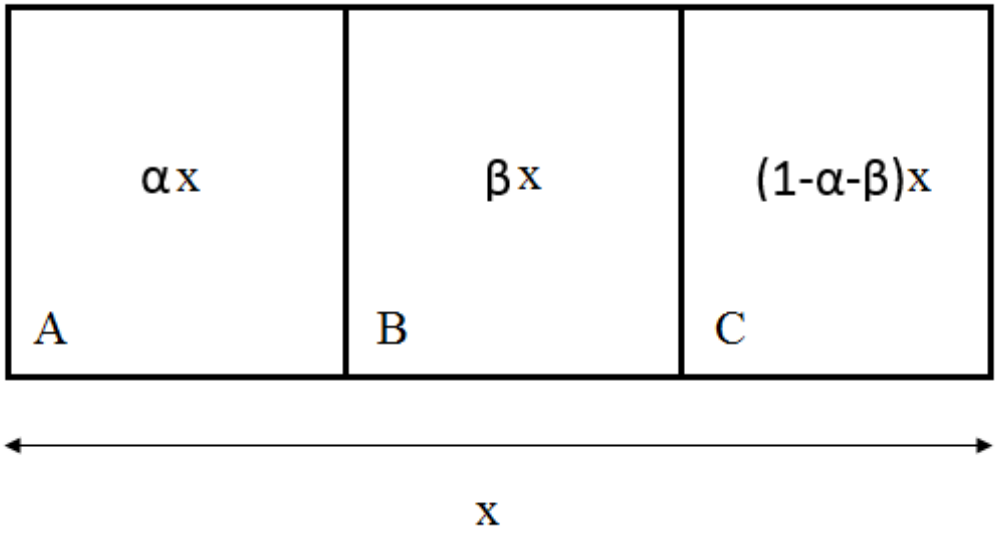

FIGURE A.1: Three attenuating materials in a composite system

single equation with two unknowns and therefore cannot be resolved using a single fast neutron energy.

A.2 Two Energies

Following the single neutron energy case, two different neutron energies are used in the derivation below by applying Equation (A.2),

$$\frac{1}{x}\ln\left(\frac{I_1}{I_{1C}}\right) = \alpha(\mu_{1C}-\mu_{1A})+\beta(\mu_{1C}-\mu_{1B}) \tag{A.3}$$

$$\frac{1}{x}\ln\left(\frac{I_2}{I_{2C}}\right) = \alpha(\mu_{2C}-\mu_{2A})+\beta(\mu_{2C}-\mu_{2B}) \tag{A.4}$$

with Equation (A.3) and (A.4) representing the calculation of the volume fraction. I_1 and I_2 are the transmission through the sample at neutron energies one and two, respectively. I_1C and I_2C are the transmission through a pure sample, *C*, at neutron energies one and two. μ_{ij} defines the attenuation coefficient taken at neutron energy i (i = 1 or 2) for material j (j = *A*, *B* or *C*).

From Equation (A.3) it is calculated that,

$$\alpha = \frac{1}{\mu_{1C}-\mu_{1A}}\left[\frac{1}{x}\ln\left(\frac{I_1}{I_{1C}}\right)-\beta\left(\mu_{1C}-\mu_{1B}\right)\right] \tag{A.5}$$

and placing in Equation (A.4) and defining $\mu_{ij}-\mu_{ik}=\mu_{ijk}$ for $j,k=A,B,C$ and $i=1,2$, β is derived below,

$$\frac{1}{x}\ln\left(\frac{I_2}{I_{2C}}\right) = \frac{1}{x}\left[\frac{\mu_{2CA}}{\mu_{1CA}}\right]\ln\left(\frac{I_1}{I_{1C}}\right) - \beta\left[\frac{\mu_{2CA}\mu_{1CB}}{\mu_{1CA}} - \mu_{2CB}\right] \tag{A.6}$$

$$\beta = \frac{\mu_{1CA}}{(\mu_{2CA}\mu_{1CB} - \mu_{2CB}\mu_{1CA})}\frac{1}{x}\left[\ln\left(\frac{I_1}{I_{1C}}\right)\frac{\mu_{2CA}}{\mu_{1CA}} - \ln\left(\frac{I_2}{I_{2C}}\right)\right] \tag{A.7}$$

by including Equation (A.5) into Equation (A.7) the solution for α is derived below,

$$\alpha = \frac{1}{x}\left[\frac{1}{\mu_{1CA}}\ln\left(\frac{I_1}{I_{1C}}\right) - \frac{\mu_{1CB}}{(\mu_{2CA}\mu_{1CB} - \mu_{2CB}\mu_{1CA})}\left(\ln\left(\frac{I_1}{I_{1C}}\right)\frac{\mu_{2CA}}{\mu_{1CA}} - \ln\left(\frac{I_2}{I_{2C}}\right)\right)\right]. \tag{A.8}$$

Using Equation (A.7) and Equation (A.8), the volume fraction of each of the materials *A*, *B* and *C* can be obtained using two distinct neutron energies.

Bibliography

1. Daniels, G., Franklyn, C., Dangendorf, V., Buffler, A. & Bromberger, B. Fast neutron radiography at an RFQ accelerator system. *Physics Procedia* **69.** *Proceedings of the 10th World Conference on Neutron Radiography (WCNR-10) Grindelwald, Switzerland October 5–10, 2014*, 109 –114. ISSN: 1875-3892. http://www.sciencedirect.com/science/article/pii/S1875389215006264 (2015).
2. Vartsky, D., Mor, I., Goldberg, M., Bar, D., Feldman, G., Dangendorf, V., Tittelmeier, K., Weierganz, M., Bromberger, B. & Breskin, A. Novel detectors for fast-neutron resonance radiography. *Nuclear Instruments and Methods in Physics Research Section A: Accelerators, Spectrometers, Detectors and Associated Equipment* **623.** 1st International Conference on Technology and Instrumentation in Particle Physics, 603 –605. ISSN: 0168-9002. http://www.sciencedirect.com/science/article/pii/S0168900210006480 (2010).
3. Darcy, H. *Les fontaines publiques de la ville de Dijon. Exposition et application des principes à suivre et des formules à employer dans les questions de distribution d'eau: ouvrage terminé par un appendice relatif aux fournitures d'eau de plusieurs villes au filtrage des eaux et à la fabrication des tuyaux de fonte, de plomb, de tole et de bitume* https://books.google.co.za/books?id=42EUAAAAQAAJ. (Dalmont, 1856).
4. Gardner, W. Steady state solutions of the unsaturated moisture flow equation with application to evaporation from a water table. *Soil Sci* (1958).
5. Von der Hardt, P. & Röttger, H. *Neutron radiography handbook: Nuclear science and technology* (Springer Science & Business Media, 2012).
6. De Beer, F. Neutron-and X-ray radiography/tomography: Non-destructive analytical tools for the characterization of nuclear materials. *Journal of the Southern African Institute of Mining and Metallurgy* **115,** 913–924 (2015).
7. Sowerby, B. & Tickner, J. Recent advances in fast neutron radiography for cargo inspection. *Nuclear Instruments and Methods in Physics Research Section A: Accelerators, Spectrometers, Detectors and Associated Equipment* **580,** 799–802 (2007).
8. Chadwick, J. The existence of a neutron. *Proceedings of the Royal Society of London A: Mathematical, Physical and Engineering Sciences* **136,** 692–708. ISSN: 0950-1207. eprint: http://rspa.royalsocietypublishing.org/content/136/830/692.full.pdf. http://rspa.royalsocietypublishing.org/content/136/830/692. (1932).

9. Marleau, P., Brennan, J., Brubaker, E., Mengesha, W., Mrowka, S. & Nowack, A. *Fast neutron resonance tomography using double scatter spectroscopy for materials identification* in *2011 IEEE Nuclear Science Symposium Conference Record* (2011), 293–295.
10. Tochilin, E. Photographic detection of fast neutrons: Application to neutron radiography. *Physics in Medicine & Biology* **10,** 477 (1965).
11. Dangendorf, V., Bar, D., Bromberger, B., Feldman, G., Goldberg, M., Lauck, R., Mor, I., Tittelmeier, K., Vartsky, D. & Weierganz, M. Multi-frame energy-selective imaging system for fast-neutron radiography. *IEEE Transactions on Nuclear Science* **56,** 1135–1140 (2009).
12. Lambert, J. *Photometria sive de mensura et gradibus luminis, colorum et umbrae* (Klett, 1760).
13. Beer, A. Bestimmung der absorption des rothen lichts in farbigen flussigkeiten. *Ann. Physik* **162,** 78–88 (1852).
14. Mor, I. *Energy-resolved fast-neutron imaging via time resolved optical readout* MA thesis (2006).
15. Mor, I. *High spatial-resolution fast neutron detectors for imaging and spectrometry* PhD thesis (2017).
16. Mor, I., Dangendorf, V., Reginatto, M., Kaufmann, F., Vartsky, D., Brandis, M., Bar, D. & Goldberg, M. Reconstruction of material elemental composition using fast neutron resonance radiography. *Physics Procedia* **69,** 304–313 (2015).
17. He, L., Zhang, L., Luo, X., Fang, Y., Wei, Z., Chang, G., Yang, R., Liu, S., Su, M. & Liu, D. An optimal solvent of liquid scintillator for fast-neutron imaging applications. *Journal of Luminescence* **148,** 256–261 (2014).
18. Crystals, S.-G. Organic scintillation materials and assemblies. *Saint-Gobain Crystals, Nemours Google Scholar* (2008).
19. Crystals, S.-G. BC-400, BC-404, BC-408, BC-412, BC-416 premium plastic scintillators. *Saint-Gobain Crystals, Nemours Google Scholar* (2005).
20. Guzek, J. *Elemental radiography using fast neutron beams* PhD thesis (2012).
21. Mor, I., Vartsky, D., Bar, D., Feldman, G., Goldberg, M., Katz, D., Sayag, E., Shmueli, I., Cohen, Y. & Tal, A. High spatial resolution fast-neutron imaging detectors for pulsed fast-neutron transmission spectroscopy. *Journal of Instrumentation* **4,** P05016 (2009).
22. PISX, P. I. *1k. Roper Scientific*
23. ST-138 Controller Operation Manual.
24. Schneider, C., Rasband, W. & Eliceiri, K. NIH image to ImageJ: 25 years of image analysis. *Nature Methods* **9,** 671 (2012).

25. Dangendorf, V., Laczko, G., Reginatto, M., Vartsky, D., Goldberg, M., Mor, I., Breskin, A. & Chechik, R. Detectors for time-of-flight fast-neutron radiography 1. Neutron-counting gas detector. *Nuclear Instruments and Methods in Physics Research Section A: Accelerators, Spectrometers, Detectors and Associated Equipment* **542,** 197–205 (2005).
26. Dangendorf, V., Laczko, G., Kersten, C., Jagutzki, O. & Spillmann, U. Fast neutron resonance radiography in a pulsed neutron beam. *arXiv preprint nucl-ex/0301001* (2003).
27. Liu, Y., Sowerby, B. & Tickner, J. Comparison of neutron and high-energy X-ray dual-beam radiography for air cargo inspection. *Applied Radiation and Isotopes* **66,** 463–473 (2008).
28. Eberhardt, J., Rainey, S., Stevens, R., Sowerby, B. & Tickner, J. Fast neutron radiography scanner for the detection of contraband in air cargo containers. *Applied Radiation and Isotopes* **63,** 179–188 (2005).
29. Zboray, R., Adams, R., Cortesi, M. & Prasser, H.-M. Development of a fast neutron imaging system for investigating two-phase flows in nuclear thermal–hydraulic phenomena: A status report. *Nuclear Engineering and Design* **273,** 10–23 (2014).
30. Zboray, R., Adams, R. & Kis, Z. Fast neutron radiography and tomography at a 10 MW research reactor beamline. *Applied Radiation and Isotopes* **119,** 43–50 (2017).
31. Conte, M. & MacKay, W. *An introduction to the physics of particle accelerators* (World Scientific Publishing Company, 2008).
32. Rutherford, E. & Geiger, H. An electrical method of counting the number of α-particles from radio-active substances. *Proceedings of the Royal Society of London. Series A, Containing Papers of a Mathematical and Physical Character* **81,** 141–161 (1908).
33. Hellborg, R. *Electrostatic accelerators* (Springer, 2005).
34. Hund, F. Zur deutung der molekelspektren. III. *Zeitschrift für Physik* **43,** 805–826. ISSN: 0044-3328. https://doi.org/10.1007/BF01397249. (1927).
35. Wangsness, R. Electromagnetic fields. *Electromagnetic Fields, 2nd Edition, by Roald K. Wangsness, pp. 608. ISBN 0-471-81186-6. Wiley-VCH, July 1986.,* 608 (1986).
36. Cockcroft, J. & Walton, E. Experiments with high velocity positive ions. II. The disintegration of elements by high velocity protons. *Proc. R. Soc. Lond. A* **137,** 229–242 (1932).
37. De Graaff, R. V. A 1,500,000 volt electrostatic generator. *Phys. Rev* **38,** 1919 (1931).
38. Franklyn, C. & Daniels, G. Characterization methods for an accelerator based fast-neutron facility. *Journal of Instrumentation* **7,** C02043 (2012).
39. Franklyn, C. *Investigation of novel moderator geometries at the Necsa accelerator based neutron sources* in *Journal of Physics: Conference Series* **1021** (2018), 012076.

40. Staples, J. RFQs—An introduction. *AIP Conference Proceedings* **249,** 1483–1532. eprint: https://aip.scitation.org/doi/pdf/10.1063/1.41959. https://aip.scitation.org/doi/abs/10.1063/1.41959. (1992).

41. Lawrence, E. & Livingston, M. The production of high speed light ions without the use of high voltages. *Physical Review* **40,** 19 (1932).

42. Brede, H., Cosack, M., Dietze, G., Gumpert, H., Guldbakke, S., Jahr, R., Kutscha, M., Schlegel-Bickmann, D. & Schölermann, H. The Braunschweig accelerator facility for fast neutron research: 1: Building design and accelerators. *Nuclear Instruments and Methods* **169,** 349–358 (1980).

43. McMillan, E. The synchrotron a proposed high energy particle accelerator. *Physical Review* **68,** 143 (1945).

44. Veksler, V. A new method of acceleration of relativistic particles. *J. Phys.* **9,** 153–158 (1945).

45. Evans, R. *The Large Hadron Collider project* in *Proceedings of the Sixteenth International Cryogenic Engineering Conference/International Cryogenic Materials Conference* (1997), 45–52.

46. Collaboration, A. Observation of a new particle in the search for the standard model Higgs boson with the ATLAS detector at the LHC. *arXiv preprint arXiv:1207.7214* (2012).

47. Arai, M. & Crawford, K. *Neutron imaging and applications* (Springer, 2009).

48. Comsan, M. Spallation neutron sources for science and technology. *Proceedings of the 8th Conference on Nuclear and Particle Physics, 20-24 Nov. 2011, Hurghada, Egypt* (2011).

49. Orlov, V. Fast neutron reactors. *Atomnays Energiya* **36.** Accelerator driven systems, 341 –355 (1974).

50. Glascock, M. & Neff, H. Neutron activation analysis and provenance research in archaeology. *Measurement Science and Technology* **14,** 1516. http://stacks.iop.org/0957-0233/14/i=9/a=304. (2003).

51. Reijonen, J. *Compact neutron generators for medical, home land security, and planetary exploration* in *Proceedings of the 2005 Particle Accelerator Conference* (2005), 49–53.

52. Lang, R., Pienaar, J., Hogenbirk, E., Masson, D., Nolte, R., Zimbal, A., Röttger, S., Benabderrahmane, M. & Bruno, G. Characterization of a deuterium–deuterium plasma fusion neutron generator. *Nuclear Instruments and Methods in Physics Research Section A: Accelerators, Spectrometers, Detectors and Associated Equipment* **879,** 31 –38. ISSN: 0168-9002. http://www.sciencedirect.com/science/article/pii/S0168900217310380. (2018).

53. Martone, M., Angelone, M. & Pillon, M. The 14 MeV Frascati neutron generator. *Journal of Nuclear Materials* **212-215.** Fusion Reactor Materials, 1661 –1664. ISSN: 0022-3115. http://www.sciencedirect.com/science/article/pii/0022311594911096. (1994).

54. Adams, R., Bort, L., Zboray, R. & Prasser, H.-M. Development and characterization of a D–D fast neutron generator for imaging applications. *Applied Radiation and Isotopes* **96,** 114 –121. ISSN: 0969-8043. http://www.sciencedirect.com/science/article/pii/S0969804314004084. (2015).

55. Bauer, G. Physics and technology of spallation neutron sources. *Nuclear Instruments and Methods in Physics Research Section A: Accelerators, Spectrometers, Detectors and Associated Equipment* **463.** Accelerator driven systems, 505 –543. ISSN: 0168-9002. http://www.sciencedirect.com/science/article/pii/S016890020100167X. (2001).

56. Mason, T. *et al.* The Spallation Neutron Source in Oak Ridge: A powerful tool for materials research. *Physica B: Condensed Matter* **385-386,** 955 –960. ISSN: 0921-4526. http://www.sciencedirect.com/science/article/pii/S092145260601177X (2006).

57. Arai, M. & Maekawa, F. Japan Spallation Neutron Source (JSNS) of J-PARC. *Nuclear Physics News* **19,** 34–39. eprint: https://doi.org/10.1080/10506890903405316. https://doi.org/10.1080/10506890903405316 (2009).

58. Jie, W., Shi-Nian, F., Jing-Yu, T., Ju-Zhou, T., Ding-Sheng, W., Fang-Wei, W. & Sheng, W. China Spallation Neutron Source - an overview of application prospects. *Chinese Physics C* **33,** 1033–1042. https://doi.org/10.1088%2F1674-1137%2F33%2F11%2F021 (2009).

59. Garoby, R., Vergara, A, Danared, H, Alonso, I, Bargallo, E, Cheymol, B, Darve, C, Eshraqi, M, Hassanzadegan, H, Jansson, A, *et al.* The european spallation source design. *Physica Scripta* **93,** 014001 (2017).

60. Kononov, V., Bokhovko, M., Kononov, O., Soloviev, N., Chu, W. & Nigg, D. Accelerator-based fast neutron sources for neutron therapy. *Nuclear Instruments and Methods in Physics Research Section A: Accelerators, Spectrometers, Detectors and Associated Equipment* **564,** 525 –531. ISSN: 0168-9002. http://www.sciencedirect.com/science/article/pii/S0168900206005705. (2006).

61. Wei, Z., Yan, Y., Yao, Z., Lan, C. & Wang, J. Evaluation of the neutron energy spectrum, angular distribution, and yield of the ^{9}Be(d,n) reaction with a thick beryllium target. *Phys. Rev. C* **87,** 054605. https://link.aps.org/doi/10.1103/PhysRevC.87.054605. (5 2013).

62. Kar, S., Green, A., Ahmed, H., Alejo, A., Robinson, A., Cerchez, M., Clarke, R., Doria, D., Dorkings, S. & Fernandez, J. Beamed neutron emission driven by laser accelerated light ions. *New Journal of Physics* **18,** 053002 (2016).

63. Oláh, L., El-Megrab, A., Fenyvesi, A., Majdeddin, A., Dóczi, R., Semkova, V., Qaim, S. & Csikai, J. Investigations on neutron fields produced in 2H(d, n)3He and 9Be(d, n)10B reactions. *Nuclear Instruments and Methods in Physics Research Section A: Accelerators, Spectrometers, Detectors and Associated Equipment* **404,** 373 – 380. ISSN: 0168-9002. http://www.sciencedirect.com/science/article/pii/S0168900297011509. (1998).

64. Capoulat, M., Herrera, M., Minsky, D., González, S. & Kreiner, A. 9Be(d,n)10B-based neutron sources for BNCT. *Applied Radiation and Isotopes* **88.** *15th International Congress on Neutron Capture Therapy Impact of a New Radiotherapy against Cancer*, 190 –194. ISSN: 0969-8043. http://www.sciencedirect.com/science/article/pii/S0969804313004831. (2014).

65. Matysiak, W., Prestwich, W. & Byun, S. Precise measurements of the thick target neutron yields of the 7Li(p,n) reaction. *Nuclear Instruments and Methods in Physics Research Section A: Accelerators, Spectrometers, Detectors and Associated Equipment* **643,** 47 –52. ISSN: 0168-9002. http://www.sciencedirect.com/science/article/pii/S0168900211007728. (2011).

66. Guerrero, C., Tsinganis, A., Berthoumieux, E., Barbagallo, M., Belloni, F., Gunsing, F., Weiß, C., Chiaveri, E., Calviani, M. & Vlachoudis, V. Performance of the neutron time-of-flight facility n_TOF at CERN. *The European Physical Journal A* **49,** 27 (2013).

67. Crandall, K. & Rusthoi, D. TRACE-3D. *Los Alamos* (1997).

68. Bashter, I. Calculation of radiation attenuation coefficients for shielding concretes. *Annals of Nuclear Energy* **24,** 1389–1401 (1997).

69. Chen, G. & Lanza, R. Fast neutron resonance radiography for elemental imaging: Theory and applications. *IEEE Transactions on Nuclear Science* **49,** 1919–1924 (2002).

70. Gardner, W. & Calissendorff, C. Gamma-ray and neutron attenuation in measurement of soil bulk density and water content. *In-Isotope and Radiation Techniques in Soil Physics and Irrigation Studies. Vienna, IAEA,* 101–113 (1967).

71. Ackermann, M., Zimmer, P., McGraw, J. & Kopit, E. *COTS Options for Low-Cost SSA*. tech. rep. (Sandia National Lab.(SNL-NM), Albuquerque, NM (United States), 2015).

72. Govender, I., Richter, M., Mainza, A. & Klerk, D. D. A positron emission particle tracking investigation of the scaling law governing free surface flows in tumbling mills. *AIChE Journal* **63,** 903–913 (2017).

73. Morrison, A., Govender, I., Mainza, A. & Parker, D. The shape and behaviour of a granular bed in a rotating drum using Eulerian flow fields obtained from PEPT. *Chemical Engineering Science* (2016).

74. De Haas, B., Bosch, A. & Kottgen, A. *Effect of Slurry Density on Load Dynamic and Milling Performances in an Iron Ore Ball Mill -On-line Estimation of In-mill Slurry Density* in (Apr. 2012).

75. McLane, V. *Neutron cross sections* (London: Academic Press, 2012).

76. De Beer, F., Strydom, W. & Griesel, E. The drying process of concrete: A neutron radiography study. *Applied Radiation and Isotopes* (2004).

77. Brede, H., Dietze, G., Kudo, K., Schrewe, U., Tancu, F. & Wen, C. Neutron yields from thick Be targets bombarded with deuterons and protons. *NIM* (1989).

78. Dangendorf, V. Multi-frame energy-selective imaging system for fast-neutron radiography. *IEEE Transactions on Nuclear Science* (2008).

79. Mellmann, J. The transverse motion of solids in rotating cylinders—forms of motion and transition behavior. *Powder Technology* **118,** 251 –270. ISSN: 0032-5910. http://www.sciencedirect.com/science/article/pii/S0032591000004022 (2001).

80. *www.crytur.com*

81. Clermont, B. & de Haas, B. Optimization of mill performance by using online ball and pulp measurements. *The Journal of the Southern African Institute of Mining and Metallurgy* (2010).

82. Harms, A. & Wyman, D. *Mathematics and physics of neutron radiography* (Dordrecht: D.Reidel Publishing Company, 1986).

83. Parker, D., Broadbent, C., Fowles, P., Hawkesworth, M. & McNeil, P. Positron emission particle tracking: A technique for studying flow within engineering equipment. *Nuclear Instruments and Methods in Physics Research Section A: Accelerators, Spectrometers, Detectors and Associated Equipment* **326,** 592–607 (1993).

84. Parker, D., Forster, R., Fowles, P. & Takhar, P. Positron emission particle tracking using the new Birmingham positron camera. *Nuclear Instruments and Methods in Physics Research Section A: Accelerators, Spectrometers, Detectors and Associated Equipment* **477,** 540–545 (2002).

85. Seville, J., Ingram, A. & Parker, D. Probing processes using positrons. *Chemical Engineering Research and Design* **83,** 788–793 (2005).

86. Bakalis, S., Cox, P., Russell, A., D, J. P. & Fryer, P. Development and use of positron emitting particle tracking (PEPT) for velocity measurements in viscous fluids in pilot scale equipment. *Chemical Engineering Science* **61,** 1864–1877 (2006).

87. Parker, D., Leadbeater, T., Fan, X., Hausard, M., Ingram, A. & Yang, Z. Positron imaging techniques for process engineering: Recent developments at Birmingham. *Measurement Science and Technology* **19,** 094004 (2008).

88. Leadbeater, T., Parker, D. & Gargiuli, J. Positron imaging systems for studying particulate, granular and multiphase flows. *Particuology* **10,** 146–153 (2012).

89. Boucher, D., Deng, Z., Leadbeater, T., Langlois, R., Renaud, M. & Waters, K. PEPT studies of heavy particle flow within a spiral concentrator. *Minerals Engineering* **62,** 120–128 (2014).

90. Guida, A., Nienow, A. & Barigou, M. Lagrangian tools for the analysis of mixing in single-phase and multiphase flow systems. *AIChE Journal* **58,** 31–45 (2012).

91. Buffler, A., Govender, I., Cilliers, J., Parker, D., Franzidis, J., Mainza, A., Newman, R., Powell, M. & der Westhuizen, A. V. *PEPT Cape Town: a new positron emission particle tracking facility at iThemba LABS* in *Proceedings of International Topical Meeting on Nuclear Research Applications and Utilization of Accelerators* **173** (2010).

92. Buffler, A., Cole, K., Leadbeater, T. & van Heerden, M. *Positron emission particle tracking: A powerful technique for flow studies* in *International Journal of Modern Physics: Conference Series* **48** (2018), 1860113.

93. Bickell, M., Buffler, A., Govender, I. & Parker, D. A new line density tracking algorithm for PEPT and its application to multiple tracers. *Nuclear Instruments and Methods in Physics Research Section A: Accelerators, Spectrometers, Detectors and Associated Equipment* **682,** 36–41 (2012).

94. Martin, T., Seville, J. & Parker, D. A general method for quantifying dispersion in multiscale systems using trajectory analysis. *Chemical Engineering Science* **62,** 3419–3428 (2007).

95. Wildman, R., Hrenya, C., Huntley, J., Leadbeater, T. & Parker, D. Experimental determination of temperature profiles in a sheared granular bed containing two and three sizes of particles. *Granular Matter* **14,** 215–220 (2012).

96. Windows-Yule, C., Rivas, N. & Parker, D. Thermal convection and temperature inhomogeneity in a vibrofluidized granular bed: The influence of sidewall dissipation. *Physical Review Letters* **111,** 038001 (2013).

97. Buijtenen, M. V., Dijk, W.-J. V., Deen, N., Kuipers, J., Leadbeater, T. & Parker, D. Numerical and experimental study on multiple-spout fluidized beds. *Chemical Engineering Science* **66,** 2368–2376 (2011).

98. García-Triñanes, P., Seville, J., Boissière, B., Ansart, R., Leadbeater, T. & Parker, D. Hydrodynamics and particle motion in upward flowing dense particle suspensions: Application in solar receivers. *Chemical Engineering Science* **146,** 346–356 (2016).

99. Parker, D., Dijkstra, A., Martin, T. & Seville, J. Positron emission particle tracking studies of spherical particle motion in rotating drums. *Chem. Eng. Sci.* **52,** 2011 (1997).

100. Morrison, A., Govender, I., Mainza, A. & Parker, D. The shape and behaviour of a granular bed in a rotating drum using Eulerian flow fields obtained from PEPT. *Chemical Engineering Science* **152,** 186–198 (2016).

101. Cole, K., Waters, K., Parker, D., Neethling, S. & Cilliers, J. PEPT combined with high speed digital imaging for particle tracking in dynamic foams. *Chemical Engineering Science* **65,** 1887–1890 (2010).

102. Chaouki, J., Larachi, F. & Duduković, M. Noninvasive tomographic and velocimetric monitoring of multiphase flows. *Industrial & Engineering Chemistry Research* **36,** 4476–4503 (1997).

103. Boucher, D., Jordens, A., Sovechles, J., Langlois, R., Leadbeater, T., Rowson, N., Cilliers, J. & Waters, K. Direct mineral tracer activation in positron emission particle tracking of a flotation cell. *Minerals Engineering* **100,** 155–165 (2017).

104. Zhutovsky, S., Kovler, K. & Bentur, A. Efficiency of lightweight aggregates for internal curing of high strength concrete to eliminate autogenous shrinking. *Materials and Structures* (2002).

105. Korshunov, D. & Sidorenko, M. Methods for determining the strength of concrete. *Materials and Structures* (1992).

106. Salim, R. *Extent of capillary rise in sands and silts* MA thesis (Western Michigan University, 2016).

107. Tyree, M. Matric potential. *Encyclopedia of Water Science* (2003).

108. Lu, N. & Likos, W. Rate of Capillary Rise in Soil. *Journal of Geotechnical and Geoenvironmental Engineering* (2004).

109. Andersson, P., Sunden, E. A., Svard, S. J. & Sjostrand, H. Correction for dynamic bias error in transmission measurements of void fraction. *Review of Scientific Instruments* (2012).

110. Eggleston, J. & Rojstaczer, S. The value of grain-size hydraulic conductivity estimates: Comparison with high resolution in-situ field hydraulic conductivity. *Geophysical Research Letters* (2001).

111. Hwang, H.-T., Jeen, S.-W., Suleiman, A. & Lee, K.-K. Comparison of Saturated Hydraulic Conductivity Estimated by Three Different Methods. *Water* **9,** 942 (Dec. 2017).

112. Kaestner, A., Lehmann, E. & Stampanoni, M. Imaging and image processing in porous media research and Advances in Water Resources. *NIM* (2008).